# POLITECNICO DI MILANO

Facoltà di Ingegneria Industriale

Corso di Laurea Magistrale in Ingegneria Aeronautica



# Unsteady aerodynamic optimization of a morphing airfoil


Relatore: Prof. Giuseppe QUARANTA

Tesi di laurea di:
Andrea Francesco CORTESI
Matr. 782785



Anno Accademico 2012 - 2013

La meta è questa: mettermi sempre là dove io possa servir meglio, dove la mia indole, le mie doti e le mie qualità trovino il terreno migliore, il più largo campo d'azione.

H. Hesse
*Narciso e Boccadoro*

Grazie

# CONTENTS

**List of Figures** **xi**

**List of Tables** **xv**

**Introduction** **1**

**1 Aerodynamic model** **7**
1.1 General Küssner and Schwarz theory . . . . . 7
1.1.1 Computation of forces . . . . . 9
1.1.2 Computation of power . . . . . 10
1.2 Moving airfoil . . . . . 11
1.2.1 Rigidly moving airfoil . . . . . 11
1.2.2 Flap rotation . . . . . 13
1.2.3 Flap and trim tab rotation . . . . . 15
1.2.4 Deforming airfoil . . . . . 15
1.2.5 Computation of power . . . . . 16
1.2.6 Comparison with Glauert theory . . . . . 17
1.2.7 Comparison with Theodorsen theory . . . . . 18
1.3 Piecewise cubic mean-line . . . . . 21
1.3.1 Cubic mean-line . . . . . 23
1.3.2 Cubic Flap . . . . . 26
1.3.3 Comparison with flapped airfoil . . . . . 30
1.3.4 Convergence . . . . . 32

**2 Inertial and elastic models** **35**
2.1 Equation of motion . . . . . 35
2.1.1 Ritz-Galerkin method . . . . . 36

2.2 Hermitian finite elements . . . . . 37
2.3 Mass and stiffness matrices computation . . . . . 38
2.3.1 Mass and bending stiffness distributions . . . . . 38
2.3.2 Thickness . . . . . 41
2.3.3 Integration . . . . . 42
2.3.4 Change of variables . . . . . 43
2.4 Power computation . . . . . 44

**3 Optimization** **47**
3.1 What to Optimize . . . . . 47
3.2 Optimization Algorithms . . . . . 49
3.2.1 Sequential Quadratic Programming . . . . . 50
3.2.2 Genetic Algorithms . . . . . 51
3.3 Multi-Objective Optimization . . . . . 52
3.3.1 NSGA-II algorithm . . . . . 54
3.4 Analytical Optimization Example . . . . . 55
3.5 Quarter-chord moment numerical optimization . . . . . 60
3.6 Aerodynamic work numerical optimization . . . . . 61
3.7 Aerodynamic moment and power numerical optimization . . . 61
3.8 Aerodynamic moment and actuation power numerical optimization . . . . . 63

**4 Results** **65**
4.1 Aerodynamic Moment Optimization . . . . . 65
4.1.1 Airfoil with a single flap . . . . . 65
4.1.2 Airfoil with two flaps . . . . . 71
4.1.3 Cubic mean-line . . . . . 74
4.1.4 Piecewise Cubic, two pieces . . . . . 75
4.2 Aerodynamic Moment and Power Optimization . . . . . 75
4.2.1 Airfoil with two flaps . . . . . 76
4.2.2 Piecewise cubic mean-line . . . . . 78
4.3 Aerodynamic Moment and total Power Optimization . . . . . 86

**5 Conclusions** **97**
5.1 Future developments . . . . . 98

**A Küssner and Schwarz integrals computation** **101**
A.1 Integrals on the whole airfoil . . . . . 101
A.2 Integrals on a portion of airfoil . . . . . 104

**B Theodorsen coefficients** **109**

**C Estratto in lingua italiana** **115**

**Bibliography** **121**

# LIST OF FIGURES


1.1 Pressure difference distribution, steady case, $N_P = 1000$ with both flaps deflected . . . . . 18
1.2 Example of Küssner and Schwarz pressure difference distribution, $N_P = 100$ . . . . . 21
1.3 Example of cubic polynomial deformation of the airfoil mean-line and superposition of a cubic flap . . . . . 27
1.4 Least squares fitting between flapped airfoil and two pieces cubic spline camberline regular up to the first derivative . . . 33
1.5 Least squares fitting between flapped airfoil and two pieces cubic spline camberline up to the first derivative, pressure difference, $N_P = 1000$ . . . . . 34

2.1 Reference mono-dimensional hermitian finite element . . . . . 38
2.2 Example of helicopteristic NACA0012 airfoil . . . . . 39
2.3 Airfoil simplified cross section . . . . . 40

3.1 Contour plot of the object function, with a representation of the constraint and the optimal solution, for $\bar{C}_L = 1$, $k = 0.5$ . 59
3.2 Aerodynamic work optimization with a fixed incidence . . . . 62

4.1 Comparison between analytical and SQP solutions for a single-flapped airfoil moment optimization, $k = 0.5$ . . . . . 66
4.2 Comparison between analytical and GA solutions for a single-flapped airfoil moment optimization, $k = 0.5$ . . . . . 67
4.3 Variation of the optimal solution with respect to the reduced frequency for a single-flapped airfoil, minimizing the aerodynamic moment, $\tilde{x}_F = 0.5$ . . . . . 68

4.4 Variation of the optimal moment with respect to the reduced frequency for a single-flapped airfoil, $\tilde{x}_F = 0.5$ . . . . . 69
4.5 Variation of the optimal solution with respect to the reduced frequency for a single-flapped airfoil, minimizing the aerodynamic moment at different hinge positions, $\bar{C}_L = 0.05$ . . . . . 70
4.6 Variation of the optimum moment with respect to the reduced frequency for a single-flapped airfoil, minimizing the aerodynamic moment at different hinge positions, $\bar{C}_L = 0.05$ . 71
4.7 Variation of the optimal solution with respect to the reduced frequency for a double-flapped airfoil, minimizing the aerodynamic moment, $\tilde{x}_F = 0.4$, $\tilde{x}_{F_1} = 0.6$ . . . . . 73
4.8 Optimal solution for the moment optimization, cubic mean-line, $\bar{C}_L = 0.05$ . . . . . 74
4.9 Example of optimal shape for the moment optimization, cubic mean-line, $k = 0.5$, $\bar{C}_L = 0.05$ . . . . . 75
4.10 Pareto front, two flaps model, $k = 0.3$, $\tilde{x}_F = 0.4$, $\tilde{x}_{F_1} = 0.6$ $\bar{C}_L = 0.05$ . . . . . 76
4.11 Optimal solution with respect to the weight $A$ defined in eq. 3.34, two flaps model, $k = 0.3$ . . . . . 77
4.12 Optimal solution with respect to the scalarization weight $A$, two flaps model, $\bar{C}_L = 0.05$ . . . . . 77
4.13 Pareto front, two-pieces cubic spline model, $k = 0.4$, $\tilde{x}_F = 0.5$, $\bar{C}_L = 0.05$ . . . . . 78
4.14 Optimal shapes at different parts of the Pareto front, $k = 0.4$, $\bar{C}_L = 0.05$ . . . . . 79
4.15 Optimal solutions comparison at different $N_t$ . . . . . 81
4.16 Pareto fronts with different $N_t$ comparison at different $k$ . . . 82
4.17 Optimal solutions comparison at different $k$, $N_t = 4$ . . . . . 83
4.18 Optimal pressure difference comparison at different $k$, $N_t = 4$, real part . . . . . 84
4.19 Optimal pressure difference comparison at different $k$, $N_t = 4$, imaginary part . . . . . 85
4.20 Optimal solutions comparison at different $k$, $N_t = 4$, $\rho_s = 300\,kg/m^3$ and $E_s = 0.4\,GPa$ . . . . . 88
4.21 Optimal pressure difference comparison at different $k$, $N_t = 4$, $\rho_s = 300\,kg/m^3$ and $E_s = 0.4\,GPa$, real part . . . . . 89
4.22 Optimal pressure difference comparison at different $k$, $N_t = 4$, $\rho_s = 300\,kg/m^3$ and $E_s = 0.4\,GPa$, imaginary part . . . . . 90
4.23 Pareto fronts comparison at different $k$, $N_t = 4$, $\rho_s = 300\,kg/m^3$ and $E_s = 0.4\,GPa$ . . . . . 91

4.24 Pareto fronts comparison at different $k$, $N_t = 4$, $\rho_s = 300\,kg/m^3$ and $E_s = 0.1\,GPa$ . . . . . 91
4.25 Pareto fronts comparison at different $k$, $N_t = 4$, $\rho_s = 75\,kg/m^3$ and $E_s = 0.4\,GPa$ . . . . . 91
4.26 Pareto fronts comparison at different $k$, $N_t = 4$ . . . . . 92
4.27 Comparison between the aerodynamic power optimization solutions and the actuation power optimization solutions . . . . 92
4.28 Optimal solutions comparison at different $k$, $N_t = 4$, $\rho_s = 300\,kg/m^3$ and $E_s = 0.1\,GPa$ . . . . . 93
4.29 Optimal solutions comparison at different $k$, $N_t = 4$, $\rho_s = 75\,kg/m^3$ and $E_s = 0.4\,GPa$ . . . . . 94
4.30 Optimal solutions comparison at different $k$, $N_t = 4$, $\rho_s = 75\,kg/m^3$ and $E_s = 0.1\,GPa$ . . . . . 95
4.31 Optimal solutions comparison at different $k$, $N_t = 4$, $\rho_s = 600\,kg/m^3$ and $E_s = 0.8\,GPa$ . . . . . 96

C.1 Esempio di deformazione polinomiale cubica della linea media e sovrapposizione di un flap cubico . . . . . 117

# LIST OF TABLES


1.1 Percentage differences between Theodorsen and Küssner and Schwarz theories, $N_P = 100$, at different configurations $[\alpha, \beta, \beta_1]$, with $k = 0.1$ . . . . . 21
1.2 Percentage differences between flapped and spline representations of the chord, $N_P = 1000$, spline regular up to the second derivative, two-segment spline, $k = 0.5$ . . . . . 32
1.3 Percentage differences between flapped and spline representations of the chord, $N_P = 1000$, spline regular up to the first derivative, two-segment spline, $k = 0.5$ . . . . . 32
1.4 Residuals between aerodynamic power truncated at a different number of upwash coefficients. The spline is a least squares fitting of a flapped airfoil with the indicated angle amplitudes 33

2.1 Material properties of helicopter blade . . . . . 39
2.2 NACA four digits airfoil thickness coefficients . . . . . 41
2.3 Nodes and weights for Gauss-Legendre integration method . . 43

3.1 Analytical optimal solutions for $\tilde{x}_p = -0.5$, $\tilde{x}_f = 0.5$, $k = 0.5$ . 59

4.1 Analytical optimal solutions for $\tilde{x}_p = -0.5$, $\tilde{x}_F = 0.4$, $\tilde{x}_{F_1} = 0.6$, $k = 0.5$ . . . . . 72

**Abstract**

This thesis work presents an approach to aerodynamic optimization of harmonically deforming morphing thin-airfoils. The frequency domain Küssner and Schwarz unsteady aerodynamic theory is extended to compute aerodynamic forces and power using a piecewise cubic representation of the camberline displacements, since this general formulation is able to model a wide range of shapes.

To compute the inertial and elastic contributions to the actuation power, the airfoil is treated as an Euler-Bernoulli beam, and mass and stiffness matrices are computed with a Ritz-Galerkin approach, using hermitian finite elements as shape functions.

Optimizations are performed with both genetic algorithms and sequential quadratic programming methods. Single-objective optimizations are performed on the aerodynamic moment. Multi-objective optimization are carried out to minimize the aerodynamic moment and the power (aerodynamic power or actuation power). Every optimization takes into account a lift constraint. Results are computed at different reduced frequencies.

**Key words:** optimization, morphing airfoils, unsteady aerodynamics

**Sommario**

In questa tesi è presentato un approccio per l'ottimizzazione aerodinamica di un profilo sottile *morphing* in grado di deformarsi armonicamente. Il modello di aerodinamica instazionaria nel dominio della frequenza di Küssner e Schwarz viene esteso per calcolare la potenza e le azioni aerodinamiche nel caso di una rappresentazione per mezzo di una spline cubica degli spostamenti della linea media, poiché questa formulazione è in grado di modellizzare un' ampia gamma di forme.

Per calcolare i contributi inerziale ed elastico alla potenza di attuazione totale, il profilo viene trattato come una trave di Eulero-Bernoulli e le matrici di massa e rigidezza sono calcolate utilizzando un approccio alla Ritz-Galerkin, scegliendo come funzioni di forma gli elementi finiti hermitiani.

Le ottimizzazioni sono svolte sia con un algoritmo genetico, sia con l'approccio *sequential quadratic programming*. Si eseguono ottimizzazioni mono-obiettivo sul momento aerodinamico, mentre le ottimizzazioni multi-obiettivo sono effettuate usando come obiettivi il momento aerodinamico e la potenza (aerodinamica o totale di attuazione). Ogni ottimizzazione prende in considerazione un vincolo sulla portanza. I risultati vengono calcolati a diverse frequenze ridotte.

**Parole Chiave:** ottimizzazione, aerodinamica instazionaria, profili morphing

# INTRODUCTION AND STATE OF THE ART

The introduction of new material technologies in structural application, such as adaptive materials, opens the door to the possibility of changing the shape of an aerodynamic surface in a smooth fashion by means of the application of distributed actuation forces. These *morphing* capabilities can be exploited to achieve multiple functions in both fixed wing and rotary wing aircrafts. Morphing wings or blades may lead to improvements in performances, maneuverability, aerodynamic and aeroelastic features, hence the research in this field is currently being conducted extensively.

The helicopter main rotor performance enhancement is object of several researches, because of its strong influence on the overall rotorcraft performance in hover, forward flight, vibrations and noise emission and so on. One difficult aspect in the design of rotor blades is that they are subject to a wide range of different aerodynamic conditions depending on their azimuthal position and the flight speed, hence it may be hard to choose project specifications that are an effective compromise between all the different requirements. The main rotor blades reconfiguration during the flight can be used in this sense to adapt to various conditions, in order to increase the payload, fuel efficiency, range, maximum speed and altitude, and also reduce the vibrations and noise more efficiently when compared to rotor blades with a fixed geometry.

One of the key aspects faced by modern helicopter design is vibration reduction. Helicopters are susceptible to extensive vibration because of various reasons: the unsteady aerodynamics acting on the rotor disk, nonlinear inertial couplings of rotating blades, complex rotor-fuselage interaction effects, and so on. This high level of vibration limits the helicopter performance, re-

duces structural life and increases maintenance costs. Furthermore it lowers the flight quality of passengers and crew. Therefore the need for vibration reduction is crucial. Morphing blades, constructed with adaptive materials, could be exploited to actively reduce the level of vibrations at a wide range of flying conditions, in order to improve all the aforementioned performances.

As said before, the main rotor dynamic behaviour plays a major role in the overall helicopter flight dynamics and maneuverability. Morphing technologies could support or replace traditional helicopter control systems in order to improve the main rotor dynamics, saving flight control energy, expanding the operating envelope and also to being used to trim the rotorcraft.

Active control systems could employ morphing actuators to implement gust alleviation system, useful to improve aeroelastic blade response and the overall flight quality.

In forward flight adaptive blades could also be used to move the dynamic stall effects to higher flight speed, enhancing the helicopter maximum cruise speed.

Last but not least morphing technologies could be able to reduce the required flight power by optimizing the blades shape not only in a single project condition, but adapting to a wider range of flight conditions, leading to a energy save. For this purpose the actuation system is essential not being too energy consuming in order to have a positive net earning.

The aim of this work is on finding a simple harmonic aerodynamic model for deforming airfoils suitable for a preliminary optimization of the deformation of a morphing airfoil, in order to enhance some useful performance, such as the the reduction of the oscillatory load, while maintaining a reasonable level of required actuation power. Another goal is to investigate the aforementioned optimization problem to provide the basis for further works, which may focus on more accurate, complete and extended morphing blade design and optimization. Since this work is not intended to produce a design tool for morphing airfoils, simplicity will often be preferred to accuracy.

Some results are also obtained with a flapped airfoil, which represents a more classical, albeit non widely used in rotorcraft applications, way of changing the mean-line camber of an airfoil.

# Aerodynamics

In order to enforce the optimization problem nimbly a simple model is to be chosen to describe the oscillating airfoil aerodynamics. The assumption of a thin airfoil harmonically oscillating and deforming with small constant amplitudes in a potential flow allows the adoption of a linearized two-dimensional

framework, where the airfoil can be seen as an aerodynamically equivalent mean line.

Non stationary linearized aerodynamic forces were firstly computed by Theodorsen in [22] and [23] and by Küssner and Schwarz in [15], and followed by several studies. Hence, there are different theories that could be used to develop a proper aerodynamic model of a flexible airfoil.

Classical unsteady aerodynamic studies usually deal with the problem of an airfoil subject to pitch, plunge and flaps movements, while a morphing airfoil is capable of a continuous regular deformation. Recent works, like the one from Johnston *et al.* [13], extend the unsteady thin airfoil theory to analyze the aerodynamic characteristics of a deforming airfoil, which is defined in that case by two quadratic curves with arbitrary coefficients.

The choice in this work is to adopt Küssner and Schwarz original model [15], where an integral representation in complex form is employed for computing the pressure distribution on the airfoil. The theory will be extended in order to take into account also the morphing movement of the mean line, represented with a piecewise cubic polynomial.

## Aeroelasticity

The concept of morphing structures must be dealt with very carefully. If the structure is stiff, it will require a large amount of energy to be deformed. Therefore a more flexible construction, allowing deformations at reasonable power costs, is desirable. However, this increased flexibility may cause the deterioration of the aeroelastic behaviour, leading morphing structures to be more sensitive to instability problems resulting from the interaction with the fluid flow over the structure.

The literature has extensively covered the subject of the aeroelasticity of elastically supported rigid airfoils and classical aeroelastic problems (*e.g.* [1], [9]), while only a few more recent studies have been done on flexible airfoils and their implication in flutter. Currently, problems of elastic airfoils aeroelasticity are often related to the realization of lightweight wing structures made of advanced composite materials in order to improve their aerodynamic and aeroelastic performances, since they are highly flexible.

For instance Murua, Palacios and Peirò in [16] analyzed the aeroelasticity of a compliant airfoil using an oscillating potential aerodynamic model and considering the airfoil as a flexible beam, providing a simple way to predict "camber flutter" and helping identifying its dominant physical mechanisms.

Drazumeric *et al.* in [8] studied the aeroelastic stability of a rigid airfoil-shaped leading edge, and a flexible thin laminated composite plate confor-

mally attached to its trailing edge.

Although in this work the aeroelastic problem is not discussed, it is important to remember the essential role that it plays in the overall blade behaviour, therefore it must be taken into account as soon as possible in the design of a morphing blade, possibly including it in the optimization process.

## Aerodynamic Optimization

A lot of work has been performed in the past years in the field of aerodynamic optimization. Several studies tried to optimize the shape of various aerodynamic surfaces, not only in the aeronautical field, in order to improve certain performance. These have been carried out with the employment of different aerodynamic models, from simple potential based models to RANS simulations. Some of those studies have been applied also on adaptive aerodynamic surfaces, using steady aerodynamics (for example [20], [21], [17], [10] to cite some).

Although steady aerodynamics can be a good model for some aeronautical applications, it is not certainly a suitable model for rotorcrafts blades, whose aerodynamic environment is highly unsteady. Furthermore, unsteadiness, if taken into account, can be exploited during the optimization process in order to obtain better solutions with respect to the one obtained with a steady model applied to an unsteady case. Non-stationary aerodynamic shape optimization are more difficult to find in literature, although in the recent years some studies have been done in this field (*e.g.* [25]).

In this framework this thesis wants to introduce a simple way to perform unsteady aerodynamic optimizations, developed in the frequency domain, that can be a starting step for further more accurate works.

## Structure of this work

This work is divided in five chapters, each one being about a specific topic.

- In chapter 1 a suitable aerodynamic model is discussed, starting from Küssner and Schwarz unsteady thin-airfoils theory firstly appeared in [15]. An approach to compute the pressure distribution, lift, aerodynamic moment and power is described in detail. Both flapped airfoil and a morphing airfoil are taken into account. Tests and comparisons are made to verify the goodness and the convergence of the method.

- In order to compute the global actuation power for a morphing airfoil, also elastic and inertial contribution must be considered. Chapter 2

is about this subject. The goal is to find a simple way to compute the blade structural properties and use them to obtain the actuation power.

- Chapter 3 gives some general descriptions of the optimization problem and of the algorithm used to solve it. Then each specific optimization performed is justified and illustrated. Also some simple analytical optimal results are computed.
- In chapter 4 are displayed and described all the major results of the different optimizations performed.
- Chapter 5 takes stock of the accomplishments and proposes some further developments.

# CHAPTER 1

# AERODYNAMIC MODEL

The problem of the aerodynamics of a section of a morphing blade can be modeled as a thin airfoil oscillating and deforming in a two-dimensional incompressible flow. A simple and fast model to obtain the unsteady aerodynamic loads, suitable for such a problem, is the Küssner and Schwarz general theory ([15]). This is an alternative approach to the Theodorsen theory for oscillating thin airfoils described in [22] and extended in [23].

As the thin airfoil theory is a linearized theory, solutions can be superposed to obtain another solution. So the motion of the airfoil can be divided into a mean motion and a perturbation. The mean motion is a rectilinear uniform translation of speed $U$ with respect to the fluid at rest at infinity. Then, a simple-harmonic oscillation of small (infinitesimal) amplitude is superposed. Therefore the thickness, the mean camber and the mean angle of attack are then neglected,as their effect can be added later superposing their steady-state solutions.

## 1.1 General Küssner and Schwarz theory

Within the framework described above the airfoil can be represented as a straight line aligned with the $x$ axis of the reference frame. The origin is placed at the mid-chord point, and the $z$ axis is perpendicular to the chord and directed toward the upper side of the airfoil. So the chord goes from $[-b, b]$ and the asymptotic air velocity $U$ is aligned with the $x$ axis and has the same direction.

It is possible to represent the perturbation velocity of a periodic move-

ment of the airfoil, with frequency $\omega$, as

$$v(x,t) = f(x)e^{j(\omega t+\varphi(x))} \tag{1.1}$$

where $f(x)$ is the amplitude and $\varphi(x)$ the phase of the perturbation, both depending on the position. It is useful to perform the change of variables $x = b\cos\theta$, so that $\theta = \pi$ at the leading edge and $\theta = 0$ at the trailing edge, so

$$v(\theta,t) = f(\theta)e^{j(\omega t+\varphi(\theta))} \tag{1.2}$$

Now the function $v(\theta,t)$ can be expressed as a Fourier series with respect to the spatial variable

$$v(\theta,t) = -Ue^{j\omega t}\left(P_0 + 2\sum_{n=1}^{\infty} P_n \cos n\theta\right) \tag{1.3}$$

where the series coefficients $P_n \in \mathbb{C}$, called *upwash coefficient*, are

$$P_n = -\frac{1}{\pi U e^{j\omega t}}\int_0^{\pi} v(\theta,t)\cos n\theta\, d\theta = -\frac{1}{\pi U}\int_0^{\pi} f(\theta)e^{j\varphi(\theta)}\cos n\theta\, d\theta \tag{1.4}$$

Following the method provided in [9, Chapter13], it is possible to compute the difference of pressure coefficient between the lower and the upper sides of a thin airfoil. Küssner and Schwarz proved that it can be expressed as a Fourier series

$$\Delta C_p(\theta,t) = C_{p_{\text{lower}}} - C_{p_{\text{upper}}} = e^{j\omega t}\left(4a_0\tan\frac{\theta}{2} + 8\sum_{n=1}^{\infty} a_n \sin n\theta\right) \tag{1.5}$$

with the $a_n$ coefficient that can be expressed as function of the upwash coefficients

$$a_0 = C(k)(P_0 + P_1) - P_1 \tag{1.6}$$

$$a_n = P_n + \frac{jk}{2}(P_{n-1} - P_{n+1}) \tag{1.7}$$

$k$ is the *reduced frequency* $k = \frac{\omega b}{U}$ and $C(k) \in \mathbb{C}$ is the *Theodorsen function*, defined for the first time in [22]:

$$C(k) = \frac{K_1(jk)}{K_1(jk) + K_0(jk)} = F(k) + jG(k) \tag{1.8}$$

which is expressed in terms of the modified Bessel functions of the second kind of order zero ($K_0$) and one ($K_1$).

### 1.1.1 Computation of forces

Knowing the $\Delta C_p$ it is possible to compute the global forces acting on the airfoil. The lift (2D, so its dimensions are $\left[\frac{N}{m}\right]$) is equal to

$$L(t) = \frac{1}{2}\rho U^2 \int_{-b}^{b} \Delta C_p(x,t)\, dx \tag{1.9}$$

Since we only know $\Delta C_p(\theta, t)$, it is necessary to perform the aforementioned change of variable

$$L(t) = \frac{1}{2}\rho U^2 b \int_{0}^{\pi} \Delta C_p(\theta,t) \sin\theta\, d\theta \tag{1.10}$$

Exploiting the fact that

$$\int_0^\pi \sin n\theta \sin m\theta\, d\theta = \begin{cases} 0 & \text{if } m \neq n \\ \frac{\pi}{2} - \frac{\sin 2n\pi}{4n} & \text{if } m = n \end{cases} \tag{1.11}$$

$$\int_0^\pi \tan\frac{\theta}{2} \sin\theta\, d\theta = \pi \tag{1.12}$$

it is possible to see that

$$L(t) = \frac{1}{2}\rho U^2 4b\pi(a_0 + a_1)e^{j\omega t} \tag{1.13}$$

$$L(t) = \frac{1}{2}\rho U^2 (2b) 2\pi (C(k)(P_0 + P_1) + \frac{jk}{2}(P_0 - P_2))e^{j\omega t} \tag{1.14}$$

This result is very interesting because shows that the lift depends only on the first three upwash coefficients, independently from the kind of airfoil movement.

The moment about a generic point $x_0$ (2D, positive nose-up) is equal to

$$M_0(t) = -\frac{1}{2}\rho U^2 \int_{-b}^{b} (x - x_0)\Delta C_p(x,t)\, dx \tag{1.15}$$

Using the usual coordinate transformation, calling $\tilde{x}_0 = x_0/b$

$$M_0(t) = -\frac{1}{2}\rho U^2 b^2 \int_{0}^{\pi} (\cos\theta - \tilde{x}_0)\Delta C_p(\theta,t) \sin\theta\, d\theta \tag{1.16}$$

$$\begin{aligned} M_0(t) = -\frac{1}{2}\rho U^2 b^2 \Bigg( & 4a_0 \int_0^\pi \frac{1}{2}\tan\frac{\theta}{2}\sin 2\theta\, d\theta + \\ & + 8\sum_{n=1}^{\infty} a_n \int_0^\pi \frac{1}{2}\sin 2\theta \sin n\theta\, d\theta \Bigg) e^{j\omega t} + b\tilde{x}_0 L(t) \end{aligned} \tag{1.17}$$

Exploiting the fact that

$$\int_0^{\pi} \tan\frac{\theta}{2}\sin 2\theta\, d\theta = -\pi \tag{1.18}$$

it is possible to show that

$$M_0(t) = \frac{1}{2}\rho U^2 b^2 2\pi \left(a_0 - a_2 + 2\tilde{x}_0(a_0 + a_1)\right) e^{j\omega t} \tag{1.19}$$

Expressing the $a_n$ in terms of the upwash coefficients, it results

$$\begin{aligned} M_0(t) =& \frac{1}{2}\rho U^2 b^2 2\pi \Big( (1 + 2\tilde{x}_0)(C(k)(P_0 + P_1) - P_1) + \\ &+ 2\tilde{x}_0 \Big( P_1 + \frac{jk}{2}(P_0 - P_2) \Big) - P_2 - \frac{jk}{4}(P_1 - P_3) \Big) e^{j\omega t} \end{aligned} \tag{1.20}$$

As for the lift, the aerodynamic moment depends only on a limited number of upwash coefficients, as depends only on the first four, independently from the airfoil motion and the point $\tilde{x}_0$. Using as a reference point for the aerodynamic moment the quarter chord point, *i.e.* $\tilde{x}_0 = -1/2$, equation 1.20 can be simplified in

$$M_{c/4}(t) = -\frac{1}{2}\rho U^2 b^2 2\pi \left( P_1 + P_2 + \frac{jk}{2}\left( P_0 - P_2 + \frac{P_1 - P_3}{2} \right) \right) e^{j\omega t} \tag{1.21}$$

In this case the effect of the Theodorsen function is null as already verified by [22].

### 1.1.2 Computation of power

It is possible to compute the global instantaneous bi-dimensional power required to activate the system, *i.e.* to perform the perturbation movements

$$W(t) = \frac{1}{2}\rho U^2 \int_{-b}^{b} \Delta C_p(x,t) v'(x,t)\, dx \tag{1.22}$$

where $v'(x,t)$ is the speed of the airfoil with respect to the uniformly translating reference frame, namely the perturbation speed of the airfoil

$$v'(x,t) = \frac{\partial z}{\partial t} = \dot{z} \tag{1.23}$$

The computation of the power for the specific cases will be described in the next section.

## 1.2 Moving airfoil

If we consider an airfoil moving with the following law

$$z(x,t) = g(x)e^{j\omega t} \tag{1.24}$$

the speed of each point of the airfoil chord is

$$v(x,t) = \frac{dz}{dt} = \frac{\partial z}{\partial t} + \frac{\partial z}{\partial x}\frac{\partial x}{\partial t} = \frac{\partial z}{\partial t} + U\frac{\partial z}{\partial x} \tag{1.25}$$

$$v(x,t) = (j\omega g(x) + Ug'(x))e^{j\omega t} \tag{1.26}$$

Using the reduced frequency k and applying the transformation $x = b\cos\theta$

$$v(x,t) = \frac{U}{b}(jkg(x) + bg'(x))e^{j\omega t} \tag{1.27}$$

$$v(\theta,t) = \frac{U}{b}(jkg(\theta) + bg'(\theta)\frac{d\theta}{dx})e^{j\omega t} \tag{1.28}$$

$$v(\theta,t) = \frac{U}{b}(jkg(\theta) - \frac{1}{\sin\theta}g'(\theta))e^{j\omega t} \tag{1.29}$$

Hence

$$f(\theta)e^{j\varphi(\theta)} = \frac{U}{b}(jkg(\theta) - \frac{1}{\sin\theta}g'(\theta)) \tag{1.30}$$

that is a convenient form for the computation of the upwash coefficient in eq. 1.4.

### 1.2.1 Rigidly moving airfoil

Exploiting the linearity of the thin airfoils theory, it is now possible to compute the upwash coefficients independently for each different movement of the airfoil. Then each solution can be superposed to describe the desired motion of the airfoil. The following movements are considered here: a vertical translation, a pitch rotation, a flap rotation and a rotation of both flap and trim tab.

Considering a vertical translation, positive toward the top (while the Theodorsen convention is positive toward the bottom)

$$z(x,t) = he^{j\omega t} = \tilde{h}be^{j\omega t} \tag{1.31}$$

the function $g(x) = g(\theta) = \tilde{h}b$, so the velocity of the points of the airfoil is

$$v(\theta, t) = jkU\tilde{h}e^{j\omega t} \tag{1.32}$$

The upwash coefficients are

$$P_n = -\frac{jk}{\pi}\int_0^\pi \cos n\theta \, d\theta \tag{1.33}$$

and it results that

$$P_0 = -jk\tilde{h} \tag{1.34}$$
$$P_n = 0 \text{ for } n \neq 0 \tag{1.35}$$

As a result the total lift and the quarter-chord moment are

$$L(t) = \frac{1}{2}\rho U^2(2b)2\pi\left(\frac{k^2}{2} - jkC(k)\right)\tilde{h}e^{j\omega t} \tag{1.36}$$

$$M_{c/4}(t) = \frac{1}{2}\rho U^2 b^2 2\pi\frac{k^2}{2}\tilde{h}e^{j\omega t} \tag{1.37}$$

If we consider a pure rotation with respect to the point $x_p$, positive counterclockwise

$$z(x, t) = -(x - x_p)\alpha e^{j\omega t} \tag{1.38}$$

the function $g(\theta) = -b(\cos\theta - \tilde{x}_p)\alpha b$, so the velocity of the airfoil, with respect of the spatial variable $\theta$ is

$$v(\theta, t) = -U(jk(\cos\theta - \tilde{x}_p) + 1)\alpha e^{j\omega t} \tag{1.39}$$

The upwash coefficients are

$$P_n = \frac{1}{\pi}\alpha\int_0^\pi (jk(\cos\theta - \tilde{x}_p) + 1)\cos n\theta \, d\theta \tag{1.40}$$

and it results that

$$P_0 = (1 - jk\tilde{x}_p)\alpha \tag{1.41}$$
$$P_1 = \frac{jk}{2}\alpha \tag{1.42}$$
$$P_n = 0 \text{ for } n > 1 \tag{1.43}$$

Using this coefficients in equation 1.14 it is possible to compute the lift developed by an airfoil subject to a pitch oscillation

$$L(t) = \frac{1}{2}\rho U^2(2b)2\pi\left(C(k)\left((1 - jk\tilde{x}_p) + \frac{jk}{2}\right) + \frac{jk}{2}(1 - jk\tilde{x}_p)\right)\alpha e^{j\omega t} \tag{1.44}$$

It is also possible to compute the moment with respect to $c/4$, *i.e.* $\tilde{x}_0 = -1/2$ using eq. 1.21

$$M_{c/4}(t) = -\rho U^2 b^2 \pi \left( \frac{jk}{2} + \frac{jk}{2} \left( (1 - jk\tilde{x}_p) + \frac{jk}{4} \right) \right) \alpha e^{j\omega t} \tag{1.45}$$

### 1.2.2 Flap rotation

Let us consider a flap rotating around a hinge placed at the point $x_F$

$$z(x,t) = \begin{cases} 0 & \text{if } x \leq x_F \\ -(x - x_F)\beta e^{j\omega t} & \text{if } x > x_F \end{cases} \tag{1.46}$$

applying the usual coordinate transformation

$$z(\theta,t) = \begin{cases} 0 & \text{if } \theta \geq \theta_F \\ -b(\cos\theta - \tilde{x}_F)\beta e^{j\omega t} & \text{if } \theta < \theta_F \end{cases} \tag{1.47}$$

with $\theta_F = \arccos(\tilde{x}_F)$ and $\tilde{x}_F = x_F/b$. Hence the velocity of the airfoil is

$$v(\theta,t) = \begin{cases} 0 & \text{if } \theta \geq \theta_F \\ -U(jk(\cos\theta - \tilde{x}_F)\beta e^{j\omega t} & \text{if } \theta < \theta_F \end{cases} \tag{1.48}$$

Also in this case it is possible to compute the upwash coefficients

$$P_n = \frac{1}{\pi}\beta \int_0^{\theta_F} (jk(\cos\theta - \tilde{x}_F) + 1)\cos n\theta \, d\theta \tag{1.49}$$

$$P_n = \frac{1}{\pi}\beta \Big( \int_0^{\theta_F} jk\cos\theta\cos n\theta \, d\theta + \int_0^{\theta_F} (1 - jk\tilde{x}_F)\cos n\theta \, d\theta \Big) \tag{1.50}$$

It results that

$$P_0 = \Big( \frac{jk}{\pi}\sqrt{1 - \tilde{x}_F^2} + (1 - jk\tilde{x}_F)\frac{\theta_F}{\pi} \Big)\beta \tag{1.51}$$

$$P_n = \frac{jk}{\pi(n^2 - 1)} \Big( n\tilde{x}_F \sin n\theta_F - \sqrt{1 - \tilde{x}_F^2}\cos n\theta_F \Big)\beta + \\ + \frac{1}{n\pi}(1 - jk\tilde{x}_F)\sin n\theta_F \, \beta \tag{1.52}$$

Unlike the case of a movement involving the whole airfoil, the series is composed by an infinite number of terms, that decay as $1/n$ and $1/n^2$. However, it is useful to remind that only the first three coefficients are important to

evaluate the lift, and only the first four term if we want to compute also the moment.

It is important to notice that the term $P_1$ has an indetermination of the type $\frac{0}{0}$, hence it needs to be computed by a limit operation

$$P_1 \to \frac{jk}{2\pi}\left(\frac{\sin 2\theta_F}{2} + \theta_F\right) \tag{1.53}$$

The hinge moment is equal to the moment about the hinge point due to the pressure distribution on the flap surface:

$$M_F(t) = -\frac{1}{2}\rho U^2 b^2 \int_0^{\theta_F} (\cos\theta - \tilde{x}_F)\Delta C_p(\theta, t)\sin\theta\, d\theta \tag{1.54}$$

$$M_F(t) = -\frac{1}{2}\rho U^2 b^2 \int_0^{\theta_F} (\cos\theta - \tilde{x}_F)\left(4a_0 \tan\frac{\theta}{2} + 8\sum_{n=1}^{\infty} a_n \sin n\theta\right)\sin\theta\, d\theta\, e^{j\omega t} \tag{1.55}$$

This integral can be solved exploiting the prosthaphaeresis formulae and the half-angle formulae, ad it results

$$\begin{aligned} M_F(t) = &-\frac{1}{2}\rho U^2 b^2 2a_0\left((2+\tilde{x}_F)\sqrt{1-\tilde{x}_F^2} - (1+2\tilde{x}_F)\theta_F\right)e^{j\omega t} + \\ &+ \frac{1}{2}\rho U^2 b^2 \sum_{n=1}^{\infty} \frac{8a_n\tilde{x}_F}{n^2-1}\left(\tilde{x}_F \sin n\theta_F - n\sqrt{1-\tilde{x}_F^2}\cos n\theta_F\right)e^{j\omega t} + \\ &+ \frac{1}{2}\rho U^2 b^2 \sum_{n=1}^{\infty} 2a_n\left(\frac{\sin\big((n+2)\theta_F\big)}{n+2} - \frac{\sin\big((n-2)\theta_F\big)}{n-2}\right)e^{j\omega t} \end{aligned} \tag{1.56}$$

The hinge moment depends on all of the coefficients $a_n$, and therefore from all of the upwash coefficients. Hence, in order to obtain a numerical value of the hinge moment, the series needs to be truncated.

In this case the first term of the first summation and the second term of the second summation are undetermined, therefore must be computed performing a limit operation

$$\begin{aligned} &\lim_{n\to 1} \frac{8a_n\tilde{x}_F}{n^2-1}\left(\tilde{x}_F \sin n\theta_F - n\sqrt{1-\tilde{x}_F^2}\cos n\theta_F\right) = \\ &\quad = -8a_n\tilde{x}_F\frac{1}{2}\left(\frac{\sin 2\theta_F}{2} - \theta_F\right) \end{aligned} \tag{1.57}$$

$$\lim_{n\to 2} 2a_n\left(\frac{\sin\big((n+2)\theta_F\big)}{n+2} - \frac{\sin\big((n-2)\theta_F\big)}{n-2}\right) = 2a_n\left(\frac{\sin\big(4\theta_F\big)}{4} - \theta_F\right) \tag{1.58}$$

### 1.2.3 Flap and trim tab rotation

Let us consider a movement of the type

$$z(x,t) = \begin{cases} 0 & \text{if } x \le x_{F_0} \\ -(x - x_{F_0})\beta_0 e^{j\omega t} & \text{if } x_{F_0} < x \le x_{F_1} \\ -(x - x_{F_0})\beta_0 e^{j\omega t} - (x - x_{F_1})\beta_1 e^{j\omega t} & \text{if } x > x_{F_1} \end{cases} \quad (1.59)$$

with $x_{F1} > x_{F0}$. With the usual steps the speed can be calculated

$$v(\theta,t) = \begin{cases} 0 & \text{if } \theta \ge \theta_{F_0} \\ -U(jk(\cos\theta - \tilde{x}_{F_0}) + 1)\beta_0 e^{j\omega t} & \text{if } \theta_{F_0} > \theta \ge \theta_{F_1} \\ -U((jk(\cos\theta - \tilde{x}_{F_0}) + 1)\beta_0 + & \\ \quad +(jk(\cos\theta - \tilde{x}_{F_1}) + 1)\beta_1)e^{j\omega t} & \text{if } \theta < \theta_{F_1} \end{cases} \quad (1.60)$$

with $\theta_{F_0} = \arccos(\tilde{x}_{F_0})$ and $\theta_{F_1} = \arccos(\tilde{x}_{F_1})$ Exploiting the linearity, since the velocity distribution is a superposition of the effects of two rotations, with the second being relative to the first one,it can be seen that the upwash coefficients related to the flap movement $\beta_0$ are identical to the ones computed in the previous section for the variable $\beta$. Hence, for the only tab rotation $\beta_1$, it is easy to see that the upwash coefficients have the same form as those already computed for the flap, changing $\tilde{x}_{F_0}$ into $\tilde{x}_{F_1}$ and $\theta_{F_0}$ into $\theta_{F_1}$. So

$$P_0 = \left(\frac{jk}{\pi}\sqrt{1 - \tilde{x}_{F_1}^2} + (1 - jk\,\tilde{x}_{F_1})\frac{\theta_{F_1}}{\pi}\right)\beta_1 \quad (1.61)$$

$$P_n = \frac{jk}{\pi(n^2-1)}\left(n\,\tilde{x}_{F_1}\sin n\,\theta_{F_1} - \sqrt{1 - \tilde{x}_{F_1}^2}\cos n\,\theta_{F_1}\right)\beta_1 + \\ + \frac{1}{n\pi}(1 - jk\,\tilde{x}_{F_1})\sin n\,\theta_{F_1}\ \beta_1 \quad (1.62)$$

Also in this case $P_1$ must be computed by a limit like in 1.53.

### 1.2.4 Deforming airfoil

Using the approach described in section 1.2.3, it is possible to represent a deforming airfoil as a sequence of $N_F$ straight lines each one rotating with respect to the previous one by a relative angle $\beta_i$. In this way it is possible to approximate any shape and any camber variation using a closed form analytical solution that tends to the exact solution as $N_F \to \infty$

### 1.2.5 Computation of power

As seen in sec. 1.1.2, in order to compute the aerodynamic power it is necessary to know the perturbation velocity $v'(x,t)$. Since we are in a linearized framework, it is possible to write

$$v'(x,t) = v'_{\tilde{h}} + v'_{\alpha} + v'_{\beta} + v'_{\beta_1} + \text{etc.} \tag{1.63}$$

so we can calculate each member separately starting from the $z(x,t)$ laws given in the previous sections

$$v'_{\tilde{h}}(x,t) = j\omega b\tilde{h}e^{j\omega t} = v'_{\tilde{h}}(t) \tag{1.64}$$

$$v'_{\alpha}(x,t) = -j\omega(x-x_p)\alpha e^{j\omega t} \tag{1.65}$$

$$v'_{\beta}(x,t) = \begin{cases} 0 & \text{if } x \le x_F \\ -j\omega(x-x_F)\beta e^{j\omega t} & \text{if } x > x_F \end{cases} \tag{1.66}$$

$$v'_{\beta_1}(x,t) = \begin{cases} 0 & \text{if } x \le x_{F_1} \\ -j\omega(x-x_{F_1})\beta_1 e^{j\omega t} & \text{if } x > x_{F1} \end{cases} \tag{1.67}$$

Exploiting the linearity it is possible to compute the power separately for each degree of freedom

$$\begin{aligned} W_{\tilde{h}}(t) &= \frac{1}{2}\rho U^2 \int_{-b}^{b} \Delta C_p(x,t) v'_{\tilde{h}}(t)\, dx = \\ &= \frac{1}{2}\rho U^2 \int_{-b}^{b} \Delta C_p(x,t)\, dx v'_{\tilde{h}}(t) = L(t)\dot{h} \end{aligned} \tag{1.68}$$

$$\begin{aligned} W_{\alpha}(t) &= \frac{1}{2}\rho U^2 \int_{-b}^{b} \Delta C_p(x,t) v'_{\alpha}(t)\, dx = \\ &= \frac{1}{2}\rho U^2 \int_{-b}^{b} -(x-x_p)\Delta C_p(x,t)\, dx\, j\omega\alpha e^{j\omega t} = M_{c/4}(t)\dot{\alpha} \end{aligned} \tag{1.69}$$

$$\begin{aligned} W_{\beta}(t) &= \frac{1}{2}\rho U^2 \int_{-b}^{b} \Delta C_p(x,t) v'_{\beta}(t)\, dx = \\ &= \frac{1}{2}\rho U^2 \int_{x_F}^{b} -(x-x_F)\Delta C_p(x,t)\, dx\, j\omega\beta e^{j\omega t} = M_F(t)\dot{\beta} \end{aligned} \tag{1.70}$$

$$\begin{aligned} W_{\beta_1}(t) &= \frac{1}{2}\rho U^2 \int_{-b}^{b} \Delta C_p(x,t) v'_{\beta_1}(t)\, dx = \\ &= \frac{1}{2}\rho U^2 \int_{x_{F_1}}^{b} -(x-x_{F_1})\Delta C_p(x,t)\, dx\, j\omega\beta_1 e^{j\omega t} = M_{F_1}(t)\dot{\beta}_1 \end{aligned} \tag{1.71}$$

and so on for other possible flaps. Therefore the total power is

$$W(t) = L(t)\dot{h} + M_{c/4}(t)\dot{\alpha} + \sum_{k=1}^{N_F} M_{F_k}\dot{\beta}_k \tag{1.72}$$

### 1.2.6 Comparison with Glauert theory

The Küssner and Schwarz theory is to be included in the framework of unsteady thin airfoils theories. Considering the limit for $\omega \to 0$, with $\omega$ the oscillation frequency, leads to the steady case, whose behaviour must be similar to the classical thin airfoils theory.

One way to verify the exact convergence of the pressure difference distribution over the airfoil for the steady case is to compare it to the one developed by Glauert in [11] and [12] and summarized by Allen in [14]. In his work Glauert managed to compute the contributions to the difference of pressure distribution due to the angle of incidence ad the deflections of serially hinged flaps.

It is necessary to take into account that Glauert's notation and reference system is different from the one used in this work. In fact he calls the chord $c = 2b$ and his airfoil is contained in the interval $[0, c]$, with the origin placed at the leading edge. Therefore the change of variables needed for the airfoil to pass to $[0, \pi]$ is $\theta = \arccos\Big(1 - \frac{2x}{c}\Big)$. The transformed hinge point is then

$$\theta_0 = \arccos\Big(1 - \frac{2x_F^{\mathrm{Gla}}}{c}\Big) = \arccos\Big(1 - 2E\Big) \tag{1.73}$$

with $x_F^{\mathrm{Gla}} = b + x_F$ and where $E = \frac{b - x_F}{c}$ is the flap-chord ratio

The pressure difference contributions caused by the incidence and the flap deflection are

$$\Delta C_{p_\alpha} = \frac{4(1 + \cos\theta)}{\sin\theta}\alpha \tag{1.74}$$

$$\Delta C_{p_\beta} = \Big[\frac{4(1 + \cos\theta)(\pi - \theta_0)}{\pi \sin\theta} + \sum_{n=1}^{\infty} 8\frac{\sin n\theta_0 \sin n\theta}{n\pi}\Big]\beta \tag{1.75}$$

And the contributions of further flaps share the same formula with the first flap, provided that $\theta_0$ and $\beta$ are the values assumed by each flap. Superposing every contribution it is possible to obtain the global pressure difference coefficient

$$\Delta C_p = \Delta C_{p_\alpha} + \sum_{k=1}^{N_F} \Delta C_{p_{\beta_k}} \tag{1.76}$$

The result of this theory can be used to verify the exact convergence of the pressure distribution of the Küssner and Schwarz model adopted in this work at least for the steady solution. It can be noticed in Figure1.1 that the two distribution essentially coincide, if the number of terms taken into account is enough (*e.g.* $N_P = 1000$). Both the theories show a singularity

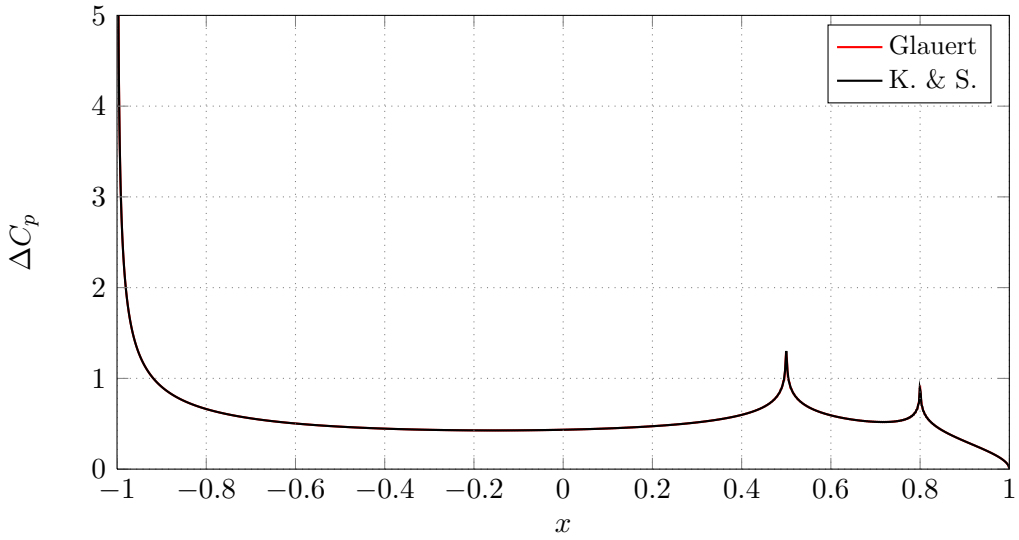


FIGURE 1.1. Pressure difference distribution, steady case, $N_P = 1000$ with both flaps deflected

in the pressure at the leading-edge, and both respect the Kutta condition at the trailing-edge, where the pressure difference is null.

It is noticeable that singularities arise also at the hinge points whenever a flap deflection is not null. This is related to the fact that each hinge is a point of non-smoothness in the speed. These discontinuities are the cause of the relatively high number of terms necessary for the series to converge. In fact a lower number of terms would cause the pressure difference profile to show some oscillations especially in the proximity of these points (see the Fourier series of an impulse for example and Figure 1.2). The forces and the power, as will be shown in 1.2.7, suffer less this problem because of the integration operation that smoothens the effect of these essential discontinuities.

### 1.2.7 Comparison with Theodorsen theory

Since Küssner and Schwarz theory shares the same starting assumptions with Theodorsen theory, a comparison can be performed to verify its exactness and convergence of the lift and the moments.

Let us start by examining the classic case of a pitching and plunging airfoil. The lift associated with both degrees of freedom have already been

computed in equations 1.36 and 1.44. Superposing the two effects we obtain

$$L(t) = \frac{1}{2}\rho U^2(2b)2\pi\left[\left(\frac{k^2}{2} - jkC(k)\right)\tilde{h} + \right. \\ \left. + \left(C(k)\left((1 - jk\tilde{x}_p) + \frac{jk}{2}\right) + \frac{jk}{2}(1 - jk\tilde{x}_p)\right)\alpha\right]e^{j\omega t} \tag{1.77}$$

With some simple steps and remembering that, with a little abuse of notation, $k^2\tilde{h}e^{j\omega t} = -b\frac{\ddot{h}}{U^2}$, $jk\tilde{h}e^{j\omega t} = \frac{\dot{h}}{U}$, $k^2\alpha e^{j\omega t} = -\frac{b^2}{U^2}\ddot{\alpha}$ and $jk\alpha e^{j\omega t} = \frac{b}{U}\dot{\alpha}$ it can be written

$$L(t) = \rho b^2\pi\left(-\ddot{h} + U\dot{\alpha} - b\tilde{x}_p\ddot{\alpha}\right) + \\ + \rho U b 2\pi C(k)\left(-\dot{h} + U\alpha + b\left(\frac{1}{2} - \tilde{x}_p\right)\dot{\alpha}\right) \tag{1.78}$$

that is the classical formulation of Theodorsen theory for oscillating airfoil, distinguishing the circulatory contribution, which depends on the Theodorsen function, and the non-circulatory part.

The same procedure can be applied to the moment, summing up eq. 1.37 and 1.45 we get

$$M_{c/4}(t) = \rho U^2 b^2\pi\left[\frac{k^2}{2}\tilde{h} - \left(\frac{jk}{2} + \frac{jk}{2}\left((1 - jk\tilde{x}_p) + \frac{jk}{4}\right)\right)\alpha\right]e^{j\omega t} \tag{1.79}$$

covering then the same steps as for the lift, it is possible to write the moment in the following form

$$M_{c/4}(t) = -\rho b^2\pi\left(\frac{\ddot{h}}{2} + Ub\dot{\alpha} + b^2\left(\frac{1}{8} - \frac{\tilde{x}_p}{2}\right)\ddot{\alpha}\right) \tag{1.80}$$

confirming the equality with Theodorsen' s classical results. It can be noticed that the quarter-chord aerodynamic moment does not depend on the Theodorsen function.

It is worthwhile to take into account for the comparison also the flaps deflections and their contribution to the values of the lift and the quarter-chord moment. Theodorsen expressed them in [23] in the following way:

$$P = -\pi\rho\omega^2 b^3\left(\tilde{h}A_{ch} + \alpha A_{c\alpha} + \beta A_{c\beta} + \gamma A_{c\gamma}\right) \tag{1.81}$$

$$M_\alpha = -\pi\rho\omega^2 b^4\left(\tilde{h}A_{ah} + \alpha A_{a\alpha} + \beta A_{a\beta} + \gamma A_{a\gamma}\right) \tag{1.82}$$

where $A_{ch} = R_{ch} + jI_{ch}$, $A_{c\alpha} = R_{c\alpha} + jI_{c\alpha}$, etc. The constants are reported in Appendix B. It is important to notice the difference of notation $\gamma = \beta_1$, and that the moment is referred to the rotation point. This is not a problem if we consider the quarter-chord point as rotation center, like we have always done.

Although these movements are associated to an infinite series of upwash coefficients (see equation 1.51), since the lift and the moment in Küssner and Schwarz theory depend only on a finite number of upwash coefficients, they are expected to assume the same value of the ones in Theodorsen's theory. This fact can be proved both analytically and numerically, by computing the values for the same data and checking that the results are the same. In the first case it can be helpful the employment of a software like *Wolfram Mathematica*, because there are long and tedious steps to be carried out and it can be easy to make little mistakes. It is essential to notice that there are some differences in sign conventions between the ones used in this work and Theodorsen's ones. He considered the airfoil translation and the lift positive downward, while here plunge movements and lift are taken positive if upward. In both theories moments and angle are considered positive if clockwise. This causes the angles contribution to the lift and the plunge effect on the the moment to have different signs.

The last comparisons left to be made are the hinge moment. Accordingly to Theodorsen in [23];

$$M_\beta = -\pi\rho\omega^2 b^4\Big(\tilde{h}A_{bh} + \alpha A_{b\alpha} + \beta A_{b\beta} + \gamma A_{b\gamma}\Big) \tag{1.83}$$

$$M_\gamma = -\pi\rho\omega^2 b^4\Big(\tilde{h}A_{dh} + \alpha A_{d\alpha} + \beta A_{d\beta} + \gamma A_{d\gamma}\Big) \tag{1.84}$$

In this case an exact equivalence with Theodorsen theory is not going to be obtained, as Küssner and Schwarz result (equation 1.56) is composed by an infinite series that needs to be truncated in order to obtain a numerical solution. Nevertheless it is possible to numerically prove the convergence for an increasing number of upwash coefficients kept into account. For a number $N_P = 100$ of upwash coefficients it is possible to see that the difference between the two theories stays below the 1% for different combination of angles with $\alpha, \beta, \beta_1 \in [-20, 20]$ (see Table 1.1).

Plotting the pressure distribution obtained with Küssner and Schwarz theory for $N_P = 100$, it can be seen (figure 1.2) that it is not as sharp as the one displayed in figure 1.1 and it is not able to represent the singularities as in detail. This is due to the number of terms used for the evaluation of the series, which is not sufficient to render the correct pressure profile. However, it is sufficient to compute the forces, obtained by integrating the difference of pressure distribution, an operation that smoothens the effects of singularities,

| Errors [%] | $[2^\circ, 5^\circ, 5^\circ]$ | $[2^\circ, -5^\circ, 5^\circ]$ | $[10^\circ, 20^\circ, 20^\circ]$ | $[10^\circ, -20^\circ, 20^\circ]$ |
|---|---|---|---|---|
| $\lvert M_f \rvert$ | 0.01063 | 0.041356 | 0.010445 | 0.038792 |
| phase$(M_f)$ | 0.000142 | 0.000312 | 0.000153 | 0.000483 |
| $\lvert M_{f_1} \rvert$ | 0.037567 | 0.137011 | 0.036851 | 0.128367 |
| phase$(M_{f_1})$ | 0.000745 | 0.001784 | 0.000784 | 0.002330 |

TABLE 1.1. Percentage differences between Theodorsen and Küssner and Schwarz theories, $N_P = 100$, at different configurations $[\alpha, \beta, \beta_1]$, with $k = 0.1$

making them less influential. However, for further application, it is possible to consider a higher number of upwash coefficients ($N_P = 1000$), to have a good pressure difference representation if necessary, since the computational cost is very low.

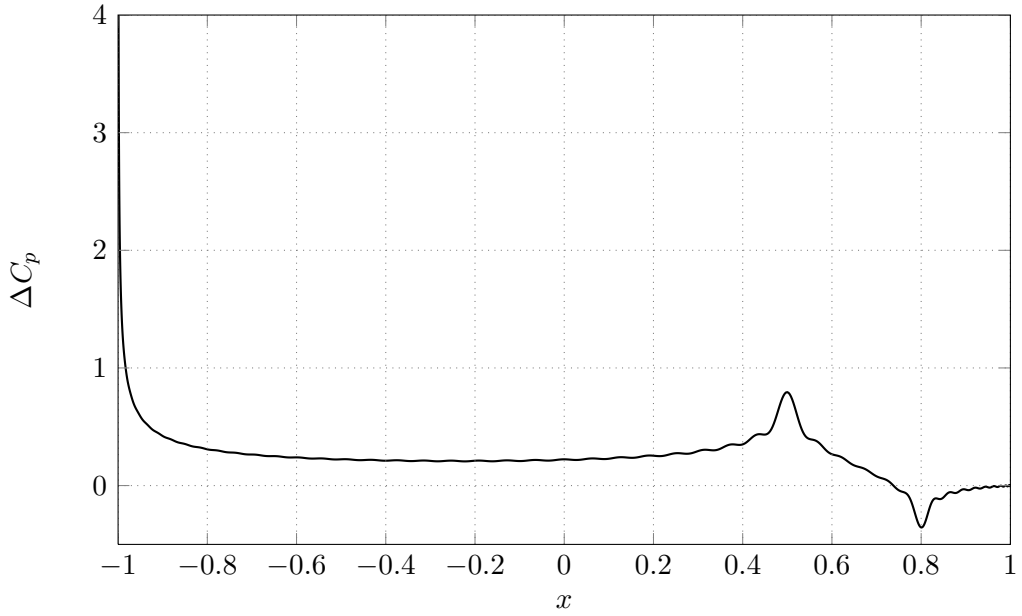


FIGURE 1.2. Example of Küssner and Schwarz pressure difference distribution, $N_P = 100$

## 1.3 Piecewise cubic mean-line

In order to describe the motion of a deforming airfoil another possibility is to describe its mean line as a cubic, or more generally as a continuous piecewise cubic with continuous first derivative, *i.e.* a cubic spline. Since

this approach generates a hingeless change in the airfoil camber, it avoids the creation of singularities in the pressure distribution located at the hinge points and should guarantee a smaller number of terms for the series to converge. The smoother shape assumed by the camberline with this method is also more representative of the deformation of a morphing blade.

A possible way to describe a harmonically oscillating cubic spline is

$$z(x,t) = \begin{cases} \mathcal{P}_0(x)e^{j\omega t} & \text{if } x < x_{F_0} \\ (\mathcal{P}_0(x) + \mathcal{P}_1(x))e^{j\omega t} & \text{if } x_{F_0} \leq x < x_{F_1} \\ (\mathcal{P}_0(x) + \mathcal{P}_1(x) + \mathcal{P}_2(x))e^{j\omega t} & \text{if } x_{F_1} \leq x < x_{F_2} \\ ... \end{cases} \tag{1.85}$$

where the shape functions are cubic polynomials $\mathcal{P}_k(x) = A_k x^3 + B_k x^2 + C_k x + D_k$, with $A_k, B_k, C_k, D_k \in \mathbb{R}$. To obtain a continuous shape it has to be imposed that $\mathcal{P}_k(x_{F_k}) = \mathcal{P}_{k+1}(x_{F_k})$ for each $k$. A more desirable smooth shape can be achieved by imposing also the continuity of the first derivative $\mathcal{P}'_k(x_{F_k}) = \mathcal{P}'_{k+1}(x_{F_k})$, with $\mathcal{P}'_k(x) = \frac{d\mathcal{P}_k}{dx} = 3A_k x^2 + 2B_k x + C_k$.

It is possible to compute the velocity of the airfoil as usual

$$v(x,t) = \begin{cases} \frac{U}{b}\Big(jk\mathcal{P}_0(x) + b\mathcal{P}'_0(x)\Big)e^{j\omega t} & \text{if } x < x_{F_0} \\ \frac{U}{b}\Big[jk(\mathcal{P}_0(x) + \mathcal{P}_1(x)) + b(\mathcal{P}'_0(x) + \mathcal{P}'_1(x))\Big]e^{j\omega t} & \text{if } x_{F_0} \leq x < x_{F_1} \\ \frac{U}{b}\Big[jk(\mathcal{P}_1(x) + \mathcal{P}_2(x) + \mathcal{P}_3(x)) + & \\ \quad + b(\mathcal{P}'_1(x) + \mathcal{P}'_2(x) + \mathcal{P}'_3(x))\Big]e^{j\omega t} & \text{if } x_{F_1} \leq x < x_{F_2} \\ ... & \end{cases} \tag{1.86}$$

Calling $v_k(x,t) = \frac{U}{b}\Big(jk\mathcal{P}_k(x) + b\mathcal{P}'_k(x)\Big)e^{j\omega t}$, it can be rewritten as

$$v(x,t) = \begin{cases} v_0(x,t) & \text{if } x < x_{F_0} \\ v_0(x,t) + v_1(x,t) & \text{if } x_{F_0} \leq x < x_{F_1} \\ v_0(x,t) + v_1(x,t) + v_2(x,t) & \text{if } x_{F_1} \leq x < x_{F_2} \\ ... \end{cases} \tag{1.87}$$

Then, by applying the change of variables $x = b\cos\theta$, it is possible to compute the upwash coefficients. This operation will be performed later for each term, since the general expression can always be built exploiting the linearity and the superposition of a cubic mean-line solution with cubic flaps.

### 1.3.1 Cubic mean-line

A simple model to represent the deformation of an airfoil is to represent its mean-line as a cubic polynomial. In order to be coherent with the notation of the case of the airfoil with a flap and a tab, the rotation (*i.e.* the first derivative) and the deformation should be referred to a point $x_p$. This means that the vertical displacement could be written as follows

$$z(x,t) = \left[\bar{A}\Big(\frac{x-x_p}{b}\Big)^3 + \bar{B}\Big(\frac{x-x_p}{b}\Big)^2 + \bar{C}\Big(\frac{x-x_p}{b}\Big) + \bar{D}\right] e^{j\omega t} \tag{1.88}$$

In this way it is simple to notice that the $\bar{C}$ and $\bar{D}$ coefficients can be connected to the plunge and the pitch rotation movements described in section 1.2 (omitting time dependency)

$$z(x_p) = \bar{D} = h \tag{1.89}$$

$$z'(x_p) = \frac{\bar{C}}{b} = -\alpha \tag{1.90}$$

therefore

$$\bar{D} = b\tilde{h} \tag{1.91}$$

$$\bar{C} = -b\alpha \tag{1.92}$$

and then, neglecting the quadratic and the cubic terms, it can be recovered the movement of a pitching and plunging airfoil written with the usual variables

$$z(x,t) = \Big[b\tilde{h} - \alpha(x-x_p)\Big] e^{j\omega t}. \tag{1.93}$$

It is possible to expand the powers of the binomials and to collect the terms with the same polynomial degree in order to obtain a simpler form, useful for the upwash coefficients computation (temporarily omitting the time exponential)

$$\begin{aligned} z(x) =& \frac{\bar{A}}{b^3}x^3 + \Big(\frac{\bar{B}}{b^2} - 3x_p\frac{\bar{A}}{b^3}\Big)x^2 + \Big(\frac{\bar{C}}{b} - 2x_p\frac{\bar{B}}{b^2} + 3x_p^2\frac{\bar{A}}{b^3}\Big)x + \\ &+ \Big(\bar{D} - x_p\frac{\bar{C}}{b} + x_p^2\frac{\bar{B}}{b^2} - x_p^3\frac{\bar{A}}{b^3}\Big) \end{aligned} \tag{1.94}$$

and naming

$$A = \frac{\bar{A}}{b^3} \tag{1.95}$$

$$B = \frac{\bar{B}}{b^2} - 3x_p\frac{\bar{A}}{b^3} \tag{1.96}$$

$$C = \frac{\bar{C}}{b} - 2x_p\frac{\bar{B}}{b^2} + 3x_p^2\frac{\bar{A}}{b^3} \tag{1.97}$$

$$D = \bar{D} - x_p\frac{\bar{C}}{b} + x_p^2\frac{\bar{B}}{b^2} - x_p^3\frac{\bar{A}}{b^3} \tag{1.98}$$

we obtain

$$\begin{aligned} z(x,t) &= (Ax^3 + Bx^2 + Cx + D)e^{j\omega t} \\ &= \mathcal{P}(x)e^{j\omega t} \end{aligned} \tag{1.99}$$

that is the general cubic shape function described at the beginning of this section.

Having this simpler expression for the motion of the airfoil, it is now possible to compute its velocity

$$\begin{aligned} v(x,t) &= \frac{U}{b}\Big(jk\mathcal{P}(x) + b\mathcal{P}'(x)\Big)e^{j\omega t} \\ &= \frac{U}{b}\Big[jk(Ax^3 + Bx^2 + Cx + D) + b(3Ax^2 + 2Bx + C)\Big]e^{j\omega t} \end{aligned} \tag{1.100}$$

As usual, it is now required to perform the change of variables $x = b\cos\theta$. Collecting the cosines with the same exponent we obtain

$$\begin{aligned} v(\theta,t) =& \frac{U}{b}\Big[jkAb^3\cos^3\theta + (jkBb^2 + 3Ab^3)\cos^2\theta + \\ &+ (jkCb + 2Bb^2)\cos\theta + (jkD + Cb)\Big]e^{j\omega t} \end{aligned} \tag{1.101}$$

Referring to equation 1.4 it is possible to compute the upwash coefficients

$$\begin{aligned} P_n =& -\frac{jkAb^3}{\pi b}\int_0^\pi \cos^3\theta\cos n\theta\, d\theta - \frac{jkBb^2 + 3Ab^3}{\pi b}\int_0^\pi \cos^2\theta\cos n\theta\, d\theta + \\ &- \frac{jkCb + 2Bb^2}{\pi b}\int_0^\pi \cos\theta\cos n\theta\, d\theta - \frac{jkD + Cb}{\pi b}\int_0^\pi \cos n\theta\, d\theta \end{aligned} \tag{1.102}$$

Each integral can be solved by exploiting the trigonometric identities, obtaining the following coefficients

$$P_0 = -\frac{3b^2}{2}A - \frac{jkb}{2}B - C - \frac{jk}{b}D \tag{1.103}$$

$$P_1 = -\frac{3jkb^2}{8}A - bB - \frac{jk}{2}C \tag{1.104}$$

$$P_2 = -\frac{3b^2}{4}A - \frac{jkb}{4}B \tag{1.105}$$

$$P_3 = -\frac{jkb^2}{8}A \tag{1.106}$$

$$P_n = 0 \text{ if } n > 3 \tag{1.107}$$

At this point the lift and the aerodynamic moment are easily computable with the relations 1.14 and 1.21.

The simplified formula for the computation of power used in the flaps case is no longer valid, so it must be deduced starting from its definition.

$$W(t) = \frac{1}{2}\rho U^2 \int_{-b}^{b} \Delta C_p(x,t) v'(x,t)\, dx \tag{1.108}$$

with

$$v'(x,t) = \frac{\partial z}{\partial t} = \dot{z} = j\omega \mathcal{P}(x) e^{j\omega t} \tag{1.109}$$

Substituting it in the definition of power and passing from $x$ to $\theta$ we have

$$W(t) = \frac{1}{2}\rho U^2 bj\omega \int_0^{\pi} \Delta C_p(\theta,t)\mathcal{P}(\theta)\sin\theta\, d\theta\, e^{j\omega t} \tag{1.110}$$

expressing the $\Delta C_p$ as in equation 1.5 and $\mathcal{P}(x)$ as described before

$$\begin{aligned} W(t) =& \frac{1}{2}\rho U^2 bj\omega \int_0^{\pi} \left(4a_0 \tan\frac{\theta}{2} + 8\sum_{n=1}^{\infty} a_n \sin n\theta\right)(Ab^3\cos^3\theta + \\ &+ Bb^2\cos^2\theta + Cb\cos\theta + D)\sin\theta\, d\theta\, e^{j2\omega t} \end{aligned} \tag{1.111}$$

once this eight integrals have been computed (see Appendix A), the final expression of the aerodynamic power is

$$\begin{aligned} W(t) =& \frac{1}{2}\rho U^3 jk \left[4a_0\pi\left(-\frac{3b^3}{8}A + \frac{b^2}{2}B - \frac{b}{2}C + D\right) + \right. \\ &+ 8\pi a_1\left(\frac{b^2}{8}B + \frac{1}{2}D\right) + 8\pi a_2\left(\frac{b^3}{8}A + \frac{b}{4}C\right) + \\ &\left. + 8\pi a_3\frac{b^2}{8}B + 8\pi a_4\frac{b^3}{16}A\right] e^{j2\omega t} \end{aligned} \tag{1.112}$$

Because this simple cubic deformation involves the whole mean line of the airfoil, it can be noticed that there exist a finite number of non-null upwash coefficients and that the power can be expressed in an exact form, like for the plunge and pitch movements.

### 1.3.2 Cubic Flap

Similarly to section 1.2.2, in which a flap rotation to be superposed to a global airfoil movement has been analyzed, in this section a cubic partial deformation of the mean-line will be examined. When superposed to the global cubic deformation, this corresponds to a piecewise cubic solution with two pieces (see Figure 1.3).

Unlike the conventional flap, this one is not allowed to perform a rotation around a hinge point, but can only deform with a parabolic and a cubic terms, because a first derivatives continuity constraint is to be imposed to obtain the desired smoothness. This can be easily achieved by writing the vertical displacement in the following way

$$z(x,t) = \begin{cases} 0 & \text{if } x \leq x_F \\ \left[ \bar{A}_1 \left( \frac{x-x_F}{b} \right)^3 + \bar{B}_1 \left( \frac{x-x_F}{b} \right)^2 \right] e^{j\omega t} & \text{if } x > x_F \end{cases} \tag{1.113}$$

expanding the powers we obtain

$$z(x,t) = \begin{cases} 0 & \text{if } x \leq x_F \\ \Big( A_1 x^3 + B_1 x^2 + C_1 x + D_1 \Big) e^{j\omega t} = \mathcal{P}_1(x) e^{j\omega t} & \text{if } x > x_F \end{cases} \tag{1.114}$$

having named the coefficients:

$$A_1 = \frac{\bar{A}_1}{b^3} \tag{1.115}$$

$$B_1 = -3\frac{\bar{A}_1}{b^3} x_F + \frac{\bar{B}_1}{b^2} \tag{1.116}$$

$$C_1 = 3\frac{\bar{A}_1}{b^3} x_F^2 - 2\frac{\bar{B}_1}{b^2} x_F \tag{1.117}$$

$$D_1 = -\frac{\bar{A}_1}{b^3} x_F^3 + \frac{\bar{B}_1}{b^2} x_F^2 \tag{1.118}$$

It is also possible to choose to impose the continuity in the second derivative of the cubic spline, in order to allow a greater regularity in the mean-line shape, and consequently to obtain a smoother pressure difference, as its distribution is quite influenced by the curvature of the camberline. This can

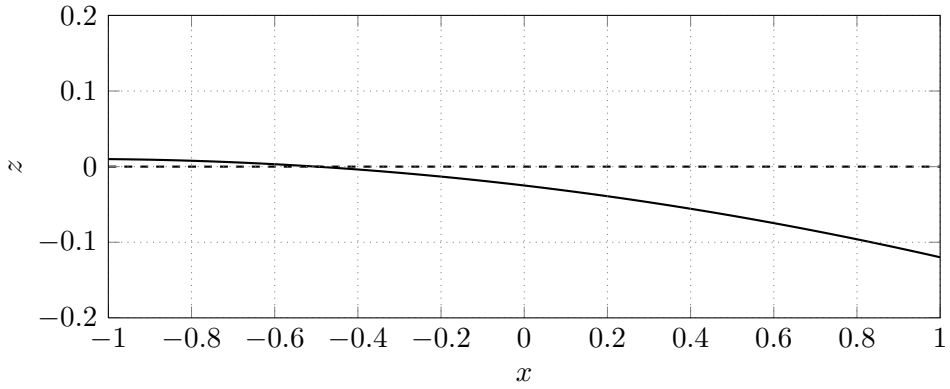


(A) First step: cubic deformation

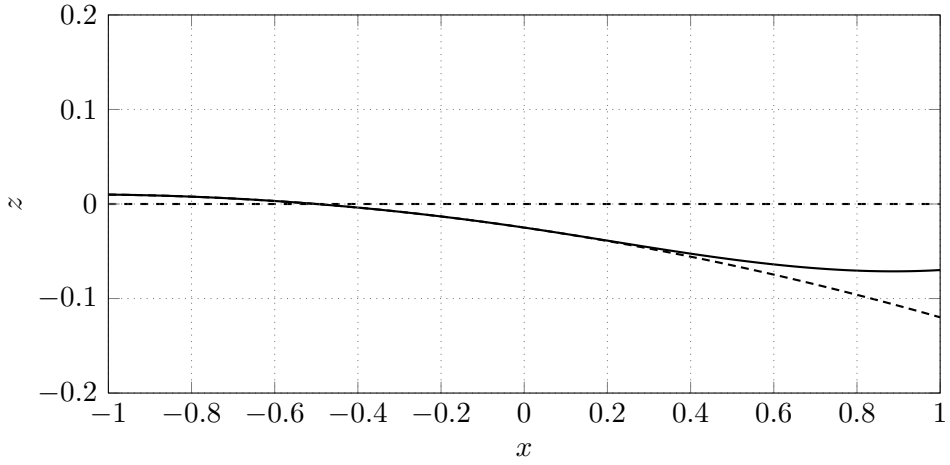


(B) Second step: linearly superposed cubic flap

FIGURE 1.3. Example of cubic polynomial deformation of the airfoil mean-line and superposition of a cubic flap

be easily accomplished by putting $\bar{B}_1 = 0$. Then the expanded polynomial parameters are simply:

$$A_1 = \frac{\bar{A}_1}{b^3} \tag{1.119}$$

$$B_1 = -3\frac{\bar{A}_1}{b^3}x_F \tag{1.120}$$

$$C_1 = 3\frac{\bar{A}_1}{b^3}x_F^2 \tag{1.121}$$

$$D_1 = -\frac{\bar{A}_1}{b^3}x_F^3 \tag{1.122}$$

As shown later, it will be easily imposable also the continuity of the second derivative, if wanted.

Hence the addition of each section of spline corresponds to the addition of a single degree of freedom.

Like it has been done so far, it is firstly necessary to compute the velocity as explained in eq. 1.86 and to apply the usual change of variables, then we can deal with the upwash coefficients

$$\begin{aligned} P_n = & -\frac{1}{\pi U e^{j\omega t}} \int_0^{\pi} v(\theta,t) \cos n\theta \, d\theta = \\ & = -\frac{jkA_1b^3}{\pi b} \int_0^{\theta_F} \cos^3\theta \cos n\theta \, d\theta + \\ & - \frac{jkB_1b^2 + 3A_1b^3}{\pi b} \int_0^{\theta_F} \cos^2\theta \cos n\theta \, d\theta + \\ & - \frac{jkC_1b + 2B_1b^2}{\pi b} \int_0^{\theta_F} \cos\theta \cos n\theta \, d\theta - \frac{jkD_1 + C_1b}{\pi b} \int_0^{\theta_F} \cos n\theta \, d\theta \end{aligned} \tag{1.123}$$

with $\theta_F = \arccos \tilde{x}_F$. The computation of the integrals is required (see Appendix A). The final solution for the upwash is

$$\begin{aligned} P_n = & -\frac{jkD + bC}{\pi b} \frac{\sin n\theta_F}{n} + \\ & - \frac{1}{2} \frac{jkbC + 2b^2B}{\pi b} \left( \frac{\sin(n+1)\theta_F}{n+1} + \frac{\sin(n-1)\theta_F}{n-1} \right) + \\ & - \frac{jkb^2B + 3b^3A}{\pi b} \left[ \frac{\sin n\theta_F}{2n} + \frac{1}{4} \left( \frac{\sin(n+2)\theta_F}{n+2} + \frac{\sin(n-2)\theta_F}{n-2} \right) \right] + \\ & - \frac{jkb^3A}{\pi b} \left[ \frac{3}{8} \left( \frac{\sin(n+1)\theta_F}{n+1} + \frac{\sin(n-1)\theta_F}{n-1} \right) + \right. \\ & \left. + \frac{1}{8} \left( \frac{\sin(n+3)\theta_F}{n+3} + \frac{\sin(n-3)\theta_F}{n-3} \right) \right] \end{aligned} \tag{1.124}$$

except for the following cases, in which some indeterminacies ought to be examined

$$\begin{aligned} P_0 = & -\frac{jkD + bC}{\pi b} \theta_F - \frac{jkbC + 2b^2B}{\pi b} \sin\theta_F + \\ & - \frac{jkb^2B + 3b^3A}{\pi b} \left( \frac{\theta_F}{2} + \frac{1}{4} \sin 2\theta_F \right) + \\ & - \frac{jkb^3A}{\pi b} \left( \frac{3}{4} \sin\theta_F + \frac{\sin 3\theta_F}{12} \right) \end{aligned} \tag{1.125}$$

$$
\begin{aligned}
P_1 = &- \frac{jkD + bC}{\pi b}\sin\theta_F - \frac{1}{2}\frac{jkbC + 2b^2B}{\pi b}\Big(\frac{\sin 2\theta_F}{2} + \theta_F\Big) + \\
&- \frac{jkb^2B + 3b^3A}{\pi b}\Big[\frac{\sin\theta_F}{2} + \frac{1}{4}\Big(\frac{\sin 3\theta_F}{3} + \sin\theta_F\Big)\Big] + \\
&- \frac{1}{8}\frac{jkb^3A}{\pi b}\Big(\frac{\sin 4\theta_F}{4} + 2\sin 2\theta_F + 3\theta_F\Big)
\end{aligned} \tag{1.126}
$$

$$
\begin{aligned}
P_2 = &- \frac{jkD + bC}{\pi b}\frac{\sin 2\theta_F}{2} - \frac{1}{2}\frac{jkbC + 2b^2B}{\pi b}\Big(\frac{\sin 3\theta_F}{3} + \sin\theta_F\Big) + \\
&- \frac{jkb^2B + 3b^3A}{\pi b}\Big[\frac{\sin 2\theta_F}{4} + \frac{1}{4}\Big(\frac{\sin 4\theta_F}{4} + \theta_F\Big)\Big] + \\
&- \frac{jkb^3A}{\pi b}\Big[\frac{3}{8}\Big(\frac{\sin 3\theta_F}{3} + \sin\theta_F\Big) + \frac{1}{8}\Big(\frac{\sin 5\theta_F}{5} + \sin\theta_F\Big)\Big]
\end{aligned} \tag{1.127}
$$

$$
\begin{aligned}
P_3 = &- \frac{jkD + bC}{\pi b}\frac{\sin 3\theta_F}{3} - \frac{1}{2}\frac{jkbC + 2b^2B}{\pi b}\Big(\frac{\sin 4\theta_F}{4} + \frac{\sin 2\theta_F}{2}\Big) + \\
&- \frac{jkb^2B + 3b^3A}{\pi b}\Big[\frac{\sin 3\theta_F}{6} + \frac{1}{4}\Big(\frac{\sin 5\theta_F}{5} + \sin\theta_F\Big)\Big] + \\
&- \frac{jkb^3A}{\pi b}\Big[\frac{3}{8}\Big(\frac{\sin 4\theta_F}{4} + \frac{\sin 2\theta_F}{2}\Big) + \\
&+ \frac{1}{8}\Big(\frac{\sin 6\theta_F}{6} + \theta_F\Big)\Big]
\end{aligned} \tag{1.128}
$$

Now we have all the necessary elements to compute the pressure distribution, the lift and the aerodynamic moment caused by this particular camberline shape, as explained in sections 1.1 and 1.1.1. What is still missing is an equation to compute the aerodynamic power associate with this motion.

$$
\begin{aligned}
W(t) = &\frac{1}{2}\rho U^2 b\int_0^{\pi}\Delta C_p(\theta,t)\dot{z}(\theta,t)\sin\theta\,d\theta = \\
= &\frac{1}{2}\rho U^2 bj\omega\int_0^{\theta_F}\Delta C_p(\theta,t)\mathcal{P}_1(\theta)\sin\theta\,d\theta\,e^{j\omega t} \\
= &\frac{1}{2}\rho U^2 bj\omega\int_0^{\theta_F}\Big(4a_0\tan\frac{\theta}{2} + 8\sum_{n=1}^{\infty}a_n\sin n\theta\Big)(A_1b^3\cos^3\theta + \\
&+ B_1b^2\cos^2\theta + C_1b\cos\theta + D_1)\sin\theta\,d\theta\,e^{j2\omega t}
\end{aligned} \tag{1.129}
$$

once the solution of the eight integrals is known (see Appendix A), the final expression of the aerodynamic power associated to the cubic flap movement

is

$$
\begin{aligned}
W(t) =& \frac{1}{2}\rho U^3 jk4a_0\Bigg\{D_1\Big(\theta_F - \sin\theta_F\Big) + C_1 b\bigg(-\frac{\theta_F}{2} + \sin\theta_F - \frac{\sin 2\theta_F}{4}\bigg) + \\
&+ B_1 b^2\bigg(\frac{\theta_F}{2} - \frac{3}{4}\sin\theta_F - \frac{\sin 3\theta_F}{12}\bigg) + \\
&+ A_1 b^3\bigg[\frac{1}{2}\bigg(\frac{\sin 3\theta_F}{6} + \frac{3}{2}\sin\theta_F\bigg) + \\
&- \frac{1}{4}\bigg(\frac{3\theta_F}{2} + \sin 2\theta_F + \frac{\sin 4\theta_F}{8}\bigg)\bigg]\Bigg\} e^{j2\omega t} + \\
&+ \frac{1}{2}\rho U^3 jk8 \sum_{n=1}^{\infty} a_n \Bigg\{D_1 \frac{1}{2}\bigg(\frac{\sin(n-1)\theta_F}{n-1} - \frac{\sin(n+1)\theta_F}{n+1}\bigg) + \\
&+ C_1 b \frac{1}{4}\bigg(\frac{\sin(n-2)\theta_F}{n-2} - \frac{\sin(n+2)\theta_F}{n+2}\bigg) + \\
&+ B_1 b^2\bigg[\frac{1}{8}\bigg(\frac{\sin(n-3)\theta_F}{n-3} - \frac{\sin(n+3)\theta_F}{n+3}\bigg) + \\
&+ \frac{1}{8}\bigg(\frac{\sin(n-1)\theta_F}{n-1} - \frac{\sin(n+1)\theta_F}{n+1}\bigg)\bigg] + \\
&+ A_1 b^3\bigg[\frac{1}{8}\bigg(\frac{\sin(n-2)\theta_F}{n-2} - \frac{\sin(n+2)\theta_F}{n+2}\bigg) + \\
&+ \frac{1}{16}\bigg(\frac{\sin(n-4)\theta_F}{n-4} - \frac{\sin(n+4)\theta_F}{n+4}\bigg)\bigg]\Bigg\}
\end{aligned}
\tag{1.130}
$$

It must be noticed that there are some undetermined terms in the summation that need to be treated with limit operations as previously done.

These results are also valid for multiple sequence of flaps, it is sufficient to replace $\theta_F$ with the one associated with the desired flap. In fact, exploiting linearity as already done with the trim tab, every upwash contribution can be computed separately and then superposed to the others in order to get the global solution.

### 1.3.3 Comparison with flapped airfoil

A comparison between the two representations of the morphing blade mean-line deformation, namely the model with flaps and the cubic spline can be made. One possible way to compare these two models is to choose the coefficients of the cubic polynomial so that the best fitting of the flapped airfoil shape can be achieved. The fitting can be obtained by solving a least squares problem.

To solve the fitting problem it is firstly necessary to write the expressions of the displacement of the airfoil points both with the flap and the cubic representations.

$$z_{\text{flaps}}(x,t) = \begin{cases} -(x-x_p)\alpha e^{j\omega t} & \text{if } x \le x_{F_0} \\ [-(x-x_p)\alpha - (x-x_{F_0})\beta_0]e^{j\omega t} & \text{if } x_{F_0} < x \le x_{F_1} \\ [-(x-x_p)\alpha - (x-x_{F_0})\beta_0 + & \\ \quad -(x-x_{F_1})\beta_1]e^{j\omega t} & \text{if } x > x_{F_1} \end{cases} \tag{1.131}$$

$$z_{\text{spline}}(x,t) = \begin{cases} \mathcal{P}_0(x)e^{j\omega t} & \text{if } x \le x_{F_0} \\ (\mathcal{P}_0(x) + \mathcal{P}_1(x))e^{j\omega t} & \text{if } x > x_{F_0} \end{cases} \tag{1.132}$$

Then a least squares best fitting can be obtained by minimizing the sum of the squares of the difference between the two different displacement, after imposing one shape, for example the one with flaps:

$$\begin{aligned} \text{Minimize} \qquad & J(\mathbf{p}) = \frac{1}{2}\sum_{j=1}^{m} r_j(\mathbf{p})^2 \\ \text{with} \qquad & r_j(\mathbf{p}) = \left| z_{\text{flaps}}(x_j, t, \bar{\mathbf{p}}) - z_{\text{spline}}(x_j, t, \mathbf{p}) \right| \end{aligned}$$

where $\bar{\mathbf{p}} = \begin{Bmatrix} \bar{\alpha} & \bar{\beta}_0 & \bar{\beta}_1 \end{Bmatrix}$ are the imposed angles and $\mathbf{p} = \begin{Bmatrix} A & B & C & A_1 & B_1 \end{Bmatrix}$ are the minimization variables.

Although the obtained shape is quite close to the starting one, there are some substantial differences, which imply that the pressure difference distributions and aerodynamic forces are expected to be quite different. First of all the first one is a regular shape, while the other presents discontinuities in the first derivative at the hinges which, as previously seen (1.2.6), cause the creation of singularities in the pressure distribution. This can obviously lead to some differences in the aerodynamic actions. Secondly, for some shapes with deflected flaps (Figure 1.4), close to the trailing edge the polynomial mean-line has a non-negligible difference in the slope (especially if the fitting is performed with a spline only regular up to the first derivative), and, of course, a different curvature, provoking other differences in the pressure distribution, which also affect the lift, the moment and the power.

The results obtained from the two different modelizations are nevertheless compared for some characteristic shapes, in order to see how the small shape differences affect the aerodynamic of the airfoil. It can be seen in Table 1.2 that for concordant small flap deflections, when the singularities effect is smaller, the results present very small differences, that increase with the

flaps deflection, as the singularities effect becomes more relevant. Instead for opposite deflections, when the aforementioned problems in the fitting arise, differences get more substantial,but the overall result are still comparable and have the same order of magnitude, as intuitively expected for qualitatively similar mean-line shapes.

| Percentage difference | $[10^\circ, 10^\circ, 10^\circ]$ | $[10^\circ, -10^\circ, 10^\circ]$ | $[10^\circ, 10^\circ, -10^\circ]$ |
|---|---|---|---|
| $\|L\|$ | 8.553908 | 7.105327 | 5.676060 |
| $\|M_{c/4}\|$ | 14.947215 | 10.634315 | 0.936460 |
| $\|W\|$ | 14.372477 | 7.524987 | 1.026945 |

TABLE 1.2. Percentage differences between flapped and spline representations of the chord, $N_P = 1000$, spline regular up to the second derivative, two-segment spline, $k = 0.5$

| Percentage difference | $[10^\circ, 10^\circ, 10^\circ]$ | $[10^\circ, -10^\circ, 10^\circ]$ | $[10^\circ, 10^\circ, -10^\circ]$ |
|---|---|---|---|
| $\|L\|$ | 0.766836 | 16.743230 | 10.752191 |
| $\|M_{c/4}\|$ | 1.385297 | 5.105471 | 7.771373 |
| $\|W\|$ | 1.560068 | 10.925071 | 8.788666 |

TABLE 1.3. Percentage differences between flapped and spline representations of the chord, $N_P = 1000$, spline regular up to the first derivative, two-segment spline, $k = 0.5$

### 1.3.4 Convergence

Since Küssner and Schwarz theory results are expressed in terms of an infinite series of upwash coefficients, it is necessary to decide where to truncate it when computing numerical values. The choice can be performed quite arbitrarily, depending of the level of accuracy needed and the computational costs one is willing to pay.

To estimate the convergence is no longer possible to perform a comparison with other theories analytical results, as did in section 1.2.7, hence another path has to be chosen.

For instance it is possible to gradually increase the number of upwash coefficients taken into account for fixed parameter values and compare the related aerodynamic power values. When the results differences tend to be small enough for a sufficient change in the number of coefficient, one can stop

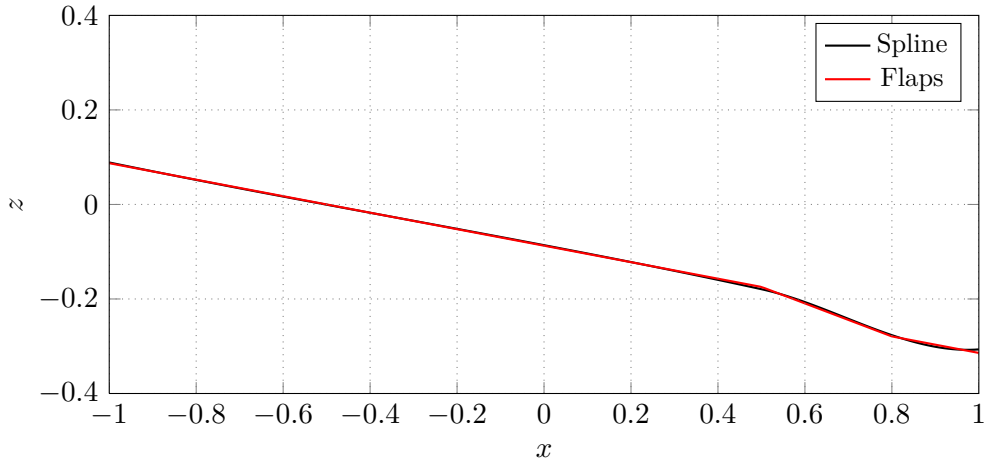


FIGURE 1.4. Least squares fitting between flapped airfoil and two pieces cubic spline camberline regular up to the first derivative

and consider the series to be converged. The test is only carried out on the aerodynamic power because the lift and the moment only depend on a small finite number of upwash coefficients, so they are not affected by truncation errors.

| $N_P$ difference | $[10^\circ, 10^\circ, 10^\circ]$ | $[10^\circ, -20^\circ, 20^\circ]$ | $[2^\circ, -5^\circ, -20^\circ]$ |
|---|---|---|---|
| $10 - 30$ | 0.000468 | 0.001856 | 0.019114 |
| $30 - 60$ | 0.000000 | 0.000001 | 0.000012 |
| $60 - 100$ | 0.000000 | 0.000000 | 0.000000 |

TABLE 1.4. Residuals between aerodynamic power truncated at a different number of upwash coefficients. The spline is a least squares fitting of a flapped airfoil with the indicated angle amplitudes

It can be seen from Table 1.4 that $N_P = 100$ is a suitable round number of upwash coefficients for a very good convergence, and is not too computationally expensive.

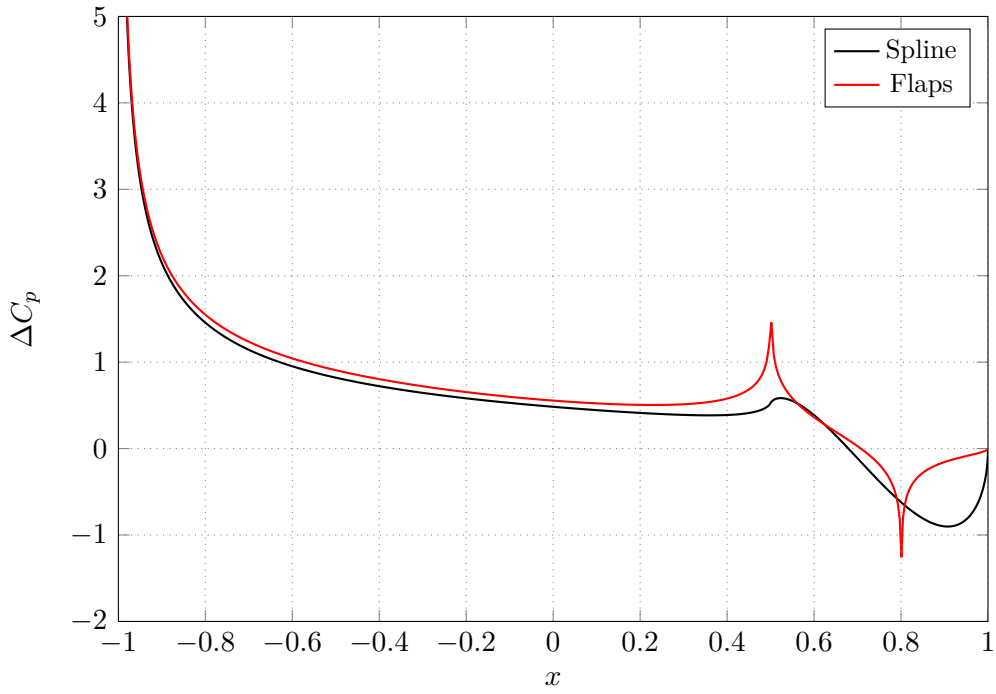


FIGURE 1.5. Least squares fitting between flapped airfoil and two pieces cubic spline camberline up to the first derivative, pressure difference, $N_P = 1000$

CHAPTER 2

# INERTIAL AND ELASTIC MODELS

The oscillating deformation of the airfoil needs to be actively induced. Hence some actuators are needed and they must be able to supply the required forces and power to impose the wanted movement. This power is mainly composed by three components, dictated by the physics of the problem: the aerodynamic power, which has been already discussed in Chapter 1, the elastic component, that arises when the airfoil mean-line is deformed, and lastly the inertial moment, needed to accelerate the airfoil mass. These two new components are discussed in this chapter.

## 2.1 Equation of motion

Since a bi-dimensional airfoil is a slender structural component, in which the thickness $t(x)$ is much smaller than the chord size, it is possible to consider it as a deformable mono-dimensional beam that bends to assume the wanted shape. The Euler-Bernoulli beam model can be used to describe the elastic behaviour of the airfoil. This model assumes that each beam section remains plane and orthogonal to the elastic line, coinciding with the mean-line for a symmetrical airfoil, during any movement.

Since the airfoil shape oscillates in time, its points are also subject to inertial forces that are opposed to the points acceleration.

It is possible to write the well known equation of motion of the beam in

a *weak form* by means of the *principle of virtual works* (PVW)

$$\int_{-b}^{b} \delta z''^T EJ(x) z'' \, dx = -\int_{-b}^{b} \delta z^T m(x) \ddot{z} \, dx + \int_{-b}^{b} \delta z^T F_{\text{aero}}(x) \, dx + \\ + \int_{-b}^{b} \delta z^T F_{\text{act}}(x) \, dx \tag{2.1}$$

where it has to be noticed that the contribution of rotational inertia of the beam section has been neglected. $F_{\text{aero}}(x)$ is the distributed aerodynamic chordwise load, namely the pressure difference distribution $\Delta P_a(x)$ and $F_{\text{act}}(x)$ are the distributed actuation forces, $EJ(x)$ is the bending stiffness and $m(x)$ the mass distribution.

### 2.1.1 Ritz-Galerkin method

The idea here is to utilize a so called *Ritz-Galerkin* approach, that is based on the approximation of the weak solution in the form:

$$z(x,t) = \sum_{i=1}^{N_n} N_i(x) u_i(t) = \Big[N(x)\Big] \, \mathbf{u}(t) \tag{2.2}$$

where $N_i(x)$ are imposed shape functions, that depends only on the position, and satisfy the essential boundary conditions, while $u_i$ are the unknown free coordinates, that are functions of the time. The separation of variables principle is hence used. $[N(x)]$ is a matrix of size $1 \times N_n$, with $N_n$ being the number of utilized shape functions. To allow the solution to converge by increasing the number of shape functions, these functions must belong to a complete basis. This means that they have to be a basis of the function space that is the space of the problem solutions.

Substituting the approximated expression of the displacement in the equilibrium equation

$$\delta \mathbf{u}^T \int_{-b}^{b} [N]''^T EJ(x) [N]'' dx \, \mathbf{u} = -\delta \mathbf{u}^T \int_{-b}^{b} [N]^T m(x) [N] dx \, \ddot{\mathbf{u}} + \\ + \delta \mathbf{u}^T \int_{-b}^{b} [N]^T \Delta P_a(x,t) \, dx + \delta \mathbf{u}^T \int_{-b}^{b} [N]^T F_{\text{act}}(x,t) \, dx \tag{2.3}$$

exploiting the arbitrariness of the virtual variation is possible to get to

$$\underbrace{\int_{-b}^{b} [N]''^T EJ(x) [N]'' dx}_{[K]} \, \mathbf{u} = -\underbrace{\int_{-b}^{b} [N]^T m(x) [N] dx}_{[M]} \, \ddot{\mathbf{u}} + \\ + \underbrace{\int_{-b}^{b} [N]^T \Delta P_a(x,t) \, dx}_{\mathbf{Q}_a} + \underbrace{\int_{-b}^{b} [N]^T F_{\text{act}}(x,t) \, dx}_{\mathbf{Q}_{\text{act}}} \tag{2.4}$$

that is

$$[M]\ddot{\mathbf{u}} + [K]\mathbf{u} = \mathbf{Q}_a(t) + \mathbf{Q}_{\text{act}}(t) \tag{2.5}$$

where $[M]$ is the *mass matrix*, $[K]$ the *stiffness matrix* and $\mathbf{Q}_a$ is the vector of the *generalized forces* associated to the aerodynamics, and $\mathbf{Q}_{\text{act}}$ are the generalized actuation forces.

Since only small harmonic oscillations are considered, it is now possible to move to the frequency domain, obtaining, with a little abuse of notation:

$$-\omega^2[M]\mathbf{u} + [K]\mathbf{u} = \mathbf{Q}_a(\omega) + \mathbf{Q}_{\text{act}}(\omega) \tag{2.6}$$

## 2.2 Hermitian finite elements

Having used a Ritz-Galerkin method to approximate the mean-line displacement, it is necessary to choose some shape functions $[N]$ and their relative degrees of freedom $\mathbf{u}$. One possible choice is to employ *finite elements*, especially hermitian finite elements.

The basic principle of finite elements method (FEM), is to divide the domain (here the beam) in a collection of subdomains, namely the finite elements. Then shape functions are defined to interpolate the displacement on each single element starting from the value of the displacement on every element nodes, that are the element degrees of freedom, whereas they are null on the other elements. This means that the support of the shape functions is compact, *i. e.* limited in space. A major advantage that results from this choice is the sparsity of the matrices.

To achieve a solution that possesses $C^1$ smoothness, it is possible to employ hermitian finite elements, which use hermitian shape functions on the elements:

$$\text{Node 1: } \begin{cases} N_1(\xi) = \frac{1}{4}(1-\xi)^2(2+\xi) \\ M_1(\xi) = \frac{h}{8}(1-\xi)^2(\xi+1) \end{cases} \tag{2.7}$$

$$\text{Node 2: } \begin{cases} N_2(\xi) = \frac{1}{4}(1+\xi)^2(2-\xi) \\ M_2(\xi) = \frac{h}{8}(1+\xi)^2(\xi-1) \end{cases} \tag{2.8}$$

where $h$ is the dimension of the element in the physical reference system $x$. These functions are defined only on the element, *i.e.* if $\xi \in [-1, 1]$, where $\xi$ is a transformed dimensionless coordinate of the reference element, otherwise they are null. As degrees of freedom are considered displacements

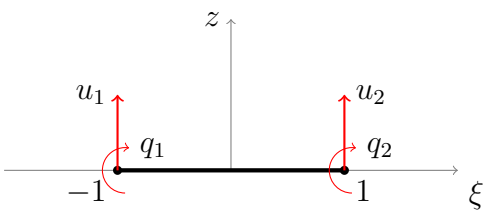


FIGURE 2.1. Reference mono-dimensional hermitian finite element

and rotations at the nodes, as shown in figure 2.1. Then the displacement of a point in the element can be interpolated in the following way

$$z(\xi) = \begin{bmatrix} N_1(\xi) & M_1(\xi) & N_2(\xi) & M_2(\xi) \end{bmatrix} \begin{Bmatrix} u_1 \\ q_1 \\ u_2 \\ q_2 \end{Bmatrix} = [N]_e \mathbf{u}_e \tag{2.9}$$

so that

$$z(-1) = u_1; \quad z(1) = u_2; \quad z'(-1) = q_1; \quad z'(1) = q_2 \tag{2.10}$$

## 2.3 Mass and stiffness matrices computation

### 2.3.1 Mass and bending stiffness distributions

In order to compute $[M]$ and $[K]$ it is firstly necessary to decide a model for the mass distribution $m(x)$ and the bending stiffness $EJ(x)$. A simple but useful model is to consider these quantities respectively proportional to the thickness of the airfoil $t(x)$ and its cube, namely

$$m(x) = C_m\, t(x) \tag{2.11}$$
$$EJ(x) = C_e\, t^3(x) \tag{2.12}$$

the reason for this choice and the meaning of the constants are discussed in this section. It is important to notice that the choice of using these models is only based on the need for simplicity, and not on a limitation on the computational technique adopted, since having used hermitian finite elements allows to take into account a more precise and local description of the airfoil structural characteristics.

A possible typical helicopter blade airfoil structure is shown in figure 2.2, based on the model proposed by Truong et al. in their work [24]. Although a morphing blade could be made in a quite different way, that will be considered

as a reference, remembering that the aim of this work is not to optimize a specific blade and to obtain accurate results but to review how an unsteady aerodynamic optimization can be carried out.

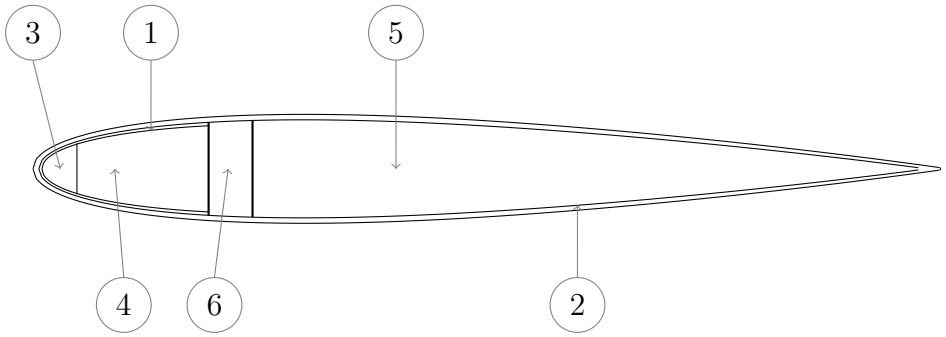


FIGURE 2.2. Example of helicopteristic NACA0012 airfoil

| Component | Material | Density $[kg/m^3]$ | $E\,[GPa]$ |
|---|---|---|---|
| 1 | carbon graphite LE wrap | 2.79 | 8.96 |
| 2a | E-1002 fiberglass 0°/90° | 1707 | 15.7 |
| 2b | E-1002 fiberglass ±45° | 1707 | 11.1 |
| 3 | tantalum leading edge slug | 13683 | 1.446 |
| 4 | foam | 95.5 | 0.031 |
| 5 | foam | 191 | 0.083 |
| 6 | Fiberite spar | 1826.9 | 15.42 |

TABLE 2.1. Material properties of helicopter blade

The goal is to extract a simplified mono-dimensional model for the mass and bending stiffness distributions that depends on the thickness, starting from a realistic bi-dimensional airfoil like the one in figure 2.2.

A dimensional analysis on the equation of motion (remembering that the problem is bi-dimensional, because the airfoil is flat) shows that the mass distribution $m(x)$ has the dimensions of $[kg/m^2]$. Then it can be seen as the product between the airfoil mean mass density and its thickness

$$m(x) = \rho_s t(x) \qquad \rightarrow \qquad C_m = \rho_s \tag{2.13}$$

Now it is necessary to extract an approximated value of the mean density from the airfoil constitutive model. It can be done with a weighted average of the single components densities (values are in table 2.1) using the relative

surfaces areas as weights.

$$\rho_s = \sum_i \rho_i \frac{A_i}{A_{tot}} \tag{2.14}$$

The surface covered by each component can be simply estimated from figure 2.2, remembering that precise results are not required in this instance. A possible value is $\rho_s \simeq 300\, kg/m^3$.

Regarding the bending stiffness $EJ(x)$, the dimensional analysis shows that its dimensions are $[Nm]$. Even though it is not true that the bending stiffness of a generic cross section of non-isotropic non-homogeneous material is equal to the product of the Young's modulus $E$ and the area moment of inertia $J$, it is possible to consider this fact as a useful simplification in order to obtain a raw approximation of $EJ(x)$ as a function of the thickness. The Young's modulus has units of pressure $[N/m^2]$ and the moment of inertia of $[m^3]$ (it is important to notice that $J$ usually has units of $[m^4]$, but it needs to be taken into account that the airfoil is flat, hence it has no span dimension).

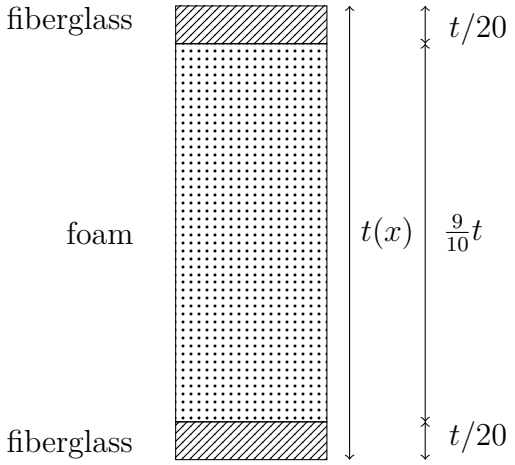


FIGURE 2.3. Airfoil simplified cross section

Concerning figure 2.3 and the aforementioned simplification, it is possible to state that

$$EJ(x) = EJ_f(x) + EJ_c(x) = E_f\, J_f(x) + E_c\, J_c(x) \tag{2.15}$$

Referring again to the figure of the cross section, it is possible to compute the second moments of area

$$J_f(x) = \frac{\left(t - t/10\right)^3}{12} = C_f\, t^3(x) \tag{2.16}$$

$$J_c(x) = \frac{t^3}{12} - \frac{\left(t - t/10\right)^3}{12} = C_c\, t^3(x) \tag{2.17}$$

Then, substituting in eq. 2.15, it can be obtained the final expression of $EJ(x)$

$$EJ(x) = E_f C_f\, t^3(x) + E_c C_c\, t^3(x) = E_s\, t^3(x) \tag{2.18}$$
$$\rightarrow \qquad C_e = E_s$$

### 2.3.2 Thickness

One of the typical helicopter blade airfoils is the NACA0012. In this work it will be used as reference because of its simplicity and its wide employment. It is a symmetrical airfoil and belongs to the NACA four digits series. Its maximum percentage thickness is $ss = 12$ (*i.e.* NACA00$ss$). The thickness distribution of this series of airfoil is standardized and is usually written as

$$t(x) = z_u(x) - z_l(x) = 2z_t(x) \tag{2.19}$$
$$z_u(x) = z_t(x) \tag{2.20}$$
$$z_l(x) = -z_t(x) \tag{2.21}$$

with

$$z_t(x) = \frac{ss}{20}\left(t_1\sqrt{x} + t_2 x + t_3 x^2 + t_4 x^3 + t_5 x^4\right) \tag{2.22}$$

where $x \in [0, 1]$ and the coefficients have the values in table 2.2.

| Coefficient | Value |
|---|---|
| $t_1$ | $+0.2969$ |
| $t_2$ | $-0.1260$ |
| $t_3$ | $-0.3516$ |
| $t_4$ | $+0.2843$ |
| $t_5$ | $-0.1015$ |

TABLE 2.2. NACA four digits airfoil thickness coefficients

Since the reference system used in this work has the origin in the middle of the airfoil, the leading edge at $x = -b$ and the trailing edge in $x = b$

($x \in [-b, b]$), the thickness expression must be rewritten in the new variables

$$z_t(x) = \frac{ss}{20} 2b \left( t_1 \sqrt{\frac{x+b}{2b}} + t_2 \frac{x+b}{2b} + t_3 \left( \frac{x+b}{2b} \right)^2 + \right.$$
$$\left. + t_4 \left( \frac{x+b}{2b} \right)^3 + t_5 \left( \frac{x+b}{2b} \right)^4 \right) \tag{2.23}$$

### 2.3.3 Integration

Now that all the necessary elements for the computation of the mass and stiffness matrix are known, it is possible to proceed with the computation of the matrices of each element $e$

$$[M]_e = \int_{-b}^{b} [N]_e^T m(x) [N]_e dx = \rho_s \int_{-b}^{b} t(x) [N]_e^T [N]_e dx =$$
$$= \rho_s \int_{-b}^{b} t(x) \begin{bmatrix} N_1^2 & N_1 M_1 & N_1 N_2 & N_1 M_2 \\ M_2 N_1 & M_1^2 & M_1 N_2 & M_1 M_2 \\ N_2 N_1 & N_2 M_1 & N_2^2 & N_2 M_2 \\ M_2 N_1 & M_2 M_1 & M_2 N_2 & M_2^2 \end{bmatrix}_e dx \tag{2.24}$$

$$[K]_e = \int_{-b}^{b} [N]_e''^T EJ(x) [N]_e'' dx = E \int_{-b}^{b} t^3(x) [N]_e''^T [N]_e'' dx =$$
$$= E \int_{-b}^{b} t^3(x) \begin{bmatrix} N_1''^2 & N_1'' M_1'' & N_1'' N_2'' & N_1'' M_2'' \\ M_2'' N_1'' & M_1''^2 & M_1'' N_2'' & M_1'' M_2'' \\ N_2'' N_1'' & N_2'' M_1'' & N_2''^2 & N_2'' M_2'' \\ M_2'' N_1'' & M_2'' M_1'' & M_2'' N_2'' & M_2''^2 \end{bmatrix}_e dx \tag{2.25}$$

The integrals are defined on the whole airfoil, but, since the finite elements shape functions are non-null only locally on each single element (compact support), their integration domain is only on each generic element $[x_1, x_2]$. Then the global matrices are built assembling each element matrix.

To compute these integrals it is possible to exploit *Gauss* numerical integration method (see [4]). It can be written in the following expression

$$\int_a^b f(x) w(x) \approx \sum_{i=0}^{g} \lambda_i f(x_i) \tag{2.26}$$

where $x_i$ are the Gauss internal nodes, $\lambda_i$ are Gauss weight coefficients and $w(x)$ is a weight function. If *Gauss-Legendre* formula is used the integration interval is $[a, b] = [-1, 1]$, the weight function is $w(x) = 1$ and the coefficients for different values of the order $g$ are displayed in tab. 2.3.

| $g$ | $x_i$ | $\lambda_i$ |
|---|---|---|
| 4 | $\pm 0.9061798459$ | 0.2369268851 |
| | $\pm 0.5384693101$ | 0.4786286705 |
| | 0 | 0.5688888888 |
| 5 | $\pm 0.9324695142$ | 0.1713244924 |
| | $\pm 0.6612093865$ | 0.3607615730 |
| | $\pm 0.2386191861$ | 0.4679139346 |

TABLE 2.3. Nodes and weights for Gauss-Legendre integration method

It is noticeable that the integration domain of the Gauss-Legendre formula is $[-1, 1]$, while the integrals have to be computed on a generic element that is defined in $[x_1, x_2]$. The passage to the generalized interval can be performed with an *isoparametric transformation* :

$$x = \frac{\tilde{x}(x_2 - x_1) + x_1 + x_2}{2} \tag{2.27}$$

hence the Jacobian of the transformation is

$$\frac{dx}{d\tilde{x}} = \frac{x_2 - x_1}{2} \tag{2.28}$$

and the integral becomes

$$\begin{aligned} \int_{x_1}^{x_2} f(x)\, dx &= \int_{-1}^{1} f(\tilde{x}) \frac{dx}{d\tilde{x}}\, d\tilde{x} = \\ &= \frac{x_2 - x_1}{2} \int_{-1}^{1} f\left( \frac{\tilde{x}(x_2 - x_1) + x_1 + x_2}{2} \right) d\tilde{x} \end{aligned} \tag{2.29}$$

At this point all the means to evaluate the element matrices are known. The following step is to use these small $4 \times 4$ matrices to assemble the global $2(N_e + 1) \times 2(N_e + 1)$ mass and stiffness matrices.

### 2.3.4 Change of variables

Once the finite elements mass and stiffness matrices are known, one last step is missing in order to advance to the computation of the power: an interface between structural coordinates $\mathbf{u}$ (FEM degrees of freedom) and aerodynamic coordinates $\mathbf{p}$ (cubic spline parameters) needs to be described.

To perform this operation it is necessary to write $2(N_e + 1) \times N_p$ transformation matrix that links the two sets of variables, where $N_e$ is the number of

elements and $N_p$ is the number of the spline parameters. This can be done by writing $2(N_e + 1)$ independent equations that equal the expressions of the displacements and rotations at each node in both the sets of variables, namely

$$\begin{Bmatrix} u_i \\ q_i \end{Bmatrix} = \begin{Bmatrix} z(x_i) \\ z'(x_i) \end{Bmatrix} = \\ = \begin{bmatrix} \left(\frac{x_i - x_p}{b}\right)^3 & \left(\frac{x_i - x_p}{b}\right)^2 & \left(\frac{x_i - x_p}{b}\right) & \left(\frac{x_i - x_F}{b}\right)^3 H(x_i - x_F) & \dots \\ \frac{3(x_i - x_p)^2}{b^3} & \frac{2(x_i - x_p)}{b^2} & \frac{1}{b} & \frac{3(x_i - x_F)^2}{b^3} H(x_i - x_F) & \dots \end{bmatrix} \begin{Bmatrix} \bar{A} \\ \bar{B} \\ \bar{C} \\ \bar{A}_1 \\ \bar{A}_2 \\ \dots \end{Bmatrix} \tag{2.30}$$

where $H(x - x_F)$ is the Heaviside step function. Repeating this for all the nodes and assembling in a single expression it is possible to write

$$\mathbf{u} = [U]\mathbf{p} \tag{2.31}$$

Finally the matrices can be transformed exploiting the PWV equation, obtaining

$$[M] = [U]^T [M]_{fem} [U] \tag{2.32}$$

$$[K] = [U]^T [K]_{fem} [U] \tag{2.33}$$

## 2.4 Power computation

The power involved in the airfoil motion can be computed integrating the product of the forces and what has been called perturbation speed in section 1.1.2, obtaining an expression similar to the PVW:

$$\int_{-b}^{b} \dot{z}''^T EJ(x) z'' \, dx = -\int_{-b}^{b} \dot{z}^T m(x) \ddot{z} \, dx + \int_{-b}^{b} \dot{z}^T F_{\text{aero}}(x) \, dx + \\ + \int_{-b}^{b} \dot{z}^T \Delta P_a(x) \, dx \tag{2.34}$$

Passing in the frequency domain, this means that the actuation power is

$$W_{\text{act}}(\omega) = j\omega \int_{-b}^{b} z''^T EJ(x) z'' \, dx - j\omega^3 \int_{-b}^{b} z^T m(x) z \, dx + \\ - j\omega \int_{-b}^{b} z^T \Delta P_a(x) \, dx \tag{2.35}$$

substituting the expression of the Ritz-Galerkin approximation and the models for $m(x)$ and $EJ(x)$ discussed in section 2.3.1, it is possible to obtain

$$\begin{aligned} W_{\text{act}}(\omega) =& j\omega E_s \mathbf{u}^T \int_{-b}^{b} [N]''^T t^3(x) [N]'' \, dx \, \mathbf{u} + \\ & - j\omega^3 \rho_s \mathbf{u}^T \int_{-b}^{b} [N]^T t(x) [N] \, dx \, \mathbf{u} + \\ & - j\omega \mathbf{u}^T \int_{-b}^{b} [N]^T \Delta P_a(x) \, dx \end{aligned} \tag{2.36}$$

that, with a little abuse of notation, is equal to

$$\begin{aligned} W_{\text{act}}(\omega) =& j\omega E_s \mathbf{u}^T [K]_{fem} \, \mathbf{u} - j\omega^3 \rho_s \mathbf{u}^T [M]_{fem} \, \mathbf{u} + \\ & - j\omega \mathbf{u}^T \int_{-b}^{b} [N]^T \Delta P_a(x) \, dx \end{aligned} \tag{2.37}$$

Then the change of variables discussed in section 2.3.4 is applied, so that every power contribution is expressed as a function of the cubic spline parameters (like the aerodynamic power computed in sections 1.3.1 and 1.3.2)

$$\begin{aligned} W_{\text{act}}(\omega) =& j\omega E_s \mathbf{p}^T [K] \, \mathbf{p} - j\omega^3 \rho_s \mathbf{p}^T [M] \, \mathbf{p} + \\ & - j\omega \mathbf{p}^T \int_{-b}^{b} [U]^T [N]^T \Delta P_a(x) \, dx \end{aligned} \tag{2.38}$$

Finally it is possible to non-dimensionalize the power like it usually done with the aerodynamic power, which means dividing it for $\frac{1}{2}\rho U^3(2b)$. This leads to

$$C_{W_{\text{act}}}(k) = jk \frac{E_s}{\rho U^2} \frac{\mathbf{p}^T [K] \, \mathbf{p}}{b^2} - jk^3 \frac{\rho_s}{\rho} \frac{\mathbf{p}^T [M] \, \mathbf{p}}{b^4} - C_{W_a} = \tag{2.39}$$

$$= C_{W_{el}}(k) - C_{W_{in}}(k) - C_{W_a}(k) \tag{2.40}$$

in this way it is possible to highlight two dimensionless parameters that scale respectively the elastic and the inertial forces with respect to the aerodynamics. These parameters are

$$\frac{E_s}{\rho U^2} \tag{2.41}$$

and

$$\frac{\rho_s}{\rho} \quad . \tag{2.42}$$

# CHAPTER 3
# OPTIMIZATION

The aim of this thesis is to optimize the aerodynamics of a morphing blade, or, in simple words, to obtain its "best" aerodynamic behaviour. But what does this mean? It means to find an optimal set of project parameters (or optimization variables) in order to minimize a so called *loss function* (or *fitness function*, *objective function*) which is the mathematical description of what has to be optimized.

## 3.1 What to Optimize

Before starting any optimization it is fundamental to decide which function (or functions) is to be minimized to achieve the goal, that is to give a precise definition of what is the desired "best". In other words a loss function has to be chosen. In our case it should be a function whose minimum corresponds to an optimal performance somehow related to the blade aerodynamics.

The main function of a lifting surface is to produce some lift indeed. Hence, also in this optimization problem, the airfoil should be able to generate a non-null lift, remembering that it is an oscillatory perturbation in respect to a reference condition, when using a linearized harmonic model such as Küssner and Schwarz theory. This can be achieved by imposing a constraint on the amplitude of the lift coefficient, forcing it to be equal to an arbitrarily assigned value. It will turn our problem into a constrained optimization, and the solution will be the set of parameters, among the ones that satisfy the constraint, which minimizes the objective functions.

This can be physically seen as the same effect as giving a certain cyclic

pitch control with respect to a steady solution, which causes an oscillation of the lift amplitude in time (at least in a linearized model), and hence in azimuthal position, in order to generate a flapping movement of the blade. The effect here is not obtained imposing a cyclic pitch angle but rather exploiting the morphing capabilities of the airfoil. Such an operation is connectible, for instance, to the one made when a rolling or pitching maneuver is wanted to start from a hovering condition.

A possible choice of objective function can be the quarter-chord aerodynamic moment. It is intuitive to understand that the minimum of the perturbation moment amplitude is achieved when the blade has no camber and zero incidence, *i.e.* when it is not oscillating and does not generate any lift. However this solution does not make much sense. The introduction of a constraint on the lift amplitude is able to avoid the optimization algorithm to converge to this trivial solution. If the moment is maintained as small as possible for each blade section, it will indeed turn into a reduction of the blade torsion, relieving its structural load and improving its fatigue behaviour. It may also decrease the moment at the pitch hinge (if one exists) involving a smaller actuation effort and reducing the vibrations transmitted to the hub.

It is important to notice that the moment value obtained with Küssner and Schwarz theory is a complex number (even if the time dependency complex exponential term), so its minimization has no direct meaning. It is possible instead to choose to minimize its amplitude (or modulus), neglecting on first instance what happens to its phase.

Another possible function to be optimized could be the aerodynamic power, as defined in Chapter 1, or rather its amplitude, for the same reason described for the moment. This power is a fraction of the total actuation power needed to morph the airfoil, the other major parts being the elastic and the inertial power. The global actuation power is computed in Chapter 2 and can substitute the aerodynamic power as an objective function. Also this function needs a constraint to avoid the solution of the optimization to be trivial.

Once identified these two functions, one may think to combine them in order to obtain a reduction of the moment without spending too much actuation power, or, from another point of view minimizing the aerodynamic power needed to produce a certain lift oscillation keeping at the same time the quarter-chord moment as small as possible. This leads to the development of a multi-objective constrained optimization, which will be described later in section 3.3.

Since the simple aerodynamic model taken into account is not capable of predicting flow separations and dynamic stalls it may be useful to impose some boundary constraint to the optimization variables, which describe the

shape and the incidence of the airfoil, in order to empirically avoid those phenomena.

## 3.2 Optimization Algorithms

There are several optimization techniques among which to choose, depending on the kind of optimization problem one has to deal with and the accuracy needed for the results.

Traditional optimization methods can be divided in *direct methods* and *gradient-based methods*. In the former only the objective function and constraint values are needed in order to advance in the optimum search, while gradient-based methods, as their name assert, use the first and second order derivatives (or some approximation of them) of the objective function and/or constraints to guide the process.

Gradient-based methods usually converge more quickly since they exploit the additional information on the derivatives, but they can be less efficient when applied on non-differentiable or discontinuous problems. Furthermore they have some features that can be an issue in some circumstances:

- The convergence to an optimal solution depends on the starting solution (initial guess)
- The majority of gradient-based algorithms are inclined to get stuck to suboptimal solutions: when non-linearities or complex interaction among variables cause the search space to have more than one optimal solution, of which most are local optima having worst objective function values
- An algorithm efficient in solving one kind of optimization problems may not be as efficient in solving a different problem, hence traditional optimization algorithms are designed to solve a specific problem

Evolutionary optimization methods (EO) utilize instead a population based approach to get to the optimal solution. Every solution belonging to the population participates in an iteration and evolves in a new population in each iteration. Evolutionary algorithms are relatively simpler to implement than gradient-based methods and do not require derivative information. Furthermore they are quite flexible and are applicable to a wide range of problems. Since evolutionary algorithms use more than one solution in an iteration, unlike most of classical optimization methods, they are facilitated in finding multiple optimal solution, reducing the possibility of getting

stuck in a local optima. This ability also makes these methods very suitable for multi-objective optimization.

This premise and the non-linearity of the optimization problem considered in this work might suggests at first glance that traditional methods are to be discarded in favour of evolutionary methods. Actually it will be shown that the careful employment of a performing gradient-based algorithm will allow some results to be obtained.

A conservative approach could be to first understand the behaviour of both classical and evolutionary methods when applied on a specific problem, and then adopting a hybrid procedure, exploiting the best of both techniques to get the desired results quality. For example one can firstly try out a fast gradient-based algorithm with different initial guesses in order to realize if multiple optima exist. If that is the case, a GA method can be used, which exhibits a more global search capability. Once a region nearby the global optimum is found, the result can be refined with a classical method started in that neighbourhood.

### 3.2.1 Sequential Quadratic Programming

One of the most effective gradient-based method for nonlinearly constrained optimization is Sequential Quadratic Programming (SQP). This method represents the state of the art in nonlinear programming methods and shows good performances over a large number of test problems.

The essential idea of SQP methods is to model the objective function at the current main iterate as a quadratic function, approximating the Hessian of the Lagrangian function using a quasi-Newton method, and to use a quadratic programming minimizer to solve this subproblem in order to find the new iterate.

A nonlinearly constrained problem can sometimes be solved in less iterations than an unconstrained problem with SQP because the algorithm can make aware decisions regarding the direction of the search thanks to limits on the feasible area given by constraints.

The implementation of a SQP algorithm consists mainly in three steps:

- Approximation of the Hessian matrix
- Quadratic programming solution
- Line Search or Thrust Region to decrease the merit function and find a new iterate point

#### Multi-Start Approach

As mentioned in section 3.2, some of the problems of gradient-based optimization methods are that the solution depends on the starting point and that they tend to get stuck in local optima, especially if one of these local solutions is the nearest stationarity point to a certain initial guess. This can be a relevant problem if the shape of the objective function and the approximative location of the solution are not known, that is the initial guess is chosen randomly.

A simple solution to this problem could be the so called *Multi-Start Approach*. It consists in performing several optimizations, starting each one from a different initial guess, randomly chosen in the space of allowed variables values.

Although this does not assure the reaching of a global solution, it increases the chance of doing it. Furthermore it helps to clarify if an optimal solution is actually a global optimum or if there exist other stationary solutions possessing a better fitness value and it can also give a hint about the complexity of the object function. Thus it is advisable to start any nonlinear global optimization with such a strategy, in order to get a knowledge about the loss function and its different local optima.

### 3.2.2 Genetic Algorithms

Genetic algorithms (GA), as the name suggests, are evolutionary optimization methods whose optimization procedure is inspired by the principles of natural selection and genetics. Their working principle is very different from most of the traditional optimization techniques. In fact they use stochastic operators, unlike deterministic operators used in classic methods. Because of this intrinsic uncertainty, one can not expect this global method to certainly converge to the global optimum within a finite time, rather it can get close to it or it can find a good global optimum.

An EO method begins with the random creation of a initial population, whose individuals have a different combination of design variables values (in GA these values represent the *genotype* of the individual) contained within specified lower and upper boundaries. Traditional Genetic algorithms represent parameters values in binary strings, to get a pseudo-chromosomal representation of the genotype. This is not always necessary and variables real value can be used directly.

After, the value of objective function of each member is evaluated in order to assign a fitness value to each solution. The fitness can be a value which is a function of the objective function value or it can be equal to the function

value itself. If the optimization problem is constrained, a penality is added to solutions that do not respect constraint (infeasible solutions) in order to worsen their fitness.

Having introduced the term genotype, also a *phenotype* of every population member ca be defined. It can be seen as the actual observed properties of the solution, such as the value assumed by the objective functions for a specific genotype.

Then genetic operators can be applied on the population. A selection operator selects above-average (better) solutions and puts them in an intermediate mating pool while discarding the worst. These operators are usually stochastic: this means that better individuals have a larger chance of being selected.

Once the mating pool is available, *cross-over* operator is applied to create new individuals for the new population: it randomly picks two solutions (parents) from the mating pool and creates one or more new solutions (children) by exchanging some portion of information between the parents. This operation will not find children solution which are better than their parents for sure, but, since parents are not just random individuals, but they have survived a selection, the chance to create above-average solutions is better than random.

Then a *mutation* function is applied: it makes small random changes in the individuals to create mutation children. It provides genetic diversity and broadens the search space of the algorithm, although it does not imply that mutation children to be better solutions.

The *elitism* combines the old population and the newly created individuals and chooses to keep better solution from this combined population. Such operation makes sure that the algorithm has a monotonically non-decreasing performance.

At this point a new (and hopefully better) population is available and the process is to be iteratively repeated, emphasizing better population members, until a termination criterion is satisfied.

## 3.3 Multi-Objective Optimization

As mentioned in section 3.1, it would be interesting to take into account more than one objective during the optimization, for example the quarter-chord moment and the power. This would lead to a multi-objective optimization problem, in which multiple objective functions are to be optimized simultaneously.

This means that, in multi-objective optimization, the objective functions

constitute a multi dimensional space, or *objective space* (*i.e.* the phenotypic space in GA), in addition to the usual decision variable space, that is the genotypic space.

Since, generally speaking, the various objective functions do not share the same stationary solutions, the optimum can not be defined like for the single-objective optimization any more. A more general definition needs to be introduced. The term *domination* is generally used for this purpose. The domination can be defined in a simple way as follows (taken from [6]):

**Definition 1** *A solution* $\mathbf{x}^{(i)}$ *is said to dominate the other solution* $\mathbf{x}^{(j)}$*, if both the following conditions are true:*

1. *The solution* $\mathbf{x}^{(i)}$ *is no worse than* $\mathbf{x}^{(j)}$ *in all objectives. Thus, the solutions are compared based on their objective function values (or location of the corresponding points (*$\mathbf{z}^{(i)}$ *and* $\mathbf{z}^{(j)}$*) on the objective space)*

2. *The solution* $\mathbf{x}^{(i)}$ *is strictly better than* $\mathbf{x}^{(j)}$ *in at least one objective.*

All points that are not dominated by any other member of the population are called *non-dominated* points. These points constitute a front when viewed in the objective space, therefore they are said to represent a non-domination front, the *Pareto-optimal front* (or simply Pareto front) and each non-dominated decision variable vector is called Pareto-optimal solution.

Between non-dominated solutions there is a trade-off property: a gain in an objective function happens only if there is a sacrifice in at least another objective.

These ideas clarify the aim of multi-objective optimizations:

- Find a set of solutions which belong to the Pareto front
- Find a set of solutions whose phenotype is wide enough to represent in good part the range of the Pareto-optimal front.

Thus, if a user needs only one optimal solution, can apply qualitative and experience-driven consideration to a wide range of Pareto-optimal solutions in order to decide which optimal solution suits best the project requirements.

In constrained multi-objective optimization a Pareto-optimal point also needs to satisfy every constraint and bound, in other words it has to be a feasible solution. The domination principle has to be revised in order to handle constraint violation:

**Definition 2** *A solution* $\mathbf{x}^{(i)}$ *is said to 'constrained-dominate' the other solution* $\mathbf{x}^{(j)}$*, if any of the following conditions are true:*

1. *solution* $\mathbf{x}^{(i)}$ *is feasible and solution* $\mathbf{x}^{(j)}$ *is infeasible*
2. *solutions* $\mathbf{x}^{(i)}$ *and* $\mathbf{x}^{(j)}$ *are both infeasible, but solution* $\mathbf{x}^{(i)}$ *has a smaller constraint violation*
3. *solutions* $\mathbf{x}^{(i)}$ *and* $\mathbf{x}^{(j)}$ *are both feasible, and solution* $\mathbf{x}^{(i)}$ *dominates* $\mathbf{x}^{(j)}$ *in the usual sense (Definition 1)*

A traditional practice is to convert multiple objectives into one single objective function, usually made up of a weighted sum of the various objectives, and treat the problem as a single-objective optimization.

$$\text{Multiple objectives} \quad \begin{cases} \text{First objective} & J_1 = f_1(\mathbf{x}) \\ \text{Second objective} & J_2 = f_2(\mathbf{x}) \end{cases} \tag{3.1}$$

$$\text{Single objective} \quad J = f_1(\mathbf{x}) + \gamma f_2(\mathbf{x}) \tag{3.2}$$

This is useful if one wants to solve the multi-objective problem with a classical optimization method, such as a gradient-based one. By varying the weights and solving the single-objective problem, different Pareto-optimal solutions can be found in order to reconstruct the actual non-dominated front. This technique is very simple but it is strongly dependent on the chosen parametrization, and it is not easy to find a good weight in order to represent a good range of the Pareto front.

Furthermore, since the various simulations are performed independently, no information can be used to help the solver in finding the optimal solution and to speed up the process.

With genetic algorithms this approach is not necessary, because their features allow the evaluation of each object function separately, then the fitness of each individual is assigned based on its dominance.

### 3.3.1 NSGA-II algorithm

Elitist Non-dominated Sorting Genetic Algorithm (or NSGA-II) is a widely used evolutionary multi-objective optimization algorithm whose goal is to find multiple Pareto-optimal solutions. A slight variation of NSGA-II is the multi-objective genetic algorithm implemented in *Matlab* and is the one used in this work. As described in [6] and [7], it possesses the following features:

- it uses an elitist principle
- it uses an explicit diversity preserving mechanism
- it emphasizes non-dominated solutions

The functioning of the algorithm is the following: at each generation the offspring population is created with the usual genetic operators starting from the parent population. After the two populations are combined together in order to obtain an intermediate population with twice the size. This population individuals are classified in non-domination classes: the first is the non-dominated front, and continues with points from the second non-dominated front, namely the points which are non-dominated by other individuals if points from the first Pareto front are not considered, and so on. Then a normal size population needs to be obtained to proceed in the iterations, so individuals from the intermediated population are accommodated in the new population starting from the one belonging to the first non-domination class, and so on. When only the last slots of the new population are available, it is possible that the individuals of the currently considered front are more than the remaining slots. Hence are selected the points which will ensure major diversity in the new generation. In order to measure the diversity of the individuals their *crowding distance* needs to be computed. The crowding distance of a point is a measure of the space (in the objective space or in the variables space) around it which is not occupied by other solutions in the population.

## 3.4 Analytical Optimization Example

Let us start with the optimization of the quarter-chord moment of an airfoil with a single flap, subject to a "trim" constraint on the lift coefficient, as discussed in 3.1. This simple example of optimization can be solved analytically and be used as a comparison to verify the exact convergence of other more complex algorithms.

Firstly a loss function is needed. Since the moment is to be minimized, it can be the Küssner and Schwarz formulation of the moment itself as a function of the incidence angle $\alpha$ and the flap relative angle $\beta$, neglecting the time complex exponential (obtained with eq. 1.21).

$$C_M(\alpha, \beta) = \frac{M_{c/4}(\alpha, \beta)}{\frac{1}{2}\rho U^2 (2b)^2} \tag{3.3}$$

Since the employed aerodynamic model is linear, it can be written as

$$C_M(\alpha, \beta) = C_{M_\alpha}\,\alpha + C_{M_\beta}\,\beta = \begin{bmatrix} C_{M_\alpha} & C_{M_\beta} \end{bmatrix} \begin{Bmatrix} \alpha \\ \beta \end{Bmatrix} \tag{3.4}$$

As said before, this is a complex quantity, so it can not be minimized as it is, but we should take as loss function $J$ only its modulus, or rather the

half of its square

$$J = \frac{1}{2}|C_M|^2 = \frac{1}{2}C_M^H C_M = \frac{1}{2}\begin{Bmatrix}\alpha\\ \beta\end{Bmatrix}^T \begin{bmatrix}{C_{M_\alpha}}^*\\ {C_{M_\beta}}^*\end{bmatrix}\begin{bmatrix}C_{M_\alpha} & C_{M_\beta}\end{bmatrix}\begin{Bmatrix}\alpha\\ \beta\end{Bmatrix} =$$
$$= \frac{1}{2}\begin{Bmatrix}\alpha\\ \beta\end{Bmatrix}^T \Big[CM\Big]\begin{Bmatrix}\alpha\\ \beta\end{Bmatrix} \tag{3.5}$$

Then the constraint function must be written. As said before, we want to impose the value of the modulus of lift coefficient, obtained with Küssner and Schwarz theory like the moment (eq. 1.14), that is

$$|C_L|(\alpha,\beta) = \bar{C}_L \tag{3.6}$$

As will be shown later, it is more convenient to impose the square of the lift coefficient absolute value

$$|C_L|^2(\alpha,\beta) = \bar{C}_L^2 \tag{3.7}$$

Since also the lift coefficient is linear, this expression can be written as

$$\begin{Bmatrix}\alpha\\ \beta\end{Bmatrix}^T \begin{bmatrix}{C_{L_\alpha}}^*\\ {C_{L_\beta}}^*\end{bmatrix}\begin{bmatrix}C_{L_\alpha} & C_{L_\beta}\end{bmatrix}\begin{Bmatrix}\alpha\\ \beta\end{Bmatrix} = \bar{C}_L^2 \tag{3.8}$$

or better

$$\begin{Bmatrix}\alpha\\ \beta\end{Bmatrix}^T \Big[CL\Big]\begin{Bmatrix}\alpha\\ \beta\end{Bmatrix} = \bar{C}_L^2 \tag{3.9}$$

with

$$\Big[CM\Big] = \begin{bmatrix}{C_{M_\alpha}}^* C_{M_\alpha} & {C_{M_\alpha}}^* C_{M_\beta}\\ {C_{M_\beta}}^* C_{M_\alpha} & {C_{M_\beta}}^* C_{M_\beta}\end{bmatrix} \tag{3.10}$$

$$\Big[CL\Big] = \begin{bmatrix}{C_{L_\alpha}}^* C_{L_\alpha} & {C_{L_\alpha}}^* C_{L_\beta}\\ {C_{L_\beta}}^* C_{L_\alpha} & {C_{L_\beta}}^* C_{L_\beta}\end{bmatrix} \tag{3.11}$$

To impose the equality constraint the *Lagrange multipliers* method can be exploited, obtaining

$$J = \frac{1}{2}\Big(|C_M|^2 + \lambda(|C_L|^2 - \bar{C}_L^2)\Big) \tag{3.12}$$

Since the moment and the lift are linear functions of the optimization variables, both the loss function and the constraint are quadratic functions, hence also the Lagrangian is quadratic.

The stationarity condition of the objective function at the minimum corresponds to the nullification of its first variation

$$\delta J = \frac{1}{2}\delta|C_M|^2 + \frac{1}{2}\delta\lambda(|C_L|^2 - \bar{C}_L^2)\Big) + \frac{1}{2}\lambda\delta|C_L|^2 = 0 \tag{3.13}$$

It is important to notice that

$$\begin{aligned}
&\delta|C_M|^2 = \delta(C_M^H C_M) = \delta C_M^H C_M + C_M^H \delta C_M = \\
&= \delta \begin{Bmatrix}\alpha\\ \beta\end{Bmatrix}^T \begin{bmatrix}{C_{M_\alpha}}^*\\ {C_{M_\beta}}^*\end{bmatrix} \begin{bmatrix}C_{M_\alpha} & C_{M_\beta}\end{bmatrix} \begin{Bmatrix}\alpha\\ \beta\end{Bmatrix} + \\
&+ \begin{Bmatrix}\alpha\\ \beta\end{Bmatrix}^T \begin{bmatrix}{C_{M_\alpha}}^*\\ {C_{M_\beta}}^*\end{bmatrix} \begin{bmatrix}C_{M_\alpha} & C_{M_\beta}\end{bmatrix} \delta \begin{Bmatrix}\alpha\\ \beta\end{Bmatrix} = \\
&= \delta \begin{Bmatrix}\alpha\\ \beta\end{Bmatrix}^T \Big[CM\Big] \begin{Bmatrix}\alpha\\ \beta\end{Bmatrix} + \delta \begin{Bmatrix}\alpha\\ \beta\end{Bmatrix}^T \Big[CM\Big]^T \begin{Bmatrix}\alpha\\ \beta\end{Bmatrix} = \\
&= \delta \begin{Bmatrix}\alpha\\ \beta\end{Bmatrix}^T \Big(\Big[CM\Big] + \Big[CM\Big]^T\Big) \begin{Bmatrix}\alpha\\ \beta\end{Bmatrix} = \\
&= 2\delta \begin{Bmatrix}\alpha\\ \beta\end{Bmatrix}^T \Big[MM\Big] \begin{Bmatrix}\alpha\\ \beta\end{Bmatrix}
\end{aligned} \tag{3.14}$$

Similarly for the lift coefficient we obtain

$$\begin{aligned}
\delta|C_L|^2 &= 2\delta \begin{Bmatrix}\alpha\\ \beta\end{Bmatrix}^T \Big(\Big[CL\Big] + \Big[CL\Big]^T\Big) \begin{Bmatrix}\alpha\\ \beta\end{Bmatrix} = \\
&= 2\delta \begin{Bmatrix}\alpha\\ \beta\end{Bmatrix}^T \Big[ML\Big] \begin{Bmatrix}\alpha\\ \beta\end{Bmatrix}
\end{aligned} \tag{3.15}$$

where

$$\begin{aligned}
\Big[MM\Big] &= \frac{1}{2}\Big(\Big[CM\Big] + \Big[CM\Big]^T\Big) = \\
&= \begin{bmatrix} {C_{M_\alpha}}^* C_{M_\alpha} & \frac{1}{2}({C_{M_\alpha}}^* C_{M_\beta} + C_{M_\alpha} {C_{M_\beta}}^*) \\ \frac{1}{2}({C_{M_\alpha}}^* C_{M_\beta} + C_{M_\alpha} {C_{M_\beta}}^*) & {C_{M_\beta}}^* C_{M_\beta} \end{bmatrix}
\end{aligned} \tag{3.16}$$

$$\begin{aligned}
\Big[ML\Big] &= \frac{1}{2}\Big(\Big[CL\Big] + \Big[CL\Big]^T\Big) = \\
&= \begin{bmatrix} {C_{L_\alpha}}^* C_{L_\alpha} & \frac{1}{2}({C_{L_\alpha}}^* C_{L_\beta} + C_{L_\alpha} {C_{L_\beta}}^*) \\ \frac{1}{2}({C_{L_\alpha}}^* C_{L_\beta} + C_{L_\alpha} {C_{L_\beta}}^*) & {C_{L_\beta}}^* C_{L_\beta} \end{bmatrix}
\end{aligned} \tag{3.17}$$

Substituting in the variation of the loss function

$$\delta J = \delta \begin{Bmatrix} \alpha \\ \beta \end{Bmatrix}^T \Big[MM\Big] \begin{Bmatrix} \alpha \\ \beta \end{Bmatrix} + \lambda\delta \begin{Bmatrix} \alpha \\ \beta \end{Bmatrix}^T \Big[ML\Big] \begin{Bmatrix} \alpha \\ \beta \end{Bmatrix} + \frac{1}{2}\delta\lambda(|c_L|^2 - \bar{c}_L^2)\Big) \quad (3.18)$$

Exploiting the arbitrariness and the independence of the variables variations, the following system is obtained

$$\begin{cases} \Big(\Big[MM\Big] + \lambda\Big[ML\Big]\Big) \begin{Bmatrix} \alpha \\ \beta \end{Bmatrix} = 0 \\ |C_L|^2 - \bar{C}_L^2 = 0 \end{cases} \quad (3.19)$$

It can be noticed that the system's first equation is an eigenvalue problem, where the Lagrange multiplier $\lambda$ is the eigenvalue and the eigenvector components are the optimization parameters. Eigenvectors are defined up to a multiplicative constant, and this can be exploited to solve the system: first the eigenvalue problem is to be solved, obtaining eigenvalues and eigenvectors, then the latter can be substituted in the second equation and a multiplicative constant is computed to satisfy the constraint.

The eigenvalue represents the shape while the constant the amplitude of the movement of the airfoil.

1. solve the eigenvalue problem, obtaining $\lambda_i$ eigenvalues and the associated $\gamma_i \mathbf{x}_i$, where $\gamma_i$ is the multiplicative arbitrary constant. The solution can be found analytically for small problems, but in general it is better to employ a numerical method able to compute the whole eigenvector spectrum.

2. substitute the eigenvector in the constraint equation

$$\gamma_i^2 \mathbf{x}_i^T \Big[CL\Big] \mathbf{x}_i - \bar{C}_L^2 = 0 \quad (3.20)$$

3. solve the former quadratic equation in order to obtain the amplitude of the eigenvector that satisfy the constraint

$$\gamma_{i_{1,2}} = \pm \sqrt{\frac{\bar{C}_L^2}{\mathbf{x}_i^T \Big[CL\Big] \mathbf{x}_i}} \quad (3.21)$$

4. repeat for each eigenvector

| Eigenvector | Optimum, $\bar{C}_L = 0.05$ [°] | Optimum, $\bar{C}_L = 1$ [°] |
|---|---|---|
| $\mathbf{x}_1$ | $\pm\begin{Bmatrix}0.5191 & 0.2323\end{Bmatrix}^T$ | $\pm\begin{Bmatrix}10.3818 & 4.6469\end{Bmatrix}^T$ |
| $\mathbf{x}_2$ | $\pm\begin{Bmatrix}1.1288 & -2.4034\end{Bmatrix}^T$ | $\pm\begin{Bmatrix}22.5760 & -48.0683\end{Bmatrix}^T$ |

TABLE 3.1. Analytical optimal solutions for $\tilde{x}_p = -0.5$, $\tilde{x}_f = 0.5$, $k = 0.5$

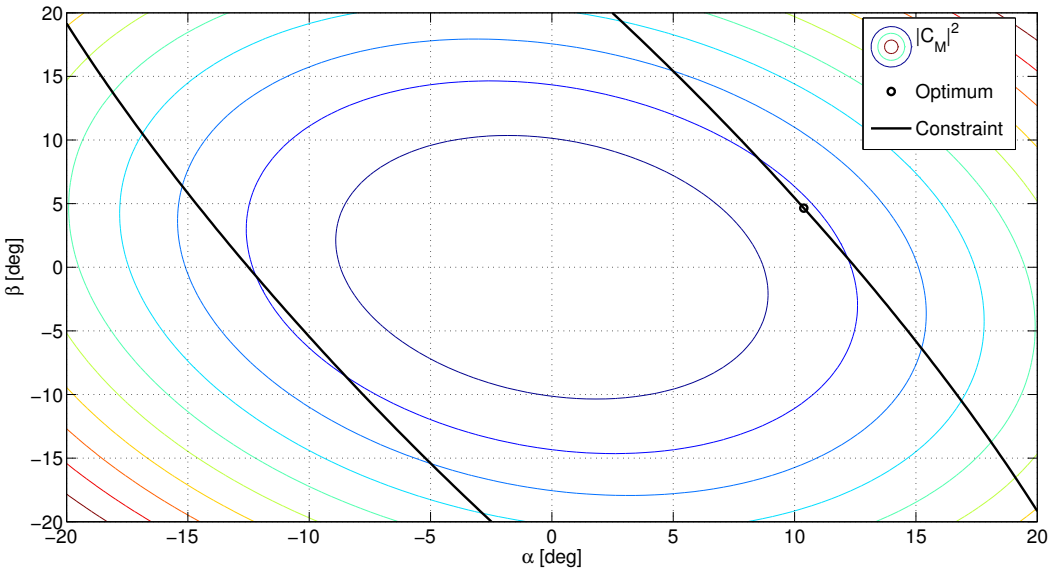


FIGURE 3.1. Contour plot of the object function, with a representation of the constraint and the optimal solution, for $\bar{C}_L = 1$, $k = 0.5$

It can be noticed that because of the $\pm$ there are two symmetric solution to the optimum problem. In fact this corresponds to a change of $\pi$ in the phase of the oscillation, which is not taken into account in our objective, hence both solutions are equally admissible. Some test results are reported in tab. 3.1 It has to be notice that only one of the eigenvectors represent an actual optimal solution, the other being a singularity point in the constraint.

This approach can be used also for bigger problems, where the airfoil chord is divided $n_t$ flaps. The procedure is the same, but the computational cost will obviously increase, as well as the number of solutions, some of which present angles that may probably lead to separation, as their values are too big. To avoid this, it is useful to introduce some bounds constraint to the optimization variables. This operation, which introduces further nonlinearities, is quite difficult to be carried out analytically, but is practicable in a

numerical optimization approach (see section 3.5).

One may now think about using this analytical approach to solve also the optimization of the aerodynamic power. First we need to write the modulus of the power coefficient, starting as usual from Küssner and Schwarz theory (1.72) Let us start by noticing that, from a dimensional point of view

$$C_W = \frac{W}{\frac{1}{2}\rho U^3 2b} = \frac{Mj\omega\alpha}{\frac{1}{2}\rho U^3 2b} = \frac{M}{\frac{1}{2}\rho U^2 (2b)^2}\frac{j\omega\alpha 2b}{U} = 2jkC_M\alpha \tag{3.22}$$

Hence, for a flapped airfoil, since the moment is a linear function

$$C_W = 2jk\begin{bmatrix} C_M & C_{M_F}\end{bmatrix}\begin{Bmatrix}\alpha\\ \beta\end{Bmatrix} = 2jk\begin{Bmatrix}\alpha\\ \beta\end{Bmatrix}^T\begin{bmatrix} C_{M_\alpha} & C_{M_{F_\alpha}}\\ C_{M_\beta} & C_{M_{F_\beta}}\end{bmatrix}\begin{Bmatrix}\alpha\\ \beta\end{Bmatrix} \tag{3.23}$$

This expression shows that the power is a quadratic function of the optimization variables, so the square of its modulus is a quartic. So it is possible to realize that the previous steps will not lead to an eigenvalue problem, but to a nonlinear equation, whose solution is not easily reachable analytically. Hence this problem will be treated numerically in section 3.6

## 3.5 Quarter-chord moment numerical optimization

The quarter-chord aerodynamic moment optimization problem can be solved by employing one of the optimization techniques described earlier in section 3.2, even though an analytical solution is available. This is useful when some boundaries to the optimization variables are introduced. It is also a good test-problem to verify the convergence of numerical algorithms.

As previously said, the problem can be stated as:

$$\begin{aligned} \text{minimize} \quad & J(\mathbf{x}) = |C_M(\mathbf{x})|^2 && (3.24)\\ \text{subject to} \quad & f(\mathbf{x}) = |C_L(\mathbf{x})|^2 - \bar{C}_L^2 = 0, && (3.25)\\ & x_i \in [\text{LB}, \text{UB}] \text{ for } i = 1, \ldots, n_{\text{var}} && (3.26)\end{aligned}$$

where $\mathbf{x}$ is the vector of the optimization variables, which could be the angle of incidence and flaps deflections or the cubic spline parameters. LB and UB are the lower and the upper boundaries assigned to the optimization variables. The problem can be solved for two variables (incidence and flap deflection) in order to verify the convergence of the numerical methods, comparing the results to the ones obtained analytically in section 3.4.

The employment of a genetic algorithm may sound redundant for such a simple problem, but it is a good starting point to adjust the various options and parameters in order to get a good functioning. However the main employment of GA in this work is for multi-objective optimization, hence it is more advisable to tune the method for this purpose.

SQP algorithm is expected to be far faster than GA for a simple quadratic function like the aerodynamic moment, also because it can efficiently exploit the constraint to get to the optimum.

## 3.6 Aerodynamic work numerical optimization

Instead of the aerodynamic power, that is null in the steady case since $k = 0$, it is possible to try to optimize the aerodynamic work, that has substantially the same meaning. This optimization does not provide a considerable added value, but is interesting because can be used to verify the fact that at the steady case the configuration with flap and tab with deflection $\beta = -\beta_1$, with $\alpha$ being imposed, is able to produce a lift variation with the minimum work cost.

The problem can be stated as:

$$\begin{aligned} \text{minimize} \quad & J(\mathbf{x}) = |C_w(\mathbf{x})|^2 && (3.27)\\ \text{subject to} \quad & f(\mathbf{x}) = |C_L(\mathbf{x})|^2 - \bar{C}_L^2 = 0, && (3.28)\\ & x_i \in [\text{LB}, \text{UB}] \text{ for } i = 1, \ldots, n_{\text{var}} && (3.29) \end{aligned}$$

A solution can be easily computed with SQP algorithm, and is shown in figure 3.2. It can be seen that the numerical solutions conforms what was expected, being $\beta = -\beta_1$ at $k = 0$. Increasing the reduced frequency the two angles become more and more different because of unsteadiness effects.

## 3.7 Aerodynamic moment and power numerical optimization

As introduced in section 3.1, it is interesting to perform a multi-objective optimization, minimizing simultaneously both the aerodynamic quarter-chord moment and the aerodynamic power, to obtain a Pareto front containing a

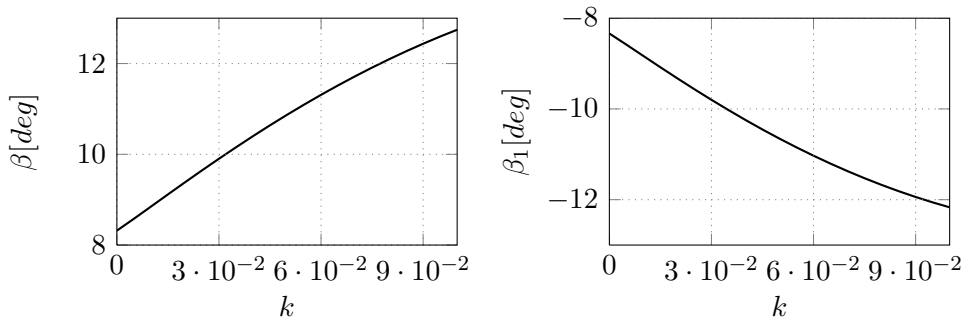


(A) Flap deflection (B) Tab deflection

FIGURE 3.2. Aerodynamic work optimization with a fixed incidence

sufficient number of trade-off non-dominated solutions.

$$\begin{aligned} &\text{minimize} && |C_M(\mathbf{x})|^2 \text{ and } |C_W(\mathbf{x})|^2 && (3.30)\\ &\text{subject to} && f(\mathbf{x}) = |C_L(\mathbf{x})|^2 - \bar{C}_L^2 = 0, && (3.31)\\ & && x_i \in [\text{LB}, \text{UB}] \text{ for } i = 1, \ldots, n_{\text{var}} && (3.32) \end{aligned}$$

Starting from what have been explained in section 3.3, there are two possible ways of doing this: scalarizing the multiple objective and optimizing a single-objective function (eq. 3.34) or applying a genetic algorithm directly on the multi-objective (eq. 3.33) problem.

$$\begin{aligned} &\text{Multiple objectives} && \begin{cases} \text{First objective} & J_1 = |C_M(\mathbf{x})|^2 \\ \text{Second objective} & J_2 = |C_W(\mathbf{x})|^2 \end{cases} && (3.33)\\ &\text{Scalarized objective} && J = AJ_1(\mathbf{x}) + \gamma B J_2(\mathbf{x}) && (3.34) \end{aligned}$$

The coefficients $A$ and $B = 1 - A$, with $A, B \in [0, 1]$, have been introduced to try and sweep the whole Pareto front, while $\gamma$ plays the role of a weight parameter used to equalize the objective functions order of magnitude. Both approaches are supposed to work, but results are not expected to be the same. Firstly because the scalarized-approach Pareto front points will strongly depend on the value of $\gamma$ and the variation pace of $A$, in other words will depend on the parametrization, while the genetic-approach front points will be obtained randomly on the basis of the random population generation and the also random application of genetic operators. Secondly, the different algorithms have different strength-points, so GA is expected to produce a more global front, whereas Multi-Start SQP approach will respect the constraint more precisely, but not all the initial guesses are expected to converge to the non-dominated solutions.

Since the utilized multi-objective optimization algorithm (the *Matlab* function `gamultiobj`) does not handle nonlinear constraints, it is essential to manually introduce a penalization to the value of the objective functions if the constraint is not satisfied, or in other words if the solution is non-feasible, starting from a certain tolerance. One simple way to implement this is to sum to each objective $j$ the following quantity:

$$R_j(\mathbf{x}) = V_j\, r(\mathbf{x}) \qquad \text{for } j = 1, \ldots, n_{\text{obj}} \tag{3.35}$$

$$\text{with} \qquad r(\mathbf{x}) = \frac{||C_L(\mathbf{x})|^2 - |\bar{C}_L|^2|}{|\bar{C}_L|^2} \tag{3.36}$$

where $V_j$ is a properly adjusted penalty parameter and $r(\mathbf{x})$ is the error on the constraint.

## 3.8 Aerodynamic moment and actuation power numerical optimization

It is possible to repeat the multi-objective optimization using as second objective the total actuation power coefficient, computed in equation 2.39 instead of the sole aerodynamic power, using the piecewise cubic model for the airfoil camberline.

$$\text{minimize} \qquad |C_M(\mathbf{x})|^2 \text{ and } |C_{W_{act}}(\mathbf{x})|^2 \tag{3.37}$$

$$\text{subject to} \qquad f(\mathbf{x}) = |C_L(\mathbf{x})|^2 - \bar{C}_L^2 = 0, \tag{3.38}$$

$$x_i \in [\text{LB}, \text{UB}] \text{ for } i = 1, \ldots, n_{\text{var}} \tag{3.39}$$

This optimization gives a more global point of view on the actual required power. Since the three power contributions are differently phased the global actuation power is not only a simple amplification of the aerodynamic power, hence the optimal shapes are supposed to be quite different.

# CHAPTER 4

# RESULTS

## 4.1 Aerodynamic Moment Optimization

In the following sections the results of the numerical optimizations of the quarter-chord aerodynamic moment are illustrated. Results are obtained with different chord modelizations (flaps or cubic spline) and different number of degrees of freedom.

### 4.1.1 Airfoil with a single flap

This is the simplest case taken into account, for which an analytical solution is also available (see section 3.4).

First of all it is reasonable to report some convergence test for both the SQP and GA methods, using the algorithms implemented respectively in the functions `fmincon` and `ga` in the software *Matlab*, for different values of reduced frequency and lift constraint. The geometry of the airfoil is instead fixed, being the flap hinge set at $\tilde{x}_F = 0.5$.

As it can be seen from Figures 4.1 and 4.2, the convergence is good in every test case, and takes only a small amount of time thanks to the high efficiency of SQP algorithms in such a problem.

Now it is possible to use the tested methods to obtain the variation of the optimal solutions with the reduced frequency $k$. Both symmetrical solutions can be found by changing the initial guess, or by redundantly employing the multi-start approach (no local optima exist in the boundaries, as seen in the contour plot in figure 4.1).

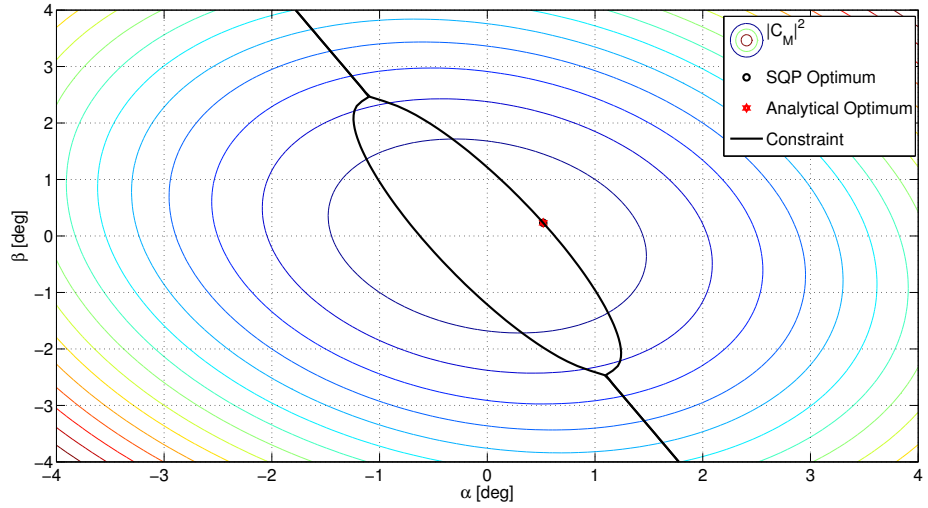


(A) $\bar{C}_L = 0.05$

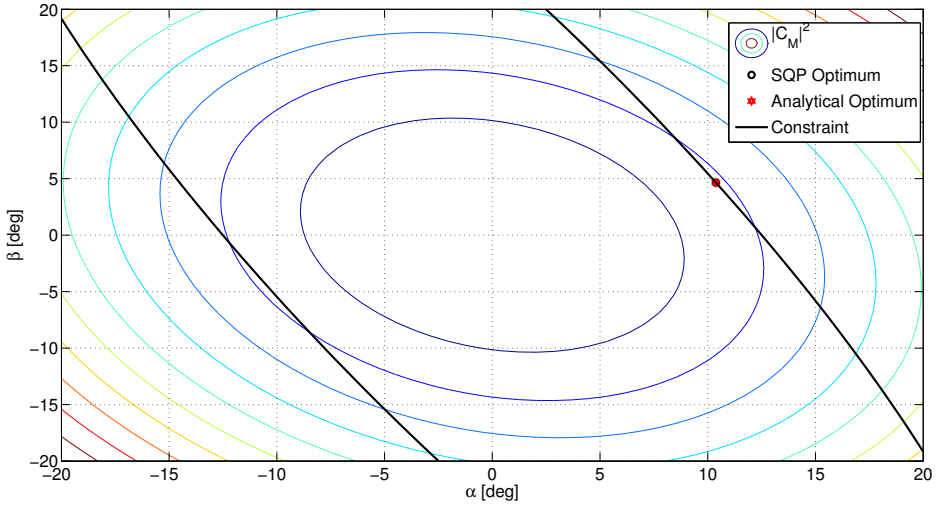


(B) $\bar{C}_L = 1$

FIGURE 4.1. Comparison between analytical and SQP solutions for a single-flapped airfoil moment optimization, $k = 0.5$

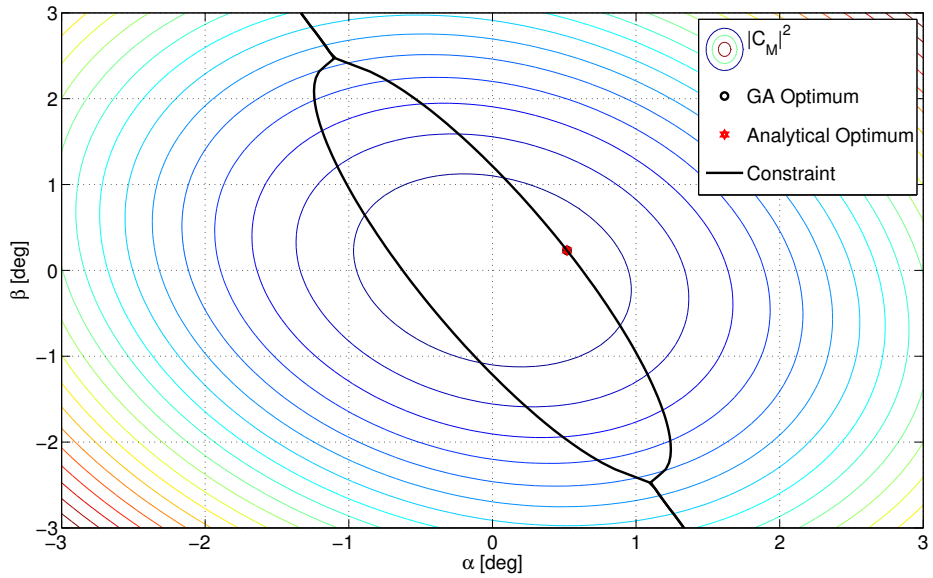


(A) $\bar{C}_L = 0.05$

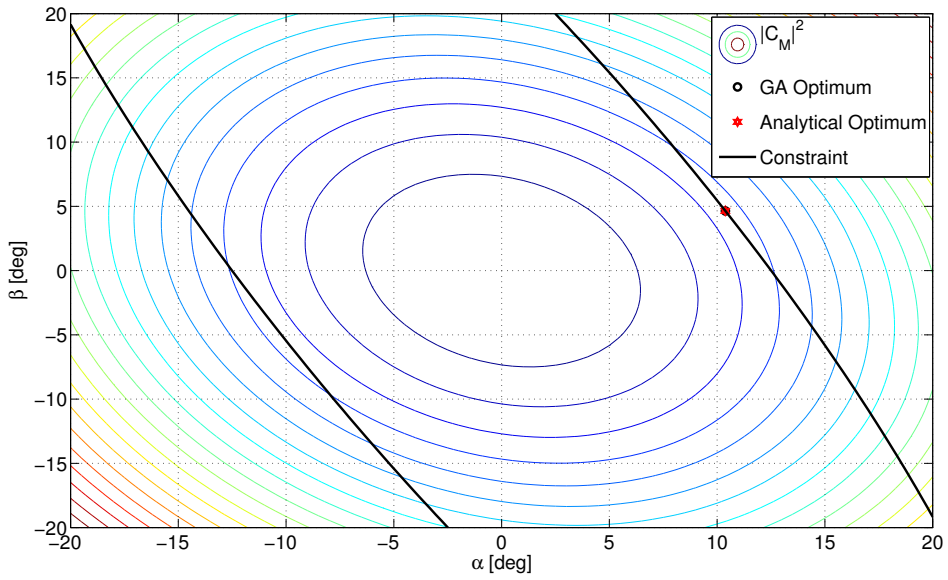


(B) $\bar{C}_L = 1$

FIGURE 4.2. Comparison between analytical and GA solutions for a single-flapped airfoil moment optimization, $k = 0.5$

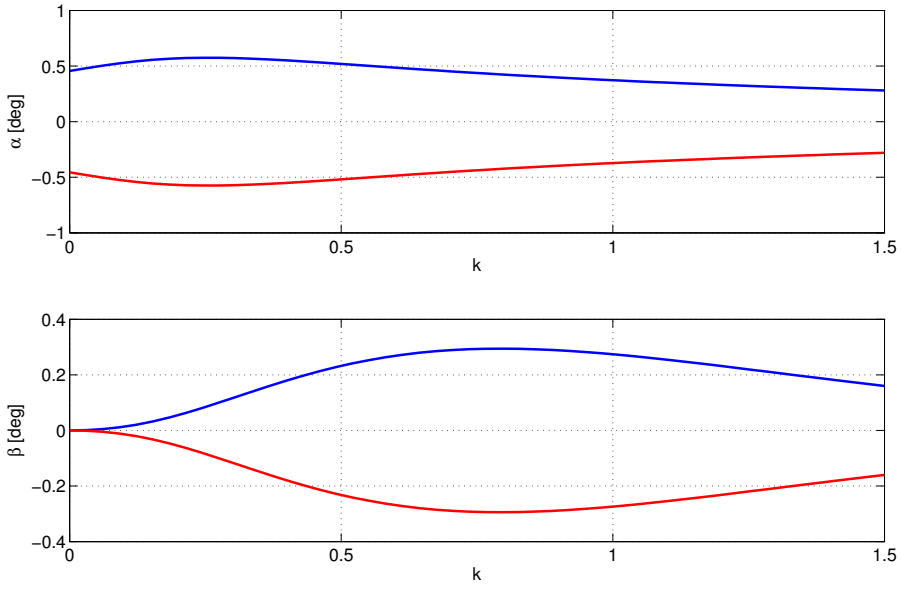


(A) $\bar{C}_L = 0.05$

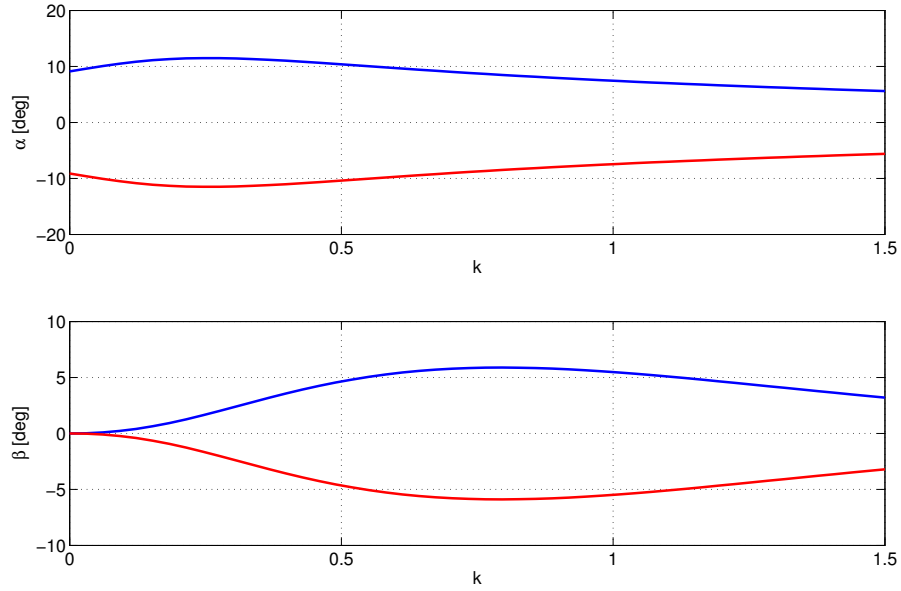


(B) $\bar{C}_L = 1$

FIGURE 4.3. Variation of the optimal solution with respect to the reduced frequency for a single-flapped airfoil, minimizing the aerodynamic moment, $\tilde{x}_F = 0.5$

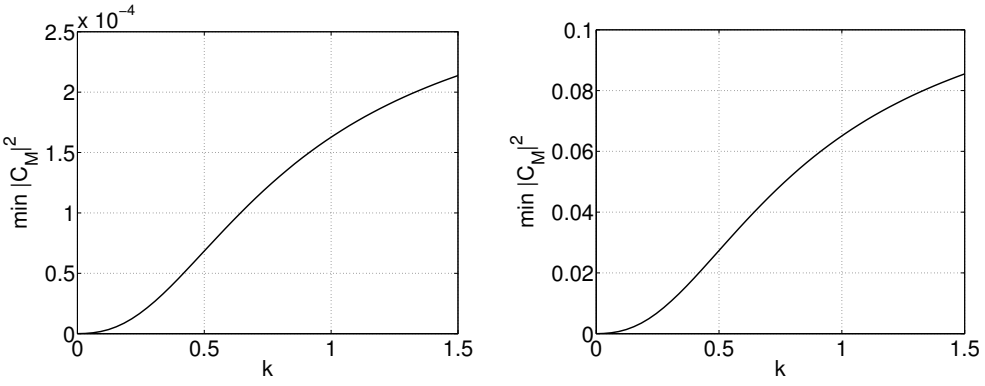


(A) $\bar{C}_L = 0.05$ (B) $\bar{C}_L = 1$

FIGURE 4.4. Variation of the optimal moment with respect to the reduced frequency for a single-flapped airfoil, $\tilde{x}_F = 0.5$

This case is too simple to deduce any general consideration on the behaviour of a morphing airfoil and the feasibility of the optimization. It is nevertheless useful firstly as a test case, secondly because the use of a flap is the simplest, yet not frequently used in rotor blades, solution to change the airfoil camber. It is remarkable that optimal angles increase until certain values of reduced frequencies, then the trend inverts and they start to decrease. This can possibly be associated with the role played by the circulatory and non-circulatory parts of the aerodynamic forces (remember that the quarter-chord moment do not depend on the Theodorsen function, as explained in section 1.1.1, but the lift does): the initially higher weight of the circulatory part decreases until, at a certain value of reduced frequency, the non-circulatory part becomes more relevant, causing the inversion of the trend. The frequencies at which the change happens are different for $\alpha$ and $\beta$. It goes without saying that the angles oscillation amplitudes required to obtain higher lift coefficient oscillations are greater. Lastly, it can be noticed that the higher the reduced frequency, the larger is the optimal value of the aerodynamic moment.

Another thing that is interesting to investigate is the behaviour of the optimal solutions with respect to a translation of the flap hinge. This will translate into a variation of the flap surface, *i.e.* of it's effectiveness. The hinge coordinate is changed from 50% to the 80% of the chord. It can be seen from figures 4.5 and 4.6 that, while the optimal moment remains essentially unchanged, the trend of the angles, especially the flap deflection $\beta$, changes drastically with the position of the flap hinge. It is important to notice that at a certain frequency (it is clearly visible in figure 4.5, A and

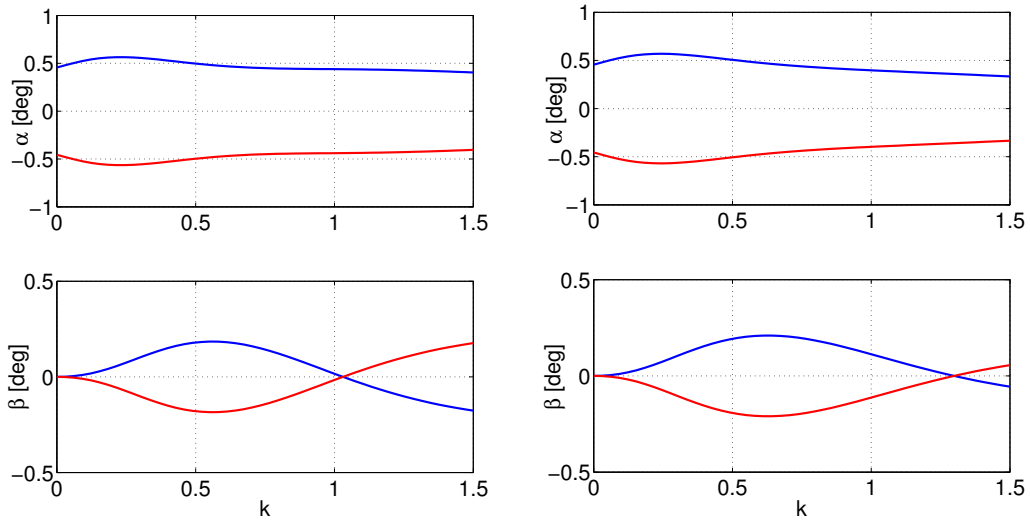


(A) $\tilde{x}_F = 0$




(B) $\tilde{x}_F = 0.2$

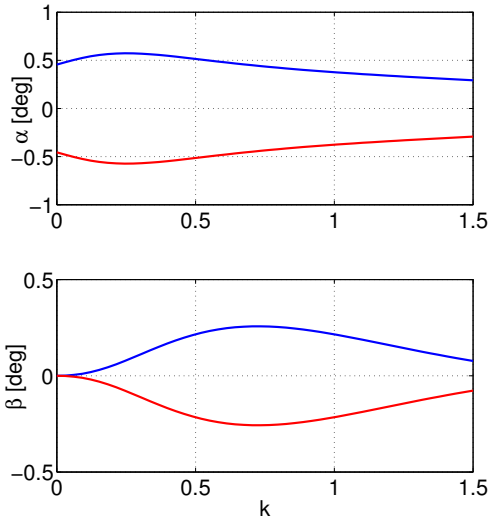


(C) $\tilde{x}_F = 0.4$

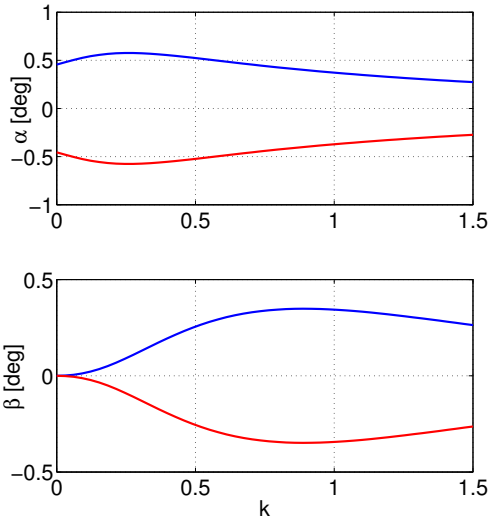


(D) $\tilde{x}_F = 0.6$

FIGURE 4.5. Variation of the optimal solution with respect to the reduced frequency for a single-flapped airfoil, minimizing the aerodynamic moment at different hinge positions, $\bar{C}_L = 0.05$

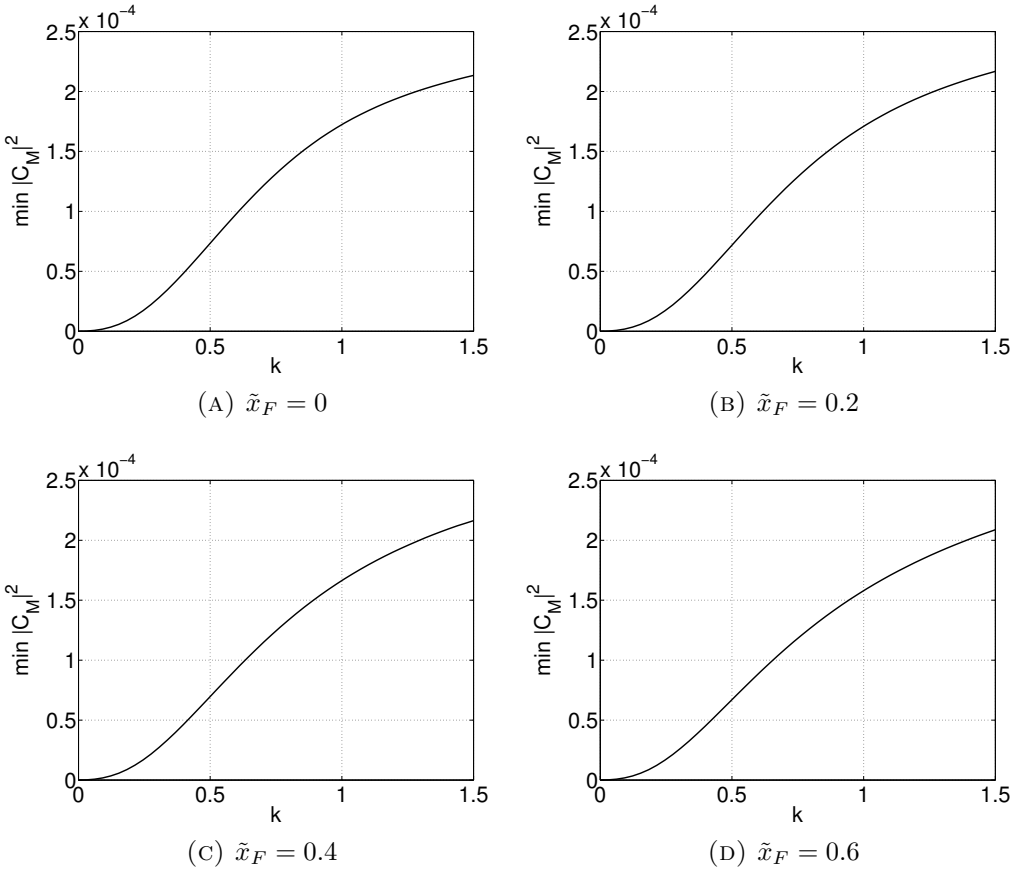


(A) $\tilde{x}_F = 0$ (B) $\tilde{x}_F = 0.2$

(C) $\tilde{x}_F = 0.4$ (D) $\tilde{x}_F = 0.6$

FIGURE 4.6. Variation of the optimum moment with respect to the reduced frequency for a single-flapped airfoil, minimizing the aerodynamic moment at different hinge positions, $\bar{C}_L = 0.05$

B) the optimal flap deflection becomes null. The *leitmotif* however is that bigger flaps require smaller deflection to obtain the optimality.

Results for the other trim condition $\bar{C}_L = 1$ are not shown here, because are substantially the same, just with a different scale (same eigenvector, different amplitude in order to fit the new constraint value).

### 4.1.2 Airfoil with two flaps

The optimization of the moment can be extended to an airfoil with two serially hinged flaps, taking into account the usual lift constraint.

Firstly it is possible to carry out the analytical computation of the optimal solution through the eigenvalue problem, as explained in section 3.4. Some results are reported in table 4.1. Only real eigenvectors are considered,

because complex eigenvectors are connected with a change in the phase of the airfoil movement, which, although interesting, is not the simplest solution, so this work is not going to focus on it any further. It can be seen that

| $\bar{C}_L$ | Real Eigenvector $\mathbf{x}_1$, $[deg]$ | Real Eigenvector $\mathbf{x}_2$, $[deg]$ |
|---|---|---|
| 0.05 | $\pm\left\{-0.745 \quad -2.233 \quad 4.651\right\}^T$ | $\pm\left\{1.953 \quad -12.213 \quad 12.445\right\}^T$ |
| 1 | $\pm\left\{-14.911 \quad -44.6703 \quad 93.014\right\}^T$ | $\pm\left\{39.052 \quad -244.3 \quad 248.9\right\}^T$ |

TABLE 4.1. Analytical optimal solutions for $\tilde{x}_p = -0.5$, $\tilde{x}_F = 0.4$, $\tilde{x}_{F_1} = 0.6$, $k = 0.5$

without imposing any boundary the optimal solution for relatively high trim conditions consists in huge flap deflections, far beyond any reasonable stall limit. So boundaries are necessarily to be taken into account when using a numerical method.

Here only SQP solutions on varying of $k$ are displayed, since the algorithm for such a problem produces more accurate solutions in less time than GA. It is noticeable in figure 4.7 that the optimal shape assumed by the airfoil is connectable to the mean line of an autostable airfoil: while one flap is bent upward, the other goes downward, and vice versa for the other symmetrical solution. The solution obtained by the numerical method at $k = 0.5$ and $\bar{C}_L = 0.05$, that is when boundaries do not intervene, are the same as the one obtained analytically in eigenvector $\mathbf{x}_2$: this in an indicator of good convergence.

Moreover, in the case with higher trim value, one of the flap deflection angles saturates to the highest value allowed by the bounds: this happens because the unbounded optima was beyond the imposed limit. So, while one flap saturates, the other, in conjunction with the incidence $\alpha$, adapts its movement in order to accomplish the optimality condition at each reduced frequency $k$. Verified this, it is possible to concentrate only on the trim condition $\bar{C}_L = 0.05$ in further moment optimizations, because it is more interesting to see how the variables act unlimitedly, as boundaries here are imposed too empirically and do not have any strong physical meaning that makes them play such an influential role in the optimization process. Moreover, these big displacements needed to optimize the moment with such an high lift constraint are expected to easily lead to separations (steady or dynamic), making these solution not particularly interesting.

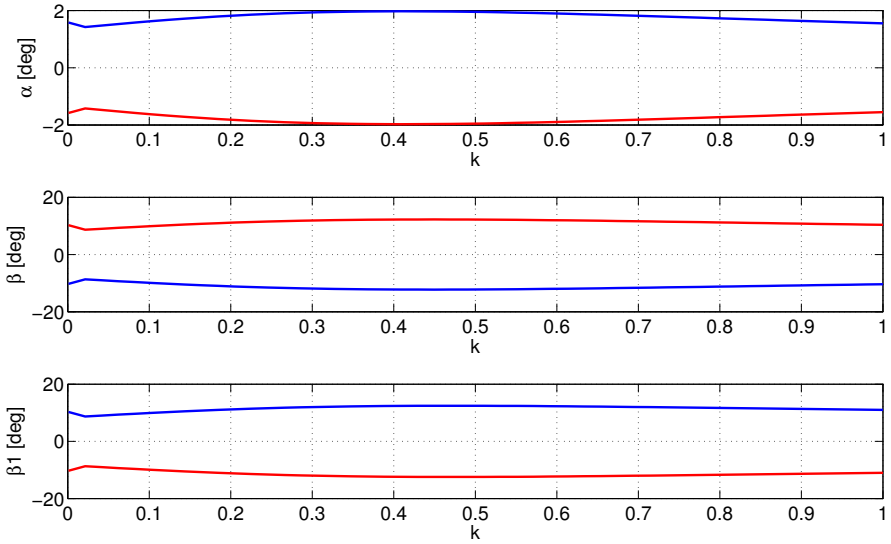


(A) $\bar{C}_L = 0.05$

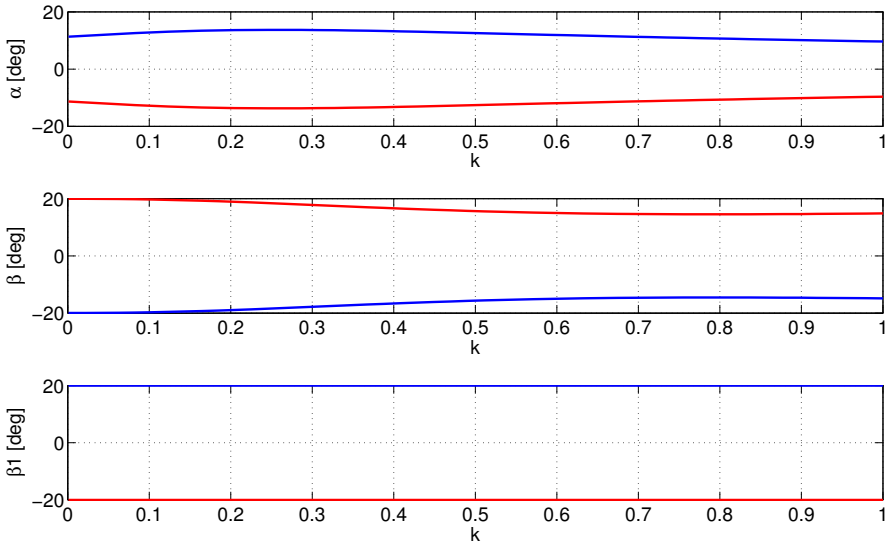


(B) $\bar{C}_L = 1$

FIGURE 4.7. Variation of the optimal solution with respect to the reduced frequency for a double-flapped airfoil, minimizing the aerodynamic moment, $\tilde{x}_F = 0.4$, $\tilde{x}_{F_1} = 0.6$

### 4.1.3 Cubic mean-line

It is now possible to change the model adopted for the chord deformation and use a cubic polynomial. The coefficient $D$ is kept null in order to prevent the vertical translation of the whole airfoil (plunge movement), as it has been done for the flapped airfoil. This leaves three degrees of freedom as optimization variables. As usual, the solution is computed for different reduced frequencies and is shown in Figure 4.8.

It is worth to notice that also here the amplitude of optimal oscillations of the camberline increases at first, then, at a certain reduced frequency around $k = 0.6$, it starts to decrease, due probably to the growth of the non-circulatory effects.

Since the interpretation of the coefficients of the cubic polynomial is not as immediate as the understanding of the flaps deflection angles, an example of the appearance of the mean-line is displayed in Figure 4.9. It can be noticed that the shape is once again similar to a auto stable airfoil (or even more, because now the mean-line is regular) with two opposite cambers. This is important because confirms what already noticed for the serially hinged flaps.

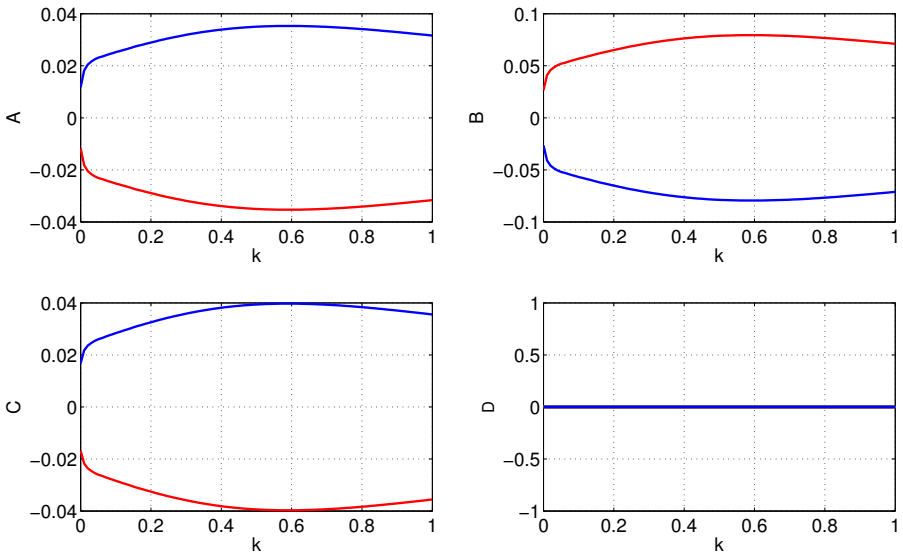


FIGURE 4.8. Optimal solution for the moment optimization, cubic mean-line, $\bar{C}_L = 0.05$

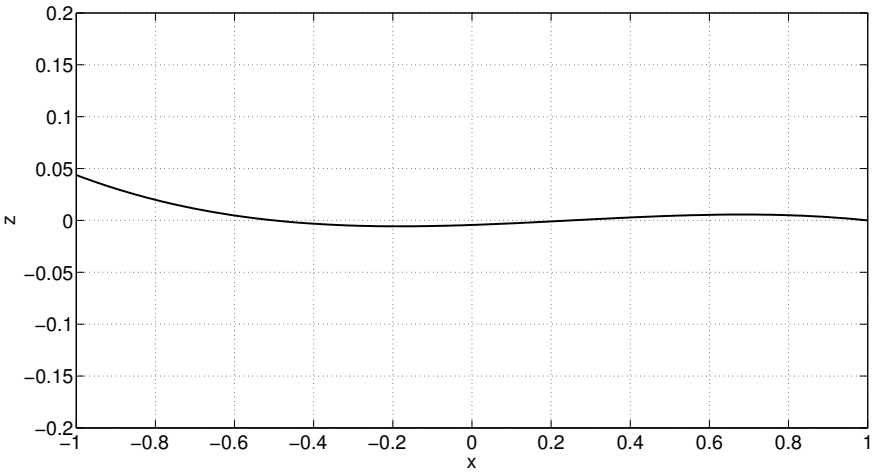


FIGURE 4.9. Example of optimal shape for the moment optimization, cubic mean-line, $k = 0.5$, $\bar{C}_L = 0.05$

### 4.1.4 Piecewise Cubic, two pieces

The aerodynamic moment optimization can be repeated for the piecewise cubic modelization of the chord, starting by considering only two cubic pieces, regular up to the second derivative, as described in section 1.3.2. In this way the number of optimization variables increases to four. The optimization is once again carried out only with SQP method.

This minimization problem is quite awkward, because values assumed by the moment in nearly optimal conditions are so small that are close to the numerical method tolerance and because the function is also very flat at that neighbourhood. Hence it is difficult to obtain accurate results, therefore no solution is displayed here.

## 4.2 Aerodynamic Moment and Power Optimization

In the following sections are displayed the results of the numerical multi-objective optimization of the quarter-chord aerodynamic moment and aerodynamic power, with both flap and spline representations of the chord and different degrees of freedom number.

The simple example of an airfoil with a single flap is not developed because the number of the variables is too low in order to manage the optimization of two functions and the constraint satisfaction.

### 4.2.1 Airfoil with two flaps

This is the first and simplest multi-objective optimization fulfilled. It is useful, despite the basic model, because it allows to understand the working principles of the different optimization methods used when facing a multiple objective problem, namely the direct optimization with a genetic algorithm (in particular the function `gamultiobj` implemented in *Matlab* environment, a slight variation of NSGA-II procedure) and the scalarization technique combined with SQP (see section 3.3). The computation is repeated for different reduced frequencies.

The introduction of the aerodynamic power as a new objective in the optimization problem is expected to reduce the optimal amplitude of the angles with respect to the moment single-objective minimization, in order to reduce the power with an optimal combination of angles and hinge moments.

Here are shown the obtained Pareto fronts and the variation in the optimal solutions with the weight $A$. It can be seen in figure 4.10 that GA and SQP Pareto fronts are quite similar, confirming the good convergence of both methods. However, in this particular problem, if the scalarization weight is properly adjusted, SQP is allowed to produce a more accurate solution, since the method is able to satisfy the constraint within a better tolerance, due to its intrinsic features (GA relative maximum error on the constraint is a little less than $10^{-2}$, SQP is able to reach $10^{-6}$ without any problem).

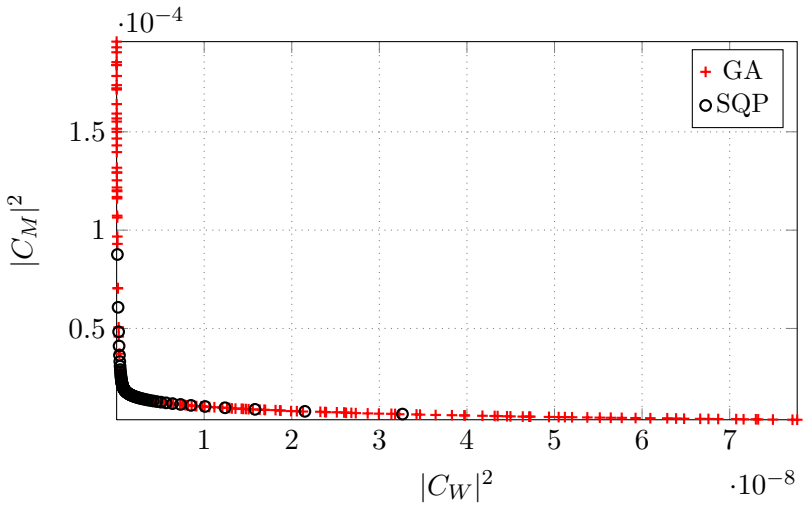


FIGURE 4.10. Pareto front, two flaps model, $k = 0.3$, $\tilde{x}_F = 0.4$, $\tilde{x}_{F_1} = 0.6$ $\bar{C}_L = 0.05$

As expected, it can be noticed that for small values of $A$, that is when the trade-off solution are more power-minimization oriented, angles are kept

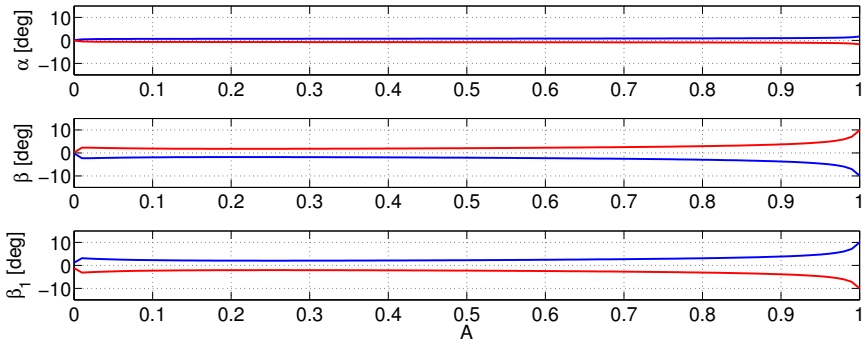


FIGURE 4.11. Optimal solution with respect to the weight $A$ defined in eq. 3.34, two flaps model, $k = 0.3$

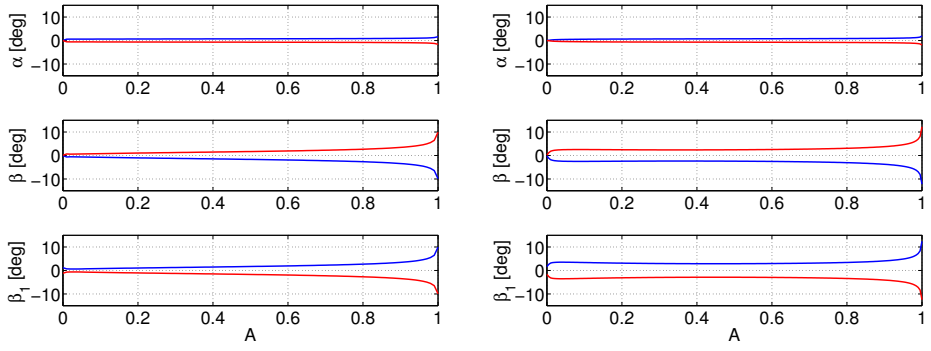


(A) $k = 0.1$ (B) $k = 0.5$

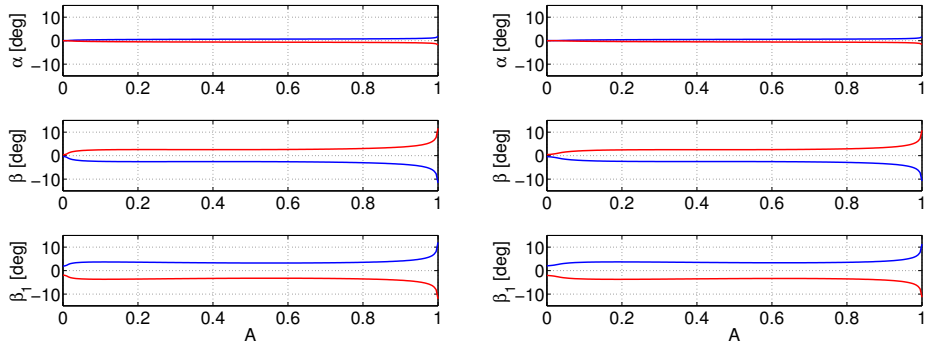


(C) $k = 0.7$ (D) $k = 0.9$

FIGURE 4.12. Optimal solution with respect to the scalarization weight $A$, two flaps model, $\bar{C}_L = 0.05$

smaller (figure 4.11), while for bigger values they increase visibly, minimizing mainly the moment. However, the displayed trend varying the parameter $A$ is not to be considered totally informative, since it also depends on the weight $\gamma$ used. The global shape of the mean-line remains the one of an autostable airfoil, with the two flaps oppositely deflected.

Figures 4.11 and 4.12 are useful to observe the variation of the multi-objective optimal solution with respect to the reduced frequency $k$. On the moment-oriented optimization side ($A \approx 1$) happens what has been described in section 4.1.2: initially the optimal angles start to increase, then, at a certain frequency, it decreases again. Instead, on the other side ($A \approx 0$ and halfway) it seems that the optima are increasingly bigger with $k$, even though at some weight values the trend may tend to decrease starting from certain frequencies.

### 4.2.2 Piecewise cubic mean-line

The multi-objective optimization is now repeated with the adoption of the piecewise cubic model for the airfoil mean-line motion. Initially only two pieces of cubic are considered. Once again both GA and SQP methods are used, and only the trim condition $\bar{C}_L = 0.05$ is taken into account.

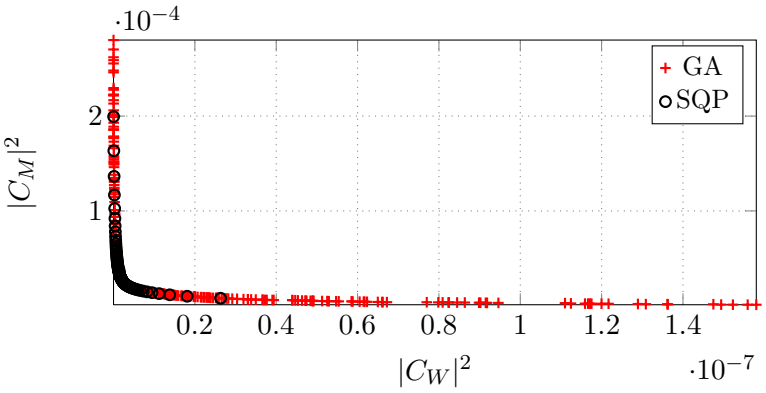


FIGURE 4.13. Pareto front, two-pieces cubic spline model, $k = 0.4$, $\tilde{x}_F = 0.5$, $\bar{C}_L = 0.05$

Figure 4.13 shows that also this time the two numerical optimization methods solutions are close enough to assert that the convergence is good. Obviously the precision of the genetic algorithm continues to be worst than the one of the gradient-based method, and the accuracy may vary on each computation due to the randomness of the method. Nevertheless, thanks to this feature, GA is able to give a more widespread front. Furthermore, it is

noticeable that the appearance of the Pareto front is comparable to the one in figure 4.10.

To understand the different optimal displacements of the airfoil at different trade-off between the two objectives, in figure 4.14 are plotted the shapes and the associated pressure difference distributions for the non-dominated solution with minimum power, the one with minimum moment and lastly one intermediate solution. It is noticeable that the deformations assumed by the

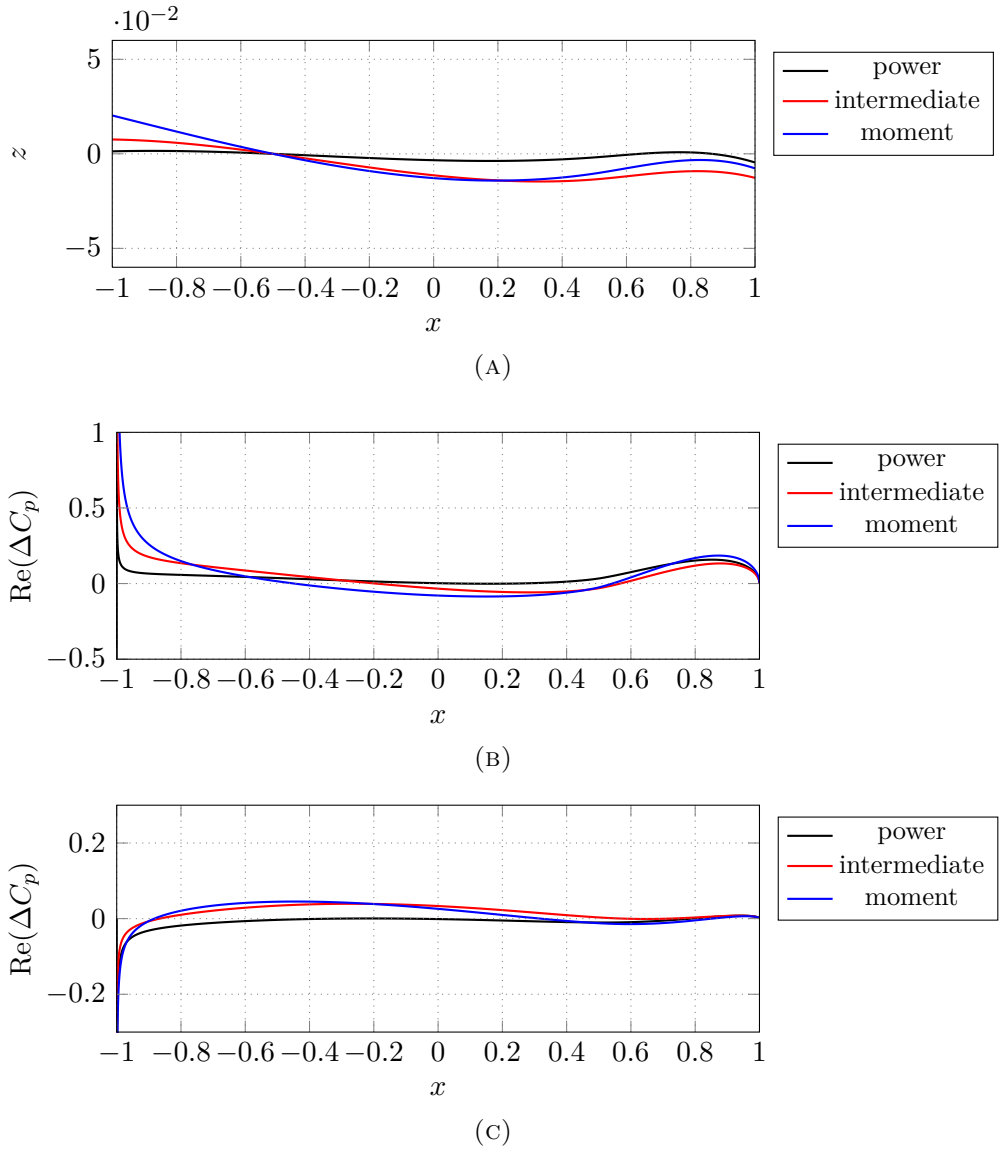


FIGURE 4.14. Optimal shapes at different parts of the Pareto front, $k = 0.4$, $\bar{C}_L = 0.05$

airfoil are again smaller if one wants to get to a better power, but now the general configuration of the airfoil is no longer the one of an autostable airfoil with a double convexity, but a third change in curvature sign can now be seen, at least for some solutions in the front (*e.g.* in figure 4.14a, black and red lines). In figure 4.14a, blue line, the airfoil deforms with just two curvatures, and the forward part remains quite flat, taking only some incidence. The deformation with two changes in curvature sign is able to keep the pressure distribution really flat (figures 4.14b and 4.14c, black), that, combined with the small displacements, allows the power to be minimized.

One question may now arise: is this model capable to predict the real optimal shape of the airfoil or more optimization variables are needed? In order to answer this question in the following section the computations will be repeated for cubic splines with an increased number of pieces, and consequently with more design parameters. If the deformation appearance remains nearly the same, although the increased number of parameters would allow a more convoluted shape, it means that the parametrization of the mean-line is thick enough to describe the optimal solution.

### Convergence

In order to verify the convergence of the spline mean-line model, as stated previously, it is possible to compute the non-dominated solutions using firstly a three pieces cubic spline, then increasing the number of pieces (and variables) to see if optimal shapes change drastically or remain quite similar. Some solutions are displayed here in figures 4.15, 4.16, 4.17, 4.18, 4.19.

It can be seen that for three, four and five pieces of spline, although the convergence of GA becomes more and more delicate, while SQP becomes slower, the obtained optimal Pareto fronts are very similar (figure 4.16), which means that the addition of a degree of freedom does not affect the optimal value of the objective functions so much. Hence, it is possible to assert that with $N_t = 4$ there are enough degrees of freedom in order to represent the correct optimal shape, taking into account that high accuracy is not needed. It is also noticeable from this figure that increased values of $k$ correspond to higher optimal values in the objective functions.

Figure 4.15 shows the comparison between some optimal shapes for different number of spline pieces $N_t$. It is possible to notice that the shapes are quite similar, and the differences are probably caused by a different convergence of GA, especially for $N_t = 5$, where convergence is more critical due to the higher number of variables. Differences are also caused by a slightly different position in the Pareto front of the solution.

Instead if the number of pieces of the cubic spline is raised too much,

for example considering eight pieces, the optimization problem becomes bad conditioned and the obtained optimal shapes start to present local oscillations that are not intended to exist.

This suggests that a good number of pieces of spline is $N_t = 4$, where degrees of freedom are enough to give a good representation of the solution but are not too much, avoiding convergence numerical problems.

As can be seen from figure 4.17, generally speaking the optimal mean-line deformations are always constituted by a three cambers shape, but the particular shape and amplitude of the displacement depends on the reduced frequency and the position of the solution in the Pareto front: solutions that minimize mostly the power tend to perform smaller oscillations, keeping also the pressure difference distribution smaller (see 4.18, 4.19).

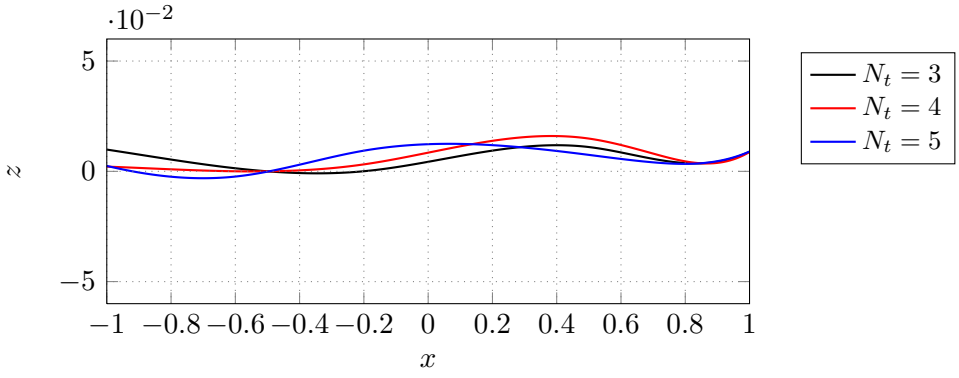


(A) $k = 0.5$, minimum power

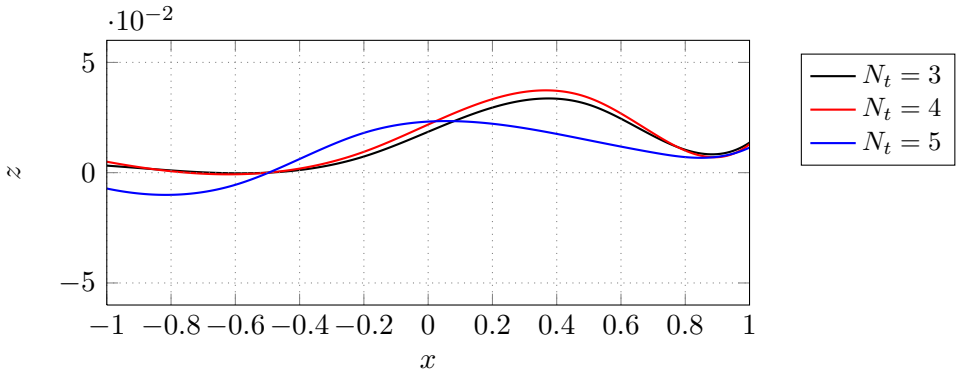


(B) $k = 0.5$, minimum moment

FIGURE 4.15. Optimal solutions comparison at different $N_t$

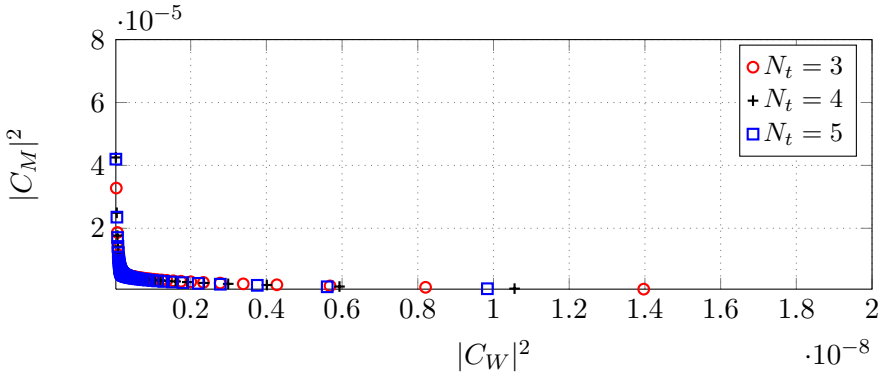


(A) $k = 0.2$

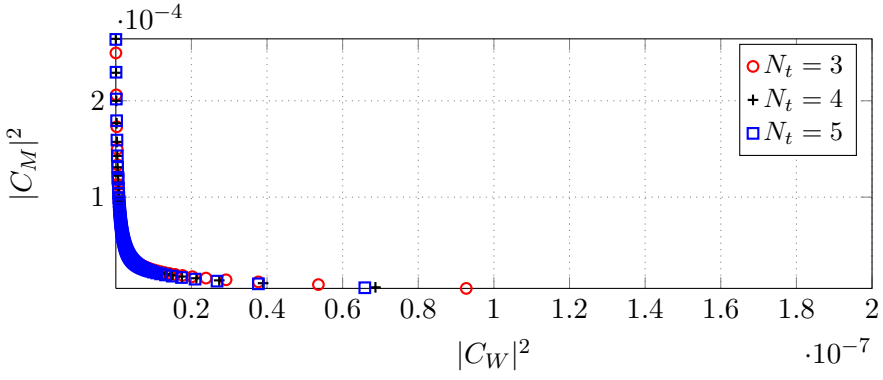


(B) $k = 0.5$

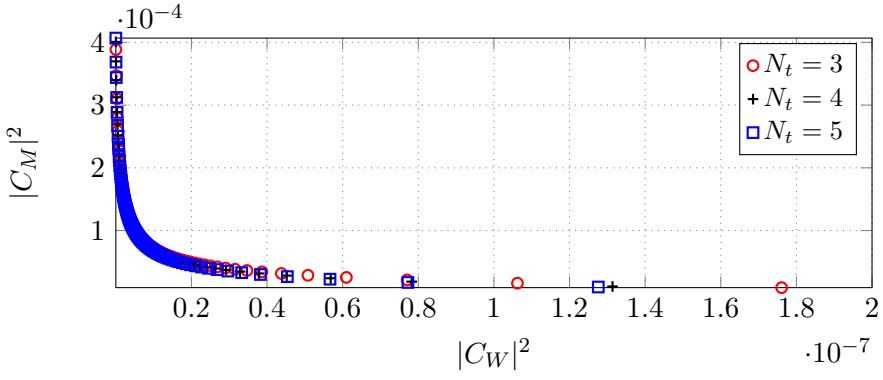


(C) $k = 0.8$

FIGURE 4.16. Pareto fronts with different $N_t$ comparison at different $k$

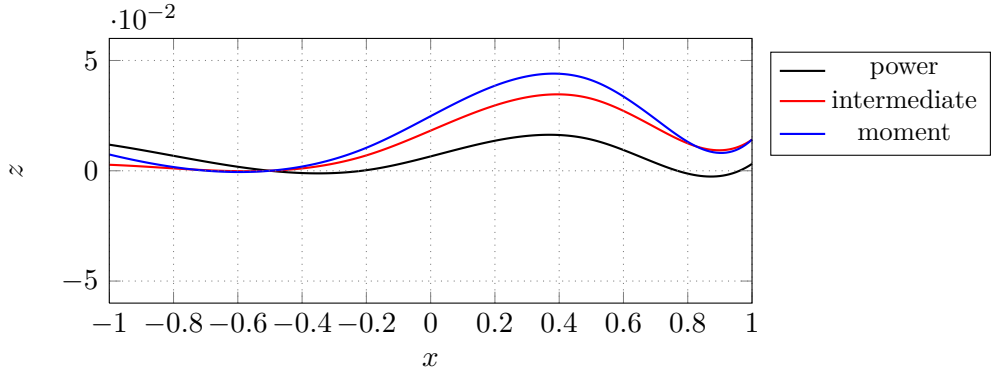


(A) $k = 0.2$

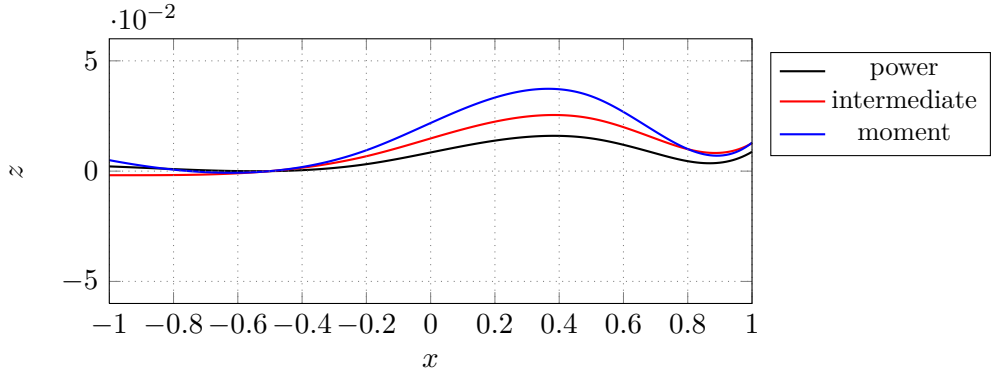


(B) $k = 0.5$

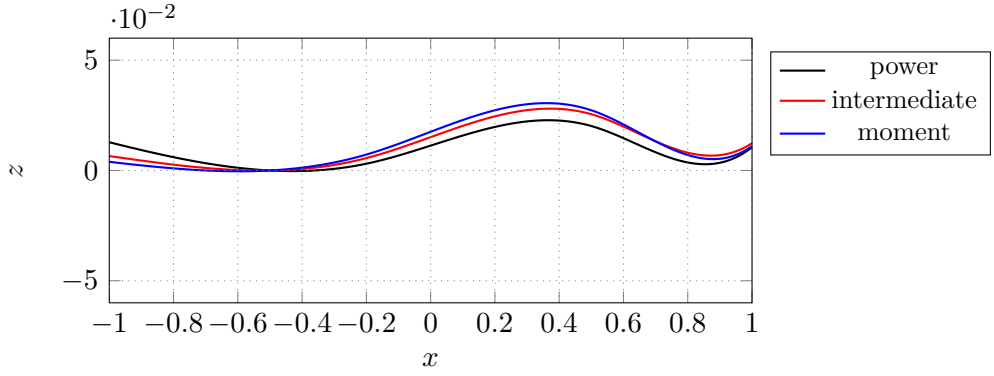


(C) $k = 0.8$

FIGURE 4.17. Optimal solutions comparison at different $k$, $N_t = 4$

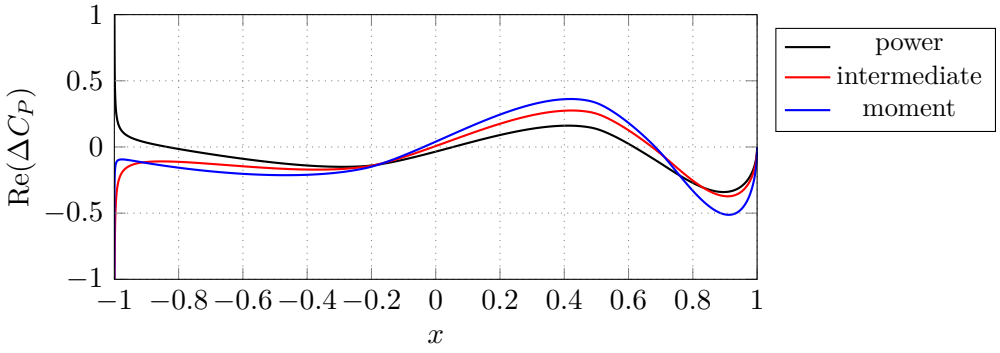


(A) $k = 0.2$

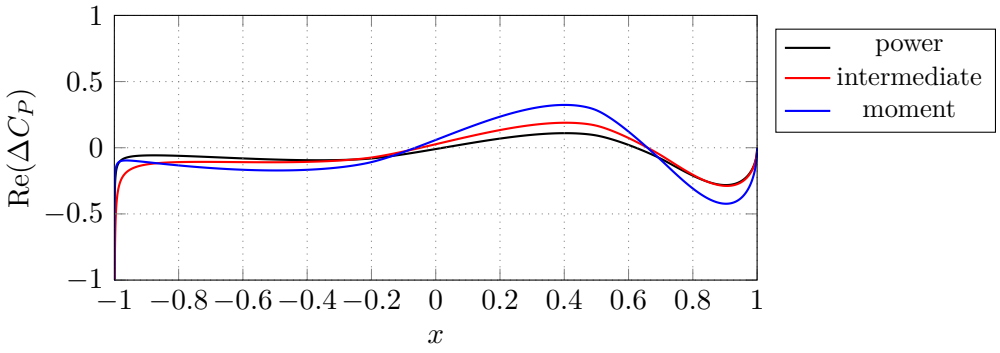


(B) $k = 0.5$

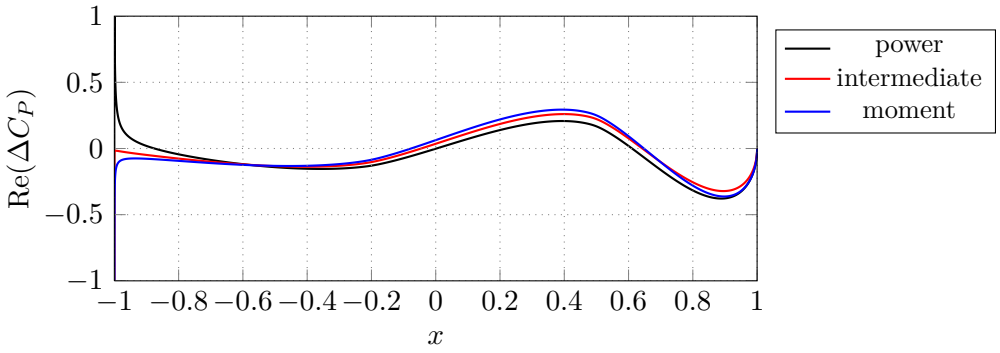


(C) $k = 0.8$

FIGURE 4.18. Optimal pressure difference comparison at different $k$, $N_t = 4$, real part

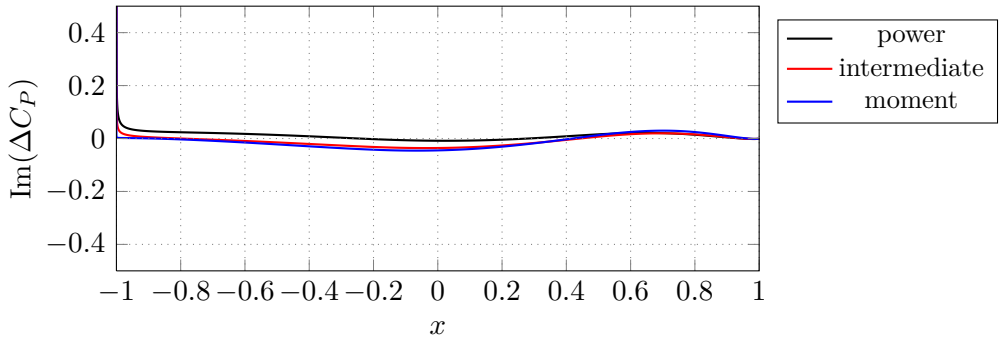


(A) $k = 0.2$

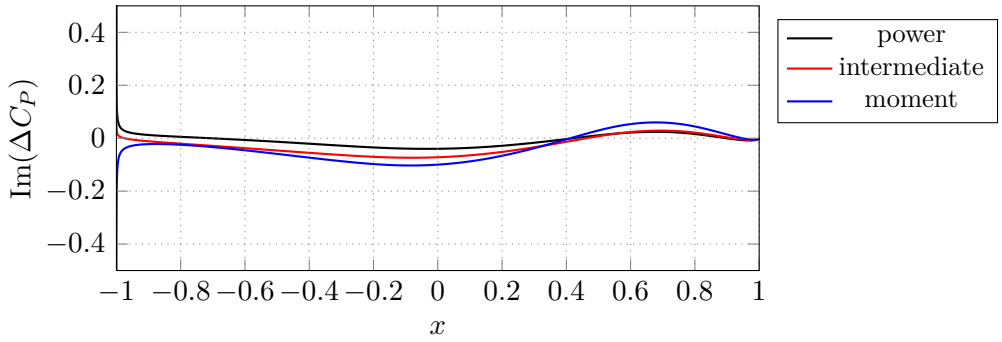


(B) $k = 0.5$

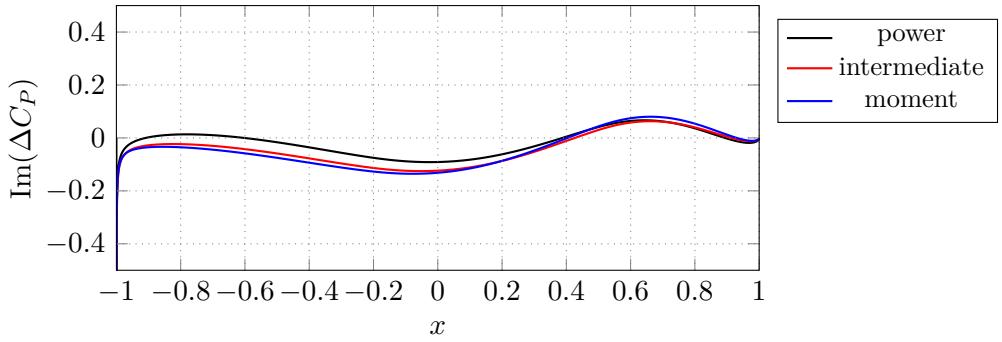


(C) $k = 0.8$

FIGURE 4.19. Optimal pressure difference comparison at different $k$, $N_t = 4$, imaginary part

## 4.3 Aerodynamic Moment and total Power Optimization

It is possible to repeat the multi-objective optimization using as the second objective the total actuation power, computed in equation 2.39, instead of the sole aerodynamic power, using the piecewise cubic model for the airfoil camberline in order to have a more physically significative objective. As verified in section 4.2.2, a number of pieces $N_t = 4$ is sufficient for the solution to converge, hence only this number of parameters is taken into account. The degree of freedom associated to the rigid rotation is initially neglected, to consider only the power associated to the mean-line deformation. Optimizations are carried out at different reduced frequencies $k$, beam densities $\rho_s$ and stiffnesses $E_s$, in order to investigate behaviour changes with reference to the dimensionless parameters $\frac{E_s}{\rho U^2}$ and $\frac{\rho_s}{\rho}$. Starting data are typical helicopteristic mean values of $\rho_s = 300\,kg/m^3$ and $E_s = 0.4\,GPa$, extracted approximately basing on the discussion in section 2.3.1 and the data in [24]. Other aerodynamic data are $U = 20\,m/s$ and $\rho = 1.225\,kg/m^3$. Some optimal results are shown in figures 4.20, 4.21 and 4.22.

Figure 4.27 shows the comparison between the two multi-objective optimization performed: the one with aerodynamic power as objective and the other with actuation power instead. It is interesting to notice that, while the overall behaviour remains substantially unchanged, the shapes associated with a power-oriented optimization with the actuation power as objective tend to be flatter with respect to the case of the only aerodynamic power optimization. That is mainly due to the high contribution of the elastic power, which highly penalizes this objective. The inertial contribution is less influential, especially at lower reduced frequencies. This consideration underlines the importance of reducing, within reason, the structural stiffness, to make the deformation process possible with reasonable actuators. The higher required power values can be seen in the non-dominated fronts in figure 4.23.

Conversely, the order of magnitude of the optimal aerodynamic quarter-chord moment and the Pareto-optimal moment-oriented solutions remain essentially the same, since the aerodynamic moment function is not changed.

The weight of the elastic and inertial contribution to the total power can be displayed also varying the values of mean mass distribution and equivalent elastic modulus, for example halving or quartering them. It must be remembered that this do not necessarily imply the only decreasing of the airfoil structural properties, but can be seen as a variation in the flight conditions, namely $U$ and $\rho$, because of the power dependency on the dimensionless

parameters 2.41 and 2.42.

Figure 4.24 is able to display the reduction of the total actuation power associated with a decrease in the equivalent elastic modulus to $E_s = 0.1GPa$. It is possible to repeat the optimization now decreasing the beam density to $\rho_s = 75\,kg/m^3$. The non-dominated phenotype for different reduced frequencies is shown in figure 4.25. It is noticeable that optimal power gets back to the same order of magnitude as the one with the original data set, signifying the minor relevance of the inertial power in the global amount.

Shapes obtained with a lower stiffness (Figure 4.28) tend to be flatter maybe because those particular shapes are able to reduce the actuation power magnitude exploiting phase differences, since the phase between the three power contribution is different. Instead, the deflections computed with a lower density (Figure 4.29) are more similar to the original ones, with some exceptions that can be attributed to a poorer convergence of the optimization.

It is also possible to decrease or increase simultaneously the values of $E_s$ and $\rho_s$ to see if there is any substantial change in the resultant solutions. Figure 4.26 shows the expected reduction and growth in the values of the actuation power. The obtained optimal deflections are displayed in figure 4.30. The overall meaning of the results do not change, only specific amplitudes are slightly different, but the qualitative results remain the same. Quantitative values are not precise enough to be directly compared because of low convergence precision of GA, parametrization differences in SQP Pareto fronts and other details, but this is neither the goal of this work.

An interesting aspect that can be deduced from all this optimization is that the global structure of the mean-line deformation remains basically the same throughout the different non-dominated solution in a single Pareto front and at different values of reduced frequencies and dimensionless numbers, with a change in this parameters involving only restrained changes in amplitudes and curvatures. This feature could be exploited, if more accurate results confirm the trend, for further developments of a morphing airfoil in an unsteady aerodynamic environment.

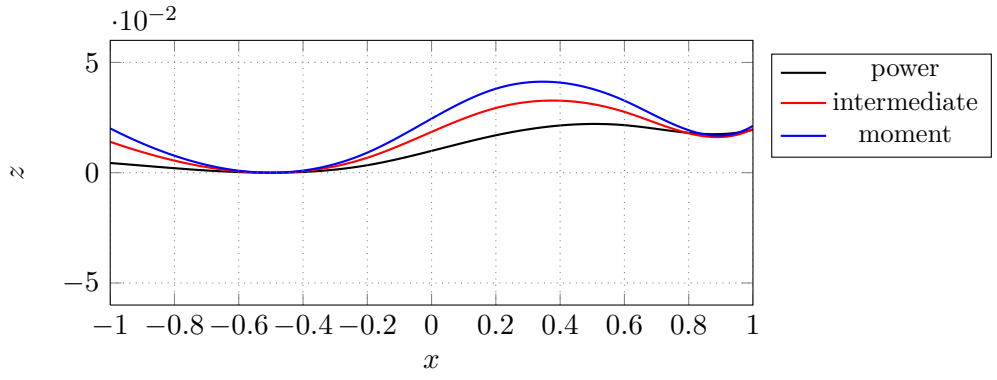


(A) $k = 0.3$

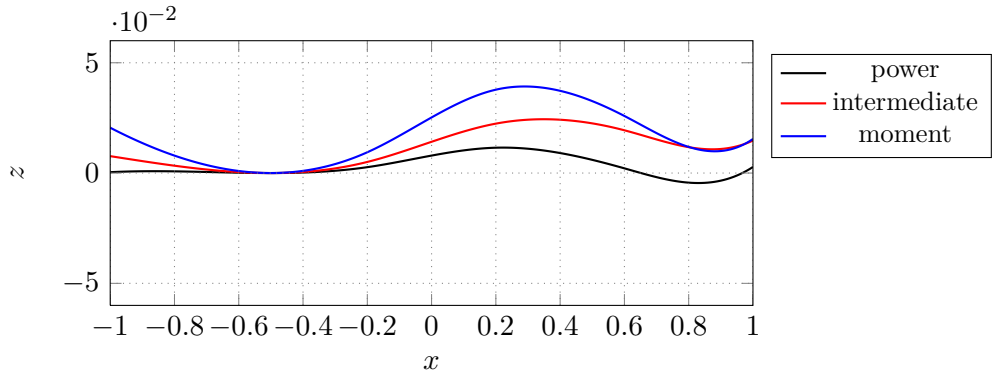


(B) $k = 0.7$

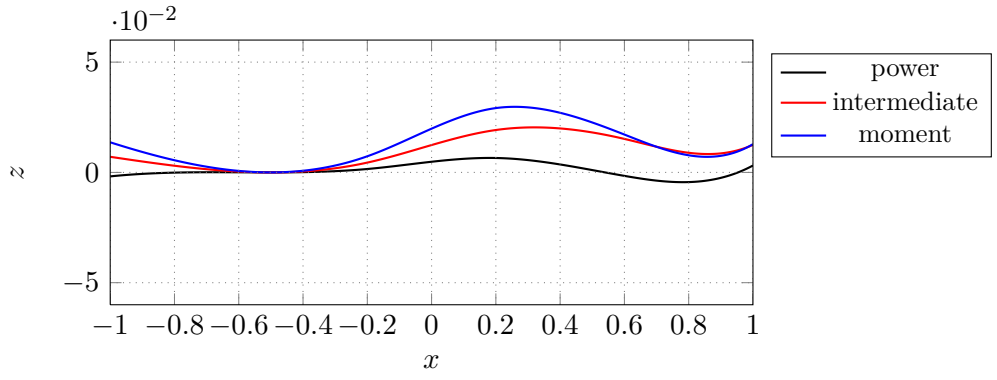


(C) $k = 1.0$

FIGURE 4.20. Optimal solutions comparison at different $k$, $N_t = 4$, $\rho_s = 300\,kg/m^3$ and $E_s = 0.4\,GPa$

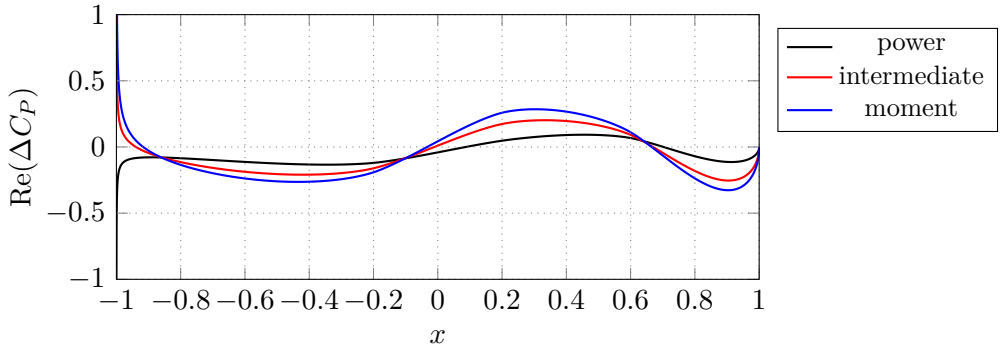


(A) $k = 0.3$

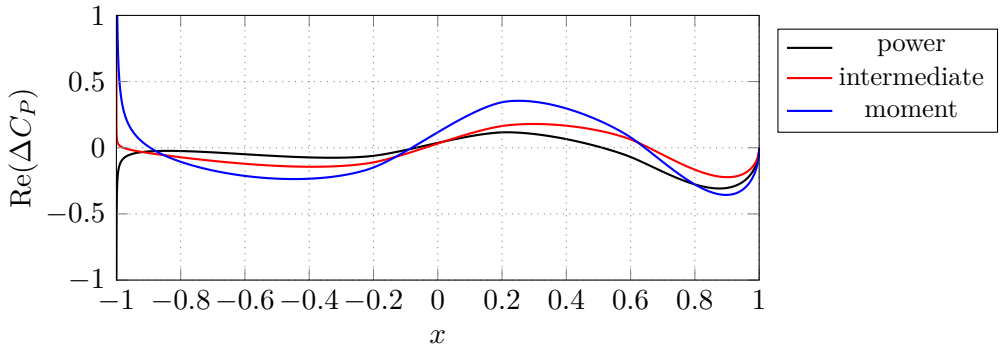


(B) $k = 0.7$

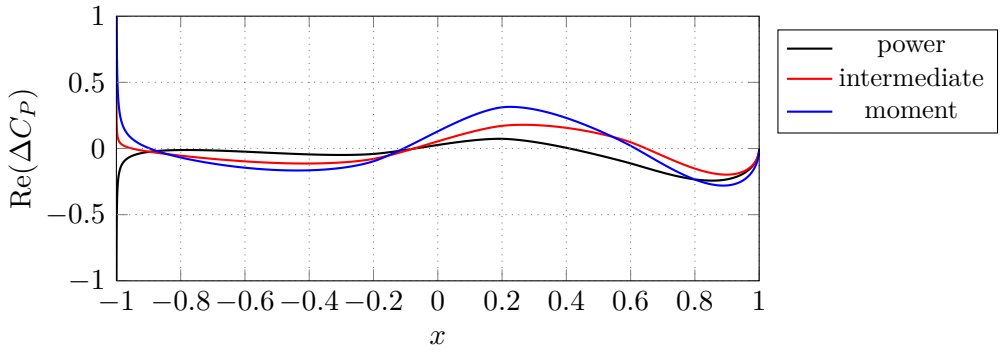


(C) $k = 1.0$

FIGURE 4.21. Optimal pressure difference comparison at different $k$, $N_t = 4$, $\rho_s = 300\,kg/m^3$ and $E_s = 0.4\,GPa$, real part

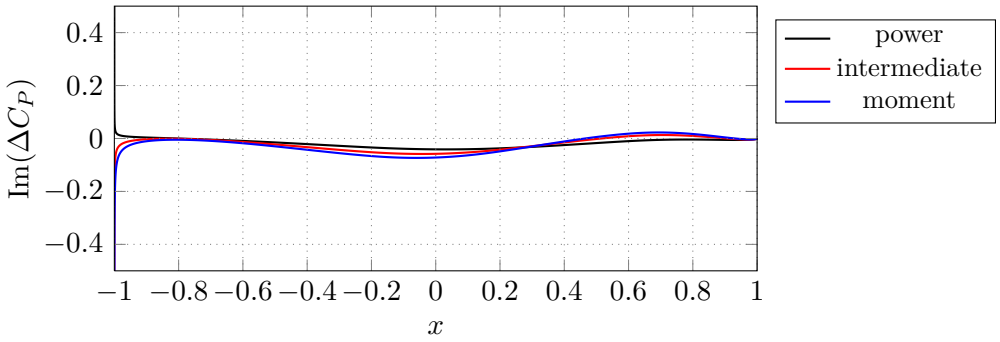


(A) $k = 0.3$

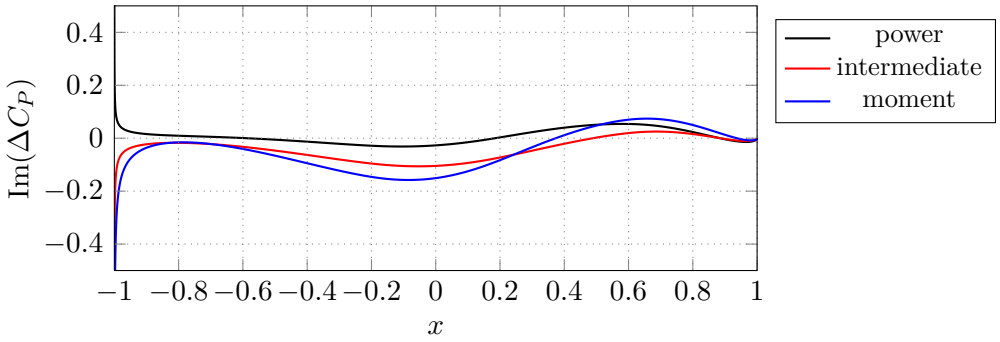


(B) $k = 0.7$

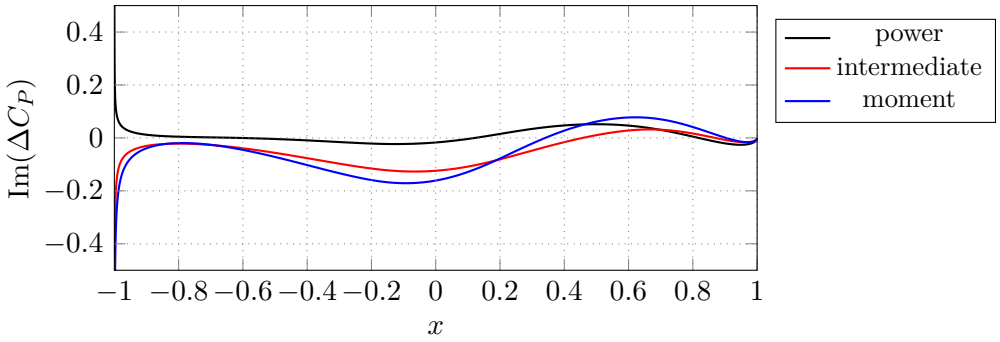


(C) $k = 1.0$

FIGURE 4.22. Optimal pressure difference comparison at different $k$, $N_t = 4$, $\rho_s = 300\,kg/m^3$ and $E_s = 0.4\,GPa$, imaginary part

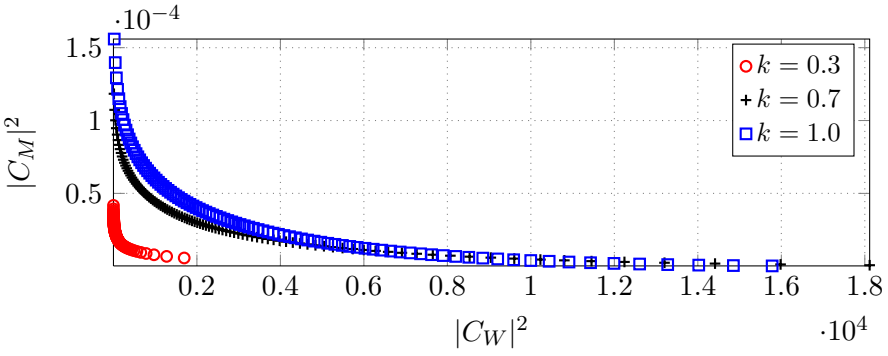


FIGURE 4.23. Pareto fronts comparison at different $k$, $N_t = 4$, $\rho_s = 300\,kg/m^3$ and $E_s = 0.4\,GPa$

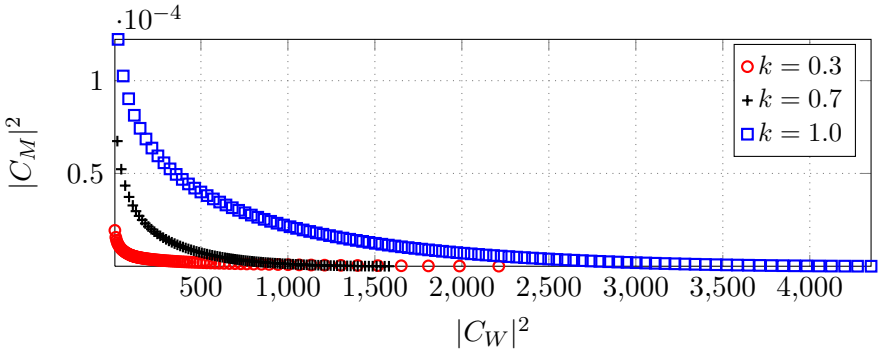


FIGURE 4.24. Pareto fronts comparison at different $k$, $N_t = 4$, $\rho_s = 300\,kg/m^3$ and $E_s = 0.1\,GPa$

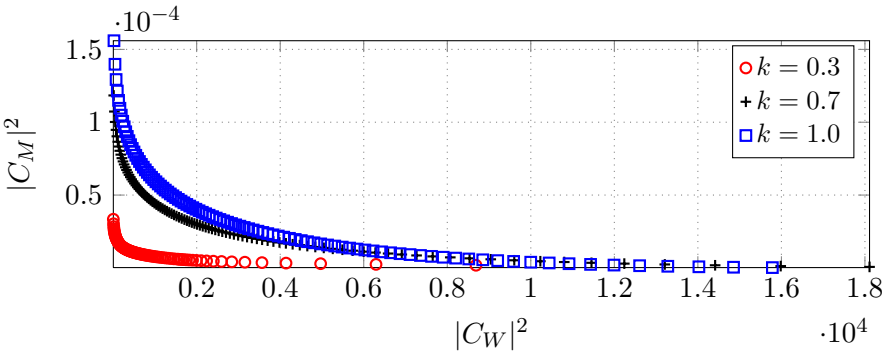


FIGURE 4.25. Pareto fronts comparison at different $k$, $N_t = 4$, $\rho_s = 75\,kg/m^3$ and $E_s = 0.4\,GPa$

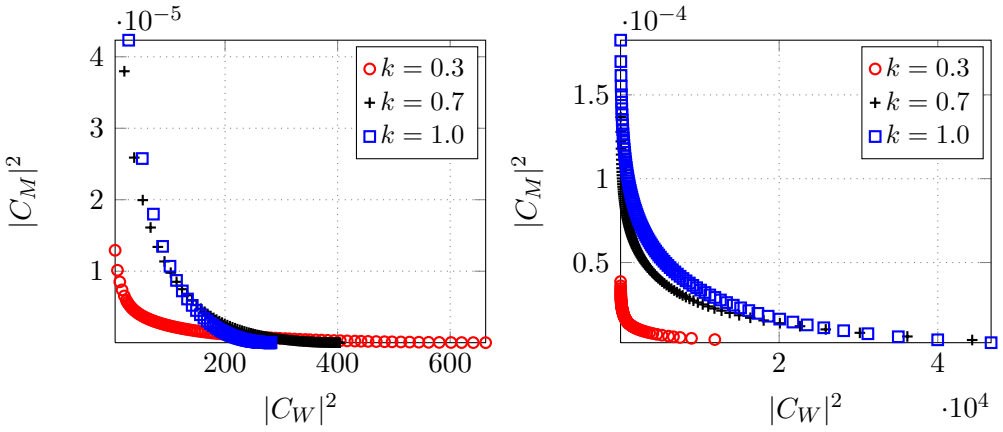


(A) $\rho_s = 75\,kg/m^3$, $E_s = 0.1\,GPa$ (B) $\rho_s = 600\,kg/m^3$, $E_s = 0.8\,GPa$

FIGURE 4.26. Pareto fronts comparison at different $k$, $N_t = 4$

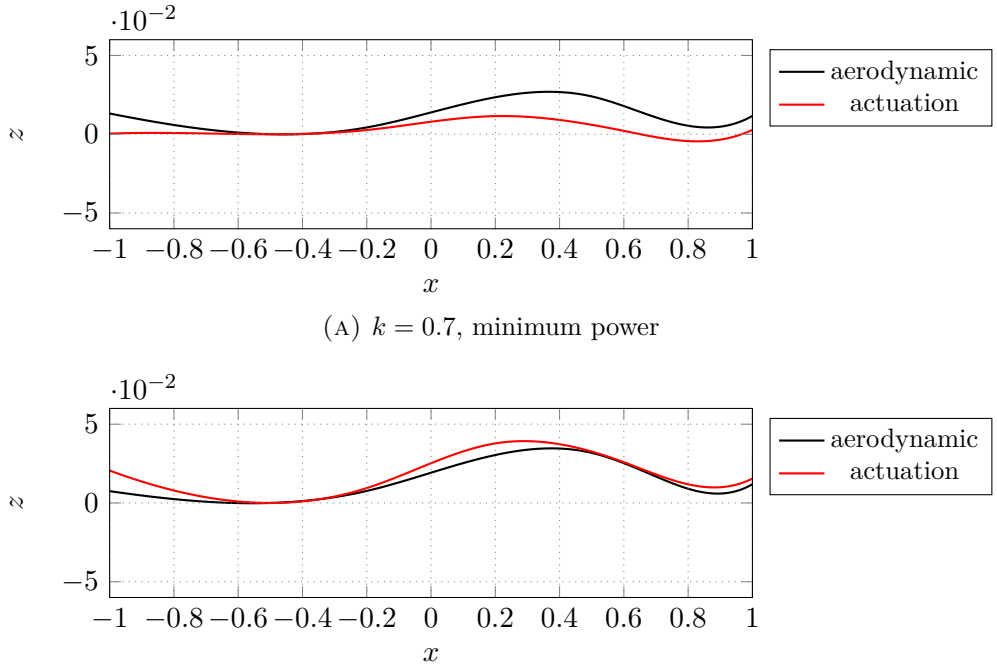


(A) $k = 0.7$, minimum power

(B) $k = 0.7$, minimum moment

FIGURE 4.27. Comparison between the aerodynamic power optimization solutions and the actuation power optimization solutions

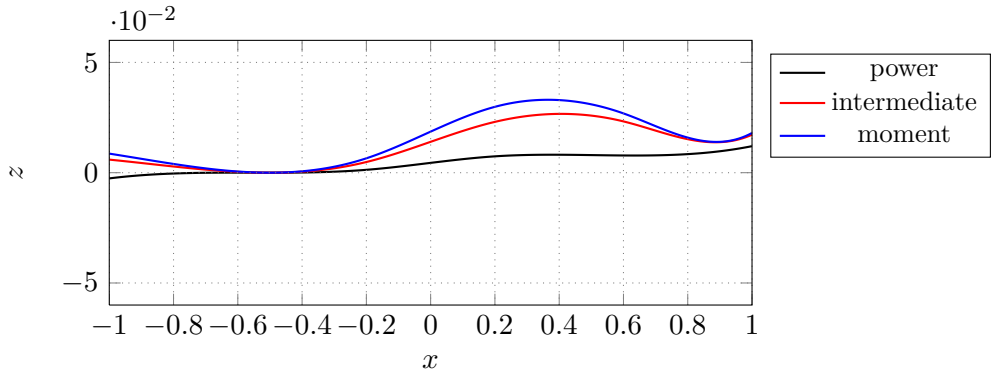


(A) $k = 0.3$

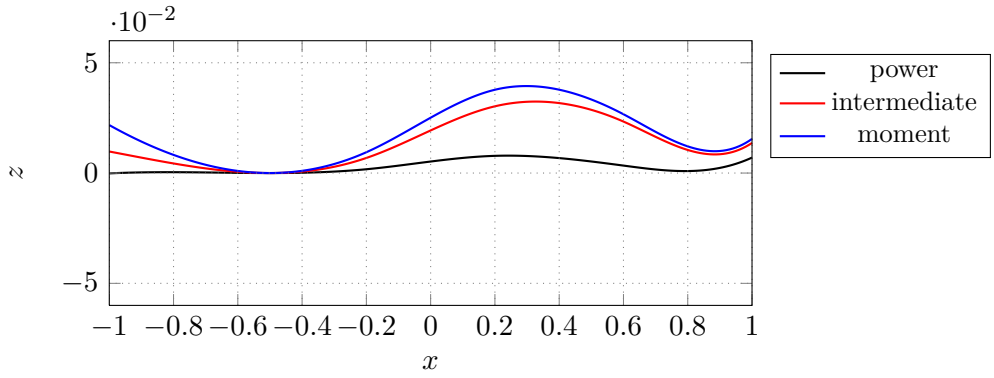


(B) $k = 0.7$

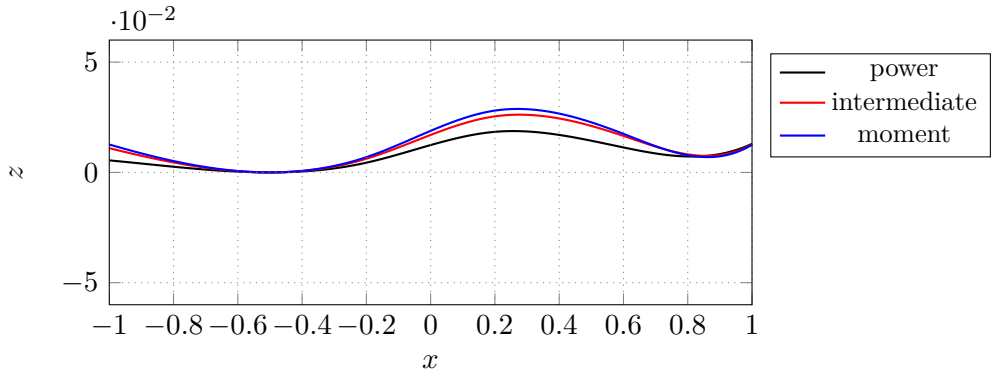


(C) $k = 1.0$

FIGURE 4.28. Optimal solutions comparison at different $k$, $N_t = 4$, $\rho_s = 300\,kg/m^3$ and $E_s = 0.1\,GPa$

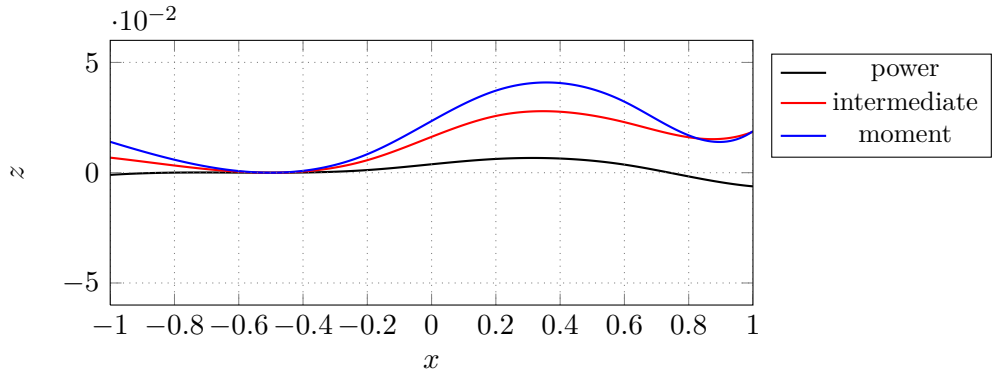


(A) $k = 0.3$

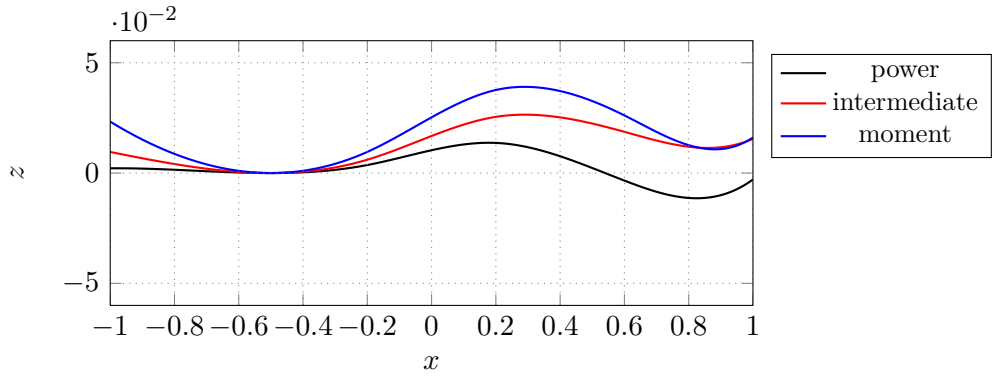


(B) $k = 0.7$

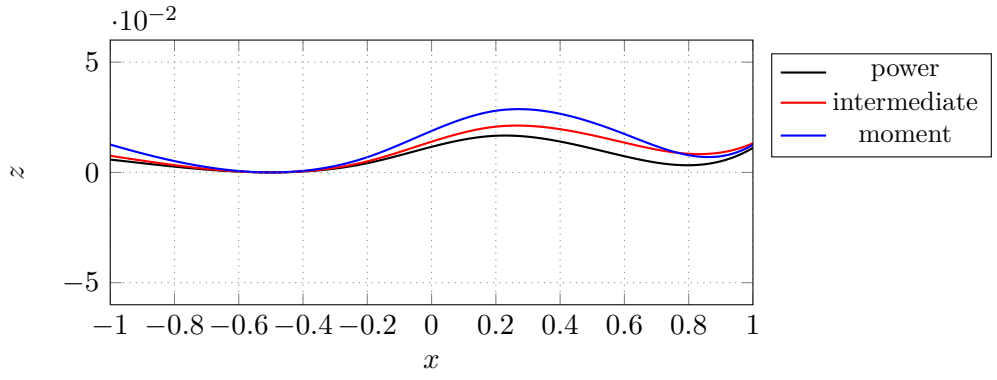


(C) $k = 1.0$

FIGURE 4.29. Optimal solutions comparison at different $k$, $N_t = 4$, $\rho_s = 75\,kg/m^3$ and $E_s = 0.4\,GPa$

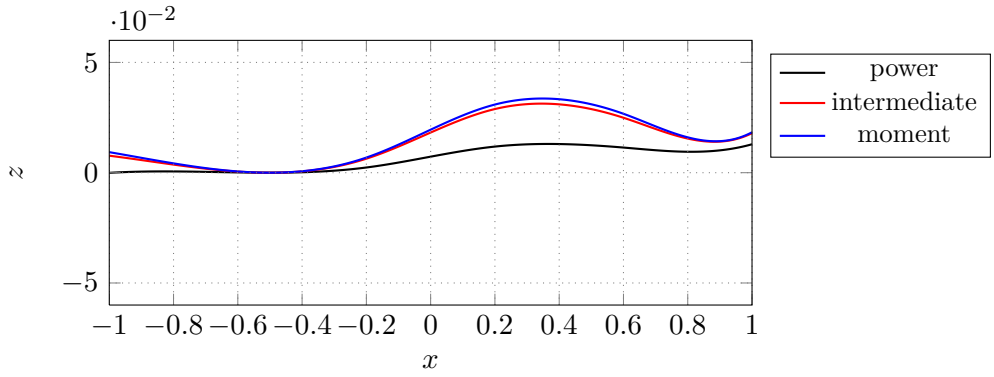


(A) $k = 0.3$

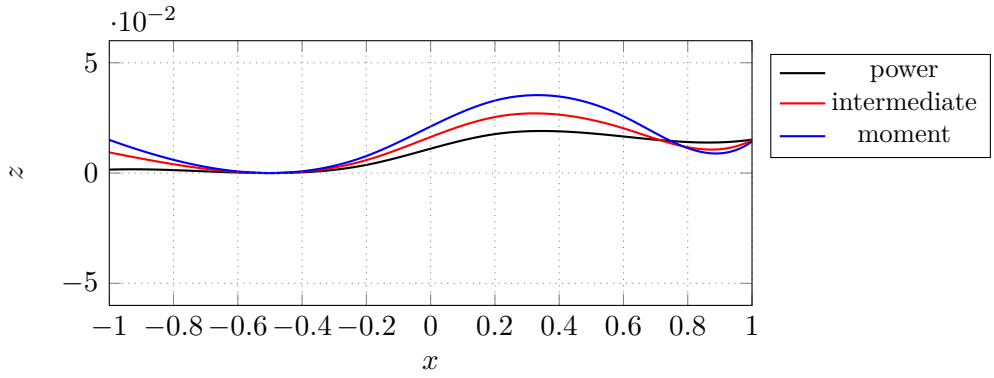


(B) $k = 0.7$

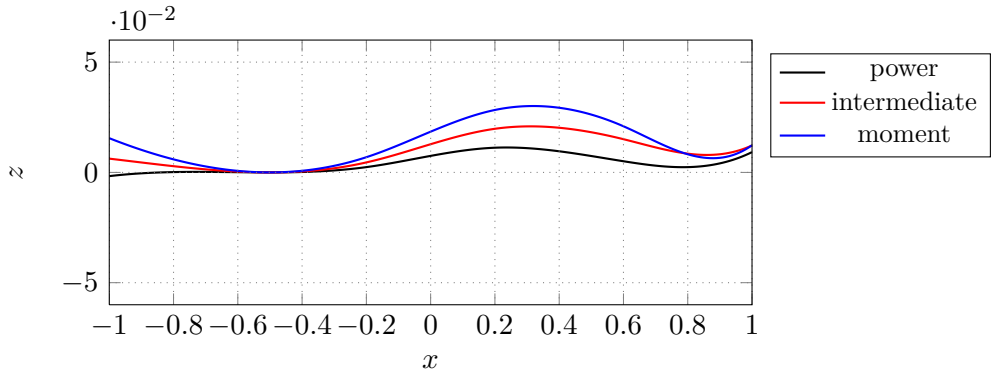


(C) $k = 1.0$

FIGURE 4.30. Optimal solutions comparison at different $k$, $N_t = 4$, $\rho_s = 75\,kg/m^3$ and $E_s = 0.1\,GPa$

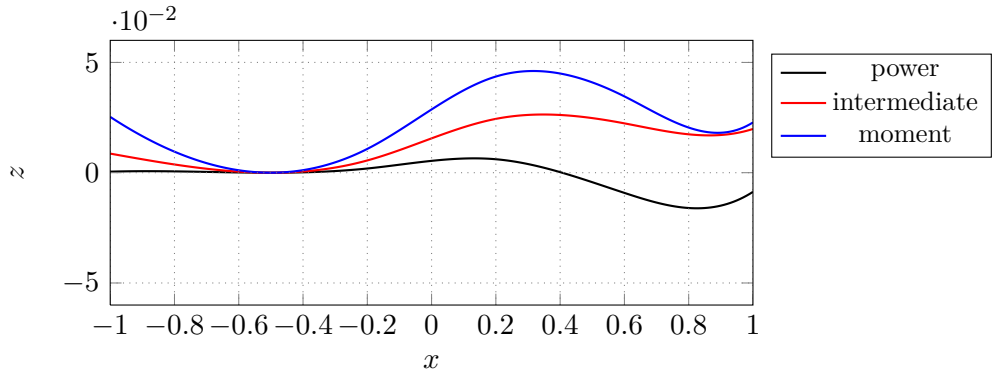


(A) $k = 0.3$

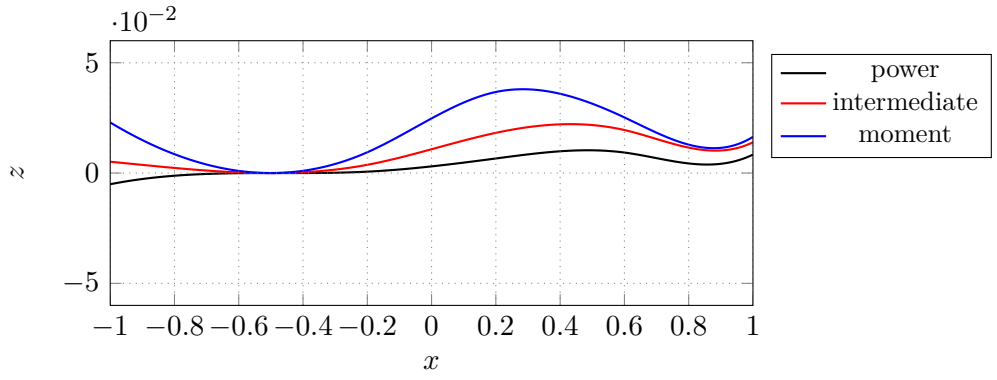


(B) $k = 0.7$

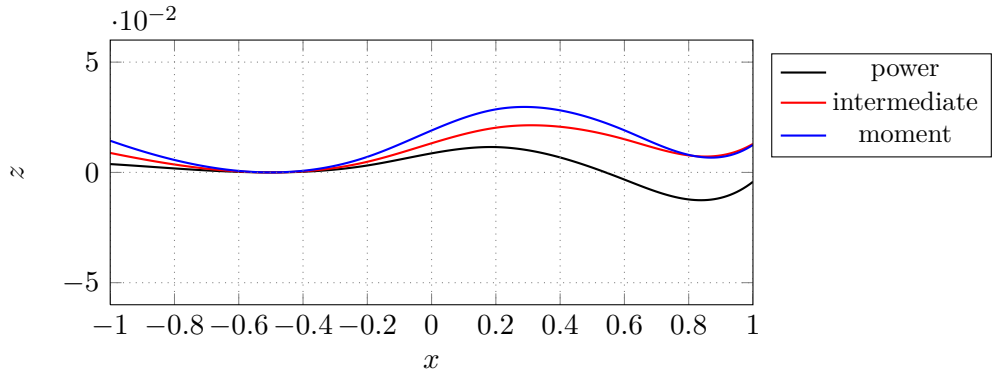


(C) $k = 1.0$

FIGURE 4.31. Optimal solutions comparison at different $k$, $N_t = 4$, $\rho_s = 600\,kg/m^3$ and $E_s = 0.8\,GPa$

# CHAPTER 5
# CONCLUSIONS

In this thesis work the problem of an unsteady aerodynamic multi-objective airfoil optimization has been studied, specifically for harmonic movements, using simple aerodynamic and structural models.

In particular, Küssner and Schwarz unsteady thin-airfoil theory was used to compute the pressure difference distribution, the aerodynamic actions and the aerodynamic power for an airfoil with multiple serially-hinged flaps and a morphing airfoil whose camberline deformation appearance is described by a cubic spline.

The airfoil was structurally treated as an Euler-Bernoulli beam. A Ritz-Galerkin approach combined with hermitian finite elements shape functions was used to compute mass and stiffness matrices used to evaluate the inertial and elastic power contributions. For the sake of simplicity, mass and stiffness distributions were considered proportional respectively to the airfoil thickness and its cube. An interface between the aerodynamic and the structural descriptions of the mean-line displacements was then built, only for the case of the cubic spline motion.

To perform the optimizations, both a gradient-based method (SQP) and an evolutionary algorithm (GA) were used. For the multiple objectives optimizations GA was used directly in its multi-objective version, while a weighted-sum scalarization approach was adopted in order to employ SQP algorithm. As expected, SQP showed better precision and constraint satisfaction, while GA was able to give a broader representation of the Pareto front, hence a more global point of view on the non-dominated solutions, especially for bigger problems.

One objective of the optimizations was to minimize the quarter-chord

oscillatory aerodynamic moment, in order to reduce the vibratory torsional load, while developing an oscillatory lift value imposed as a constraint. Then a second objective has been added, that is the minimization of the actuation power needed to perform the deformation of the morphing airfoil. Optimal shape oscillations have been computed for different reduced frequencies and various structural properties. Generally speaking, optimal shapes consist in a three cambers mean-line deformation, whose particular shapes and amplitude depend on the parameters $k$, $\frac{E_s}{\rho U^2}$ and $\frac{\rho_s}{\rho}$ and on the position of the solution on the Pareto front.

## 5.1 Future developments

Since the aim of this work was only to introduce the problem of an unsteady harmonic aerodynamic optimization, a lot of further steps can be made to improve the optimization process. They can be divided mainly in two categories:

1. Using the same physical models to introduce new elements in the problem description

2. Using more accurate models

The first sentence means that Küssner and Schwarz theory can be used to add new elements in the description of the aerodynamics of an airfoil of a morphing blade, exploiting the superposition of the effects. Fore example the effects of a sinusoidal gust can be computed (see [9], chapter 13) in order to simulate the presence of the induced velocity, or an harmonic perturbation of the asymptotic air speed $U$ can be exploited to consider forward flight with small advance ratios. In this way the optimization technique could also be adopted to solve control problems, *e.g.* minimizing the aerodynamic moment and the actuation power, with a constraint on the lift (also null), while the airfoil is subject to air speed and induced velocity perturbations. Compressibility effects can be introduced by scaling the incompressible solution with the Prandtl-Glauert transformation, if the Mach number is not too high, *i.e.* far from transonic conditions.

When facing the problem of the optimization of a real blade, is important, as suggested in the introduction, to take into account its aeroelastic behaviour, and to analyze the speed at which camber-flutter may occur (see [16]). Aeroelasticity can also be usefully taken into account during the optimization process by introducing some structural parameters (for instance the mass and bending stiffness distributions) as optimization variables, hence

both aerodynamic and structural-dynamic behaviour are contemporaneously optimized, taking in consideration their interaction.

It is also possible to introduce a method to consider the phase of the aerodynamic actions during the optimization, to have an additional control on the process, useful if aeroelastic effects are going to be investigated.

The second way is about using more accurate models to describe the aerodynamic and the elasto-mechanic behaviour of the airfoil. The aerodynamics description can be improved using for example an unsteady panel method, even considering the effects of compressibility, maybe with the addition of a flow separation prediction. Computational Fluid Dynamics (CFD) it is another possibility for the evaluation of the aerodynamic quantities needed for the optimization, but maybe is too heavy and would lead to very time-consuming computations. However, it is certainly suitable for *a posteriori* tests for the optimal solutions computed with simpler and lighter models. Inviscid tests may be carried out solving Euler equations, especially to check the effects of compressibility on solutions computed with Prandtl-Glauert transformation and relatively high Mach numbers.

while viscous tests to verify the absence of separations can be performed with Reynolds-averaged Navier-Stokes equations (RANS) with an appropriate turbulence model.

The last step could consist in applying the knowledge acquired from the previous analysis to arrange the optimization of an entire blade.

APPENDIX A

# KÜSSNER AND SCHWARZ INTEGRALS COMPUTATION

In this Appendix are reported the steps to compute all of the integrals required to obtain the solutions for Küssner and Schwarz theory in Chapter 1.

## A.1 Integrals on the whole airfoil

Let us start with a simple integral

$$\int_0^\pi \cos n\theta \, d\theta = \begin{cases} \pi & \text{if } n = 0 \\ 0 & \text{otherwise} \end{cases} \tag{A.1}$$

The previous integral can be seen as a sub-case of a useful more general integral, widely used in the work and in some of the following integrals. Prosthaphaeresis formulae are extensively utilized in this Appendix.

$$\begin{aligned} &\int_0^\pi \cos n\theta \cos m\theta \, d\theta = \frac{1}{2}\int_0^\pi \Big(\cos(n+m)\theta + \cos(n-m)\theta\Big)\, d\theta = \\ &= \frac{1}{2}\left[\frac{\sin(n+m)\theta}{n+m} + \frac{\sin(n-m)\theta}{n-m}\right]_0^\pi = \begin{cases} \pi & \text{if } n, m = 0 \\ \frac{\pi}{2} & \text{if } n = m \neq 0 \\ 0 & \text{otheriwse} \end{cases} \end{aligned} \tag{A.2}$$

The following integral is an example of one that can be computed exploiting the previous

$$\int_0^\pi \cos n\theta \cos\theta \cos 2\theta \, d\theta =$$
$$= \frac{1}{2}\int_0^\pi \cos 3\theta \cos n\theta \, d\theta + \frac{1}{2}\int_0^\pi \cos\theta \cos n\theta \, d\theta = \begin{cases} \frac{\pi}{4} & \text{if } n = 0 \\ \frac{\pi}{4} & \text{if } n = 3 \\ 0 & \text{otherwise} \end{cases} \tag{A.3}$$

Other integrals encountered during the computation of the upwash coefficients are

$$\int_0^\pi \cos n\theta \cos^2\theta \, d\theta = \int_0^\pi \cos n\theta \frac{1+\cos 2\theta}{2} \, d\theta =$$
$$= \frac{1}{2}\int_0^\pi \cos n\theta \, d\theta + \frac{1}{2}\int_0^\pi \cos n\theta \cos 2\theta \, d\theta = \begin{cases} \frac{\pi}{2} & \text{if } n = 0 \\ \frac{\pi}{4} & \text{if } n = 2 \\ 0 & \text{otherwise} \end{cases} \tag{A.4}$$

Using A.2 and A.3 one can compute

$$\int_0^\pi \cos n\theta \cos^3\theta \, d\theta = \int_0^\pi \cos n\theta \cos\theta \frac{1+\cos 2\theta}{2} \, d\theta =$$
$$= \frac{1}{2}\int_0^\pi \Big(\cos n\theta \cos\theta + \cos n\theta \cos\theta \cos 2\theta\Big) \, d\theta = \begin{cases} \frac{3}{8}\pi & \text{if } n = 1 \\ \frac{\pi}{8} & \text{if } n = 3 \\ 0 & \text{otherwise} \end{cases} \tag{A.5}$$

Other integrals arise in the computation of the aerodynamic forces and power, where also sinusoidal functions are involved. Let us begin by calculating the more general, useful in other situations

$$\int_0^\pi \sin n\theta \sin m\theta \, d\theta = \frac{1}{2}\int_0^\pi \Big(\cos(n-m)\theta - \cos(n+m)\theta\Big) \, d\theta =$$
$$= \frac{1}{2}\left[\frac{\sin(n-m)\theta}{n-m} - \frac{\sin(n+m)\theta}{n+m}\right]_0^\pi = \begin{cases} 0 & \text{if } n, m = 0 \\ \frac{\pi}{2} & \text{if } n = m \neq 0 \\ 0 & \text{if } n \neq m \end{cases} \tag{A.6}$$

Others are

$$\int_0^\pi \sin n\theta \sin\theta \cos\theta \, d\theta = \frac{1}{2}\int_0^\pi \sin n\theta \sin 2\theta \, d\theta = \begin{cases} \frac{\pi}{4} & \text{if } n = 2 \\ 0 & \text{otherwise} \end{cases} \tag{A.7}$$

$$\int_0^\pi \sin n\theta \sin\theta \cos^2\theta \, d\theta = \frac{1}{2}\int_0^\pi \sin n\theta \sin 2\theta \cos\theta \, d\theta =$$
$$= \frac{1}{4}\int_0^\pi \sin n\theta \Big(\sin 3\theta + \sin\theta\Big) \, d\theta = \begin{cases} \frac{\pi}{8} & \text{if } n = 1 \\ \frac{\pi}{8} & \text{if } n = 3 \\ 0 & \text{otherwise} \end{cases} \tag{A.8}$$

$$\int_0^\pi \sin n\theta \sin\theta \cos^3\theta \, d\theta = \frac{1}{2}\int_0^\pi \sin n\theta \sin 2\theta \cos^2\theta \, d\theta =$$
$$= \frac{1}{4}\int_0^\pi \sin n\theta \sin 2\theta \Big(1 + \cos 2\theta\Big) \, d\theta =$$
$$= \frac{1}{4}\int_0^\pi \sin n\theta \sin 2\theta \, d\theta + \frac{1}{8}\int_0^\pi \sin n\theta \sin 4\theta \, d\theta =$$
$$= \begin{cases} \frac{\pi}{8} & \text{if } n = 2 \\ \frac{\pi}{16} & \text{if } n = 4 \\ 0 & \text{otherwise} \end{cases} \tag{A.9}$$

There are also integrals involving a tangent, which need half-angle formulae to be solved

$$\int_0^\pi \tan\frac{\theta}{2} \sin\theta \, d\theta = \int_0^\pi \frac{1 - \cos\theta}{\sin\theta} \sin\theta \, d\theta =$$
$$= \Big[\theta - \sin\theta\Big]_0^\pi = \pi \tag{A.10}$$

$$\int_0^\pi \tan\frac{\theta}{2} \sin\theta \cos\theta \, d\theta = \int_0^\pi (1 - \cos\theta)\cos\theta \, d\theta =$$
$$= \int_0^\pi (\cos\theta - \cos^2\theta) \, d\theta = -\frac{1}{2}\int_0^\pi (1 + \cos 2\theta) \, d\theta = -\frac{\pi}{2} \tag{A.11}$$

$$\int_0^\pi \tan\frac{\theta}{2} \sin\theta \cos^2\theta \, d\theta = \frac{1}{2}\int_0^\pi (1 - \cos\theta)(1 + \cos 2\theta) \, d\theta =$$
$$= \frac{1}{2}\int_0^\pi (1 + \cos 2\theta) \, d\theta - \frac{1}{2}\int_0^\pi \cos\theta \, d\theta - \frac{1}{2}\int_0^\pi \cos\theta \cos 2\theta \, d\theta =$$
$$= \frac{\pi}{2} - \frac{1}{2}\int_0^\pi (\cos 3\theta + \cos\theta) \, d\theta = \frac{\pi}{2} \tag{A.12}$$

$$\begin{aligned}
&\int_0^\pi \tan\frac{\theta}{2}\sin\theta\cos^3\theta\,d\theta = \int_0^\pi (\cos^3\theta - \cos^4\theta)\,d\theta = \\
&= \frac{1}{2}\int_0^\pi (1+\cos 2\theta)\cos\theta\,d\theta - \int_0^\pi \cos^2\theta\cos^2\theta\,d\theta = \\
&= \frac{1}{2}\int_0^\pi \cos\theta\,d\theta + \frac{1}{4}\int_0^\pi (\cos 3\theta + \cos\theta)\,d\theta - \frac{1}{4}\int_0^\pi (1+\cos 2\theta)^2\,d\theta = \\
&= -\frac{1}{4}\int_0^\pi (1 + 2\cos 2\theta + \cos^2 2\theta)\,d\theta = -\frac{\pi}{4} - \frac{1}{8}\int_0^\pi (1+\cos 4\theta)\,d\theta = \\
&= -\frac{\pi}{4} - \frac{\pi}{8} = -\frac{3}{8}\pi
\end{aligned} \tag{A.13}$$

## A.2 Integrals on a portion of airfoil

All the previous integrals need to be computed again with a different integration domain when they are referred only on a portion of airfoil, for example when calculating the hinge moment of a flap. This can be seen as a more general case, in fact preceding results can be obtained imposing $\theta_F = \pi$.

Let us start with the integrals for the upwash coefficients:

$$\int_0^{\theta_F} \cos n\theta\,d\theta = \begin{cases} \theta_F & \text{if } n = 0 \\ \frac{\sin n\theta_F}{n} & \text{otherwise} \end{cases} \tag{A.14}$$

$$\begin{aligned}
&\int_0^{\theta_F} \cos n\theta\cos\theta\,d\theta = \frac{1}{2}\int_0^{\theta_F} \Big(\cos(n+1)\theta + \cos(n-1)\theta\Big)\,d\theta = \\
&= \frac{1}{2}\left[\frac{\sin(n+1)\theta}{n+1} + \frac{\sin(n-1)\theta}{n-1}\right]_0^{\theta_F} = \\
&= \begin{cases} \sin\theta_F & \text{if } n = 0 \\ \frac{1}{2}\Big(\theta_F + \frac{\sin 2\theta_F}{2}\Big) & \text{if } n = 1 \\ \frac{1}{2}\left[\frac{\sin(n+1)\theta_F}{n+1} + \frac{\sin(n-1)\theta_F}{n-1}\right] & \text{otherwise} \end{cases}
\end{aligned} \tag{A.15}$$

$$
\begin{aligned}
&\int_0^{\theta_F} \cos n\theta \cos^2\theta \, d\theta = \frac{1}{2}\int_0^{\theta_F} \cos n\theta (1+\cos 2\theta)\, d\theta = \\
&= \frac{1}{2}\int_0^{\theta_F} \cos n\theta \, d\theta + \frac{1}{2}\int_0^{\theta_F} \cos n\theta \cos 2\theta \, d\theta = \\
&= \frac{1}{2}\int_0^{\theta_F} \cos n\theta \, d\theta + \frac{1}{4}\int_0^{\theta_F} (\cos(n+2)\theta + \cos(n-2)\theta)\, d\theta = \\
&= \begin{cases}
\frac{\theta_F}{2} + \frac{1}{4}\sin 2\theta_F & \text{if } n = 0 \\
\frac{\sin 2\theta_F}{4} + \frac{1}{4}\left[\frac{\sin 4\theta_F}{4} + \theta_F\right] & \text{if } n = 2 \\
\frac{\sin n\theta_F}{2n} + \frac{1}{4}\left[\frac{\sin(n+2)\theta_F}{n+2} + \frac{\sin(n-2)\theta_F}{n-2}\right] & \text{otherwise}
\end{cases}
\end{aligned}
\tag{A.16}
$$

$$
\begin{aligned}
&\int_0^{\theta_F} \cos n\theta \cos^3\theta \, d\theta = \frac{1}{2}\int_0^{\theta_F} \cos n\theta \cos\theta (1+\cos 2\theta)\, d\theta = \\
&= \frac{1}{2}\int_0^{\theta_F} \Big(\cos n\theta \cos\theta + \cos n\theta \cos\theta \cos 2\theta\Big)\, d\theta = \\
&= \frac{1}{2}\int_0^{\theta_F} \cos n\theta \cos\theta \, d\theta + \frac{1}{4}\int_0^{\theta_F} \cos n\theta \cos 3\theta \, d\theta + \\
&+ \frac{1}{4}\int_0^{\theta_F} \cos n\theta \cos\theta \, d\theta = \\
&= \frac{3}{4}\int_0^{\theta_F} \cos n\theta \cos\theta \, d\theta + \frac{1}{8}\int_0^{\theta_F} \cos(n+3)\theta \, d\theta + \\
&+ \frac{1}{8}\int_0^{\theta_F} \cos(n-3)\theta \, d\theta = \\
&= \begin{cases}
\frac{3}{4}\sin\theta_F + \frac{\sin 3\theta_F}{12} & \text{if } n = 0 \\
\frac{1}{8}\Big(\frac{\sin 4\theta_F}{4} + 2\sin 2\theta_F + 3\theta_F\Big) & \text{if } n = 1 \\
\frac{3}{8}\Big(\frac{\sin 4\theta_F}{4} + \frac{\sin 2\theta_F}{2}\Big) + \frac{1}{8}\Big(\frac{\sin 6\theta_F}{6} + \theta_f\Big) & \text{if } n = 3 \\
\frac{3}{8}\Big(\frac{\sin(n+1)\theta_F}{n+1} + \frac{\sin(n-1)\theta_F}{n-1}\Big) + \frac{1}{8}\Big(\frac{\sin(n+3)\theta_F}{n+3} + \frac{\sin(n-3)\theta_F}{n-3}\Big) & \text{otherwise}
\end{cases}
\end{aligned}
\tag{A.17}
$$

Now the integrals involving also a sine:

$$
\begin{aligned}
&\int_0^{\theta_F} \sin n\theta \sin\theta \, d\theta = \frac{1}{2}\int_0^{\theta_F} \Big(\cos(n-1)\theta - \cos(n+1)\theta\Big)\, d\theta = \\
&= \frac{1}{2}\left[\frac{\sin(n-1)\theta}{n-1} - \frac{\sin(n+1)\theta}{n+1}\right]_0^{\theta_F} = \\
&= \begin{cases}
0 & \text{if } n = 0 \\
\frac{1}{2}\Big(\theta_F - \frac{\sin 2\theta_F}{2}\Big) & \text{if } n = 1 \\
\frac{1}{2}\Big(\frac{\sin(n-1)\theta_F}{n-1} - \frac{\sin(n+1)\theta_F}{n+1}\Big) & \text{otherwise}
\end{cases}
\end{aligned}
\tag{A.18}
$$

$$\int_0^{\theta_F} \sin n\theta \sin\theta \cos\theta \, d\theta = \frac{1}{2}\int_0^{\theta_F} \sin n\theta \sin 2\theta \, d\theta =$$
$$\frac{1}{4}\int_0^{\theta_F} \Big(\cos(n-2)\theta - \cos(n+2)\theta\Big) \, d\theta =$$
$$= \begin{cases} 0 & \text{if } n = 0 \\ \frac{1}{4}\Big(\theta_F - \frac{\sin 4\theta_F}{4}\Big) & \text{if } n = 2 \\ \frac{1}{4}\Big(\frac{\sin(n-2)\theta_F}{n-2} - \frac{\sin(n+2)\theta_F}{n+2}\Big) & \text{otherwise} \end{cases} \tag{A.19}$$

$$\int_0^{\theta_F} \sin n\theta \sin\theta \cos^2\theta \, d\theta = \frac{1}{2}\int_0^{\theta_F} \sin n\theta \sin 2\theta \cos\theta \, d\theta =$$
$$\frac{1}{4}\int_0^{\theta_F} \sin n\theta\Big(\sin 3\theta - \sin\theta\Big) \, d\theta =$$
$$= \frac{1}{8}\int_0^{\theta_F} \Big(\cos(n-3)\theta - \cos(n+3)\theta\Big) \, d\theta + \frac{1}{4}\int_0^{\theta_F} \sin n\theta \sin\theta \, d\theta =$$
$$= \begin{cases} 0 & \text{if } n = 0 \\ \frac{1}{8}\Big(\theta_F - \frac{\sin 2\theta_F}{2}\Big) + \frac{1}{8}\Big(\frac{\sin 2\theta_F}{2} - \frac{\sin 4\theta_F}{4}\Big) & \text{if } n = 1 \\ \frac{1}{8}\Big(\theta_F - \frac{\sin 6\theta_F}{6}\Big) + \frac{1}{8}\Big(\frac{\sin 2\theta_F}{2} - \frac{\sin 4\theta_F}{4}\Big) & \text{if } n = 3 \\ \frac{1}{8}\Big(\frac{\sin(n-3)\theta_F}{n-3} - \frac{\sin(n+3)\theta_F}{n+3}\Big) + \frac{1}{8}\Big(\frac{\sin(n-1)\theta_F}{n-1} - \frac{\sin(n+1)\theta_F}{n+1}\Big) & \text{otherwise} \end{cases} \tag{A.20}$$

$$\int_0^{\theta_F} \sin n\theta \sin\theta \cos^3\theta \, d\theta = \frac{1}{2}\int_0^{\theta_F} \sin n\theta \sin 2\theta \cos^2\theta \, d\theta =$$
$$\frac{1}{4}\int_0^{\theta_F} \sin n\theta \sin 2\theta \, d\theta + \frac{1}{4}\int_0^{\theta_F} \sin n\theta \sin 2\theta \cos 2\theta \, d\theta =$$
$$= \frac{1}{8}\int_0^{\theta_F} \Big(\cos(n-2)\theta - \cos(n+2)\theta\Big) \, d\theta + \frac{1}{8}\int_0^{\theta_F} \sin n\theta \sin 4\theta \, d\theta =$$
$$= \frac{1}{8}\int_0^{\theta_F} \Big(\cos(n-2)\theta - \cos(n+2)\theta\Big) \, d\theta +$$
$$+ \frac{1}{16}\int_0^{\theta_F} \Big(\cos(n-4)\theta - \cos(n+4)\theta\Big) \, d\theta =$$
$$= \begin{cases} 0 & \text{if } n = 0 \\ \frac{1}{8}\Big(\theta_F - \frac{\sin 4\theta_F}{4}\Big) + \frac{1}{16}\Big(\frac{\sin 2\theta_F}{2} - \frac{\sin 6\theta_F}{6}\Big) & \text{if } n = 2 \\ \frac{1}{16}\Big(\theta_F - \frac{\sin 8\theta_F}{8}\Big) + \frac{1}{8}\Big(\frac{\sin 2\theta_F}{2} - \frac{\sin 6\theta_F}{6}\Big) & \text{if } n = 4 \\ \frac{1}{16}\Big(\frac{\sin(n-4)\theta_F}{n-4} - \frac{\sin(n+4)\theta_F}{n+4}\Big) + \frac{1}{8}\Big(\frac{\sin(n-2)\theta_F}{n-2} - \frac{\sin(n+2)\theta_F}{n+2}\Big) & \text{otherwise} \end{cases} \tag{A.21}$$

Lastly it is necessary to compute the integrals with a tangent

$$\int_0^{\theta_F} \tan\frac{\theta}{2}\sin\theta\,d\theta = \int_0^{\theta_F} \frac{1-\cos\theta}{\sin\theta}\sin\theta\,d\theta =$$
$$= \Big[\theta - \sin\theta\Big]_0^{\theta_F} = \theta_F - \sin\theta_F \tag{A.22}$$

$$\int_0^{\theta_F} \tan\frac{\theta}{2}\sin\theta\cos\theta\,d\theta = \int_0^{\theta_F} (1-\cos\theta)\cos\theta\,d\theta =$$
$$= \int_0^{\theta_F} (\cos\theta - \cos^2\theta)\,d\theta = \frac{1}{2}\int_0^{\theta_F} (2\cos\theta - 1 - \cos 2\theta)\,d\theta =$$
$$= \sin\theta_F - \frac{\theta_F}{2} - \frac{\sin 2\theta_F}{4} \tag{A.23}$$

$$\int_0^{\theta_F} \tan\frac{\theta}{2}\sin\theta\cos^2\theta\,d\theta = \int_0^{\theta_F} (1-\cos\theta)\cos^2\theta\,d\theta =$$
$$= \int_0^{\theta_F} (\cos^2\theta - \cos^3\theta)\,d\theta =$$
$$= \frac{1}{2}\int_0^{\theta_F} (1+\cos 2\theta)\,d\theta - \frac{1}{2}\int_0^{\theta_F} (\cos\theta + \cos\theta\cos 2\theta)\,d\theta =$$
$$= \frac{\theta_F}{2} + \frac{\sin 2\theta_F}{4} - \frac{\sin\theta_F}{2} - \frac{1}{4}\int_0^{\theta_F} (\cos 3\theta + \cos\theta)\,d\theta =$$
$$= \frac{\theta_F}{2} - \frac{3\sin\theta_F}{4} + \frac{\sin 2\theta_F}{4} - \frac{\sin 3\theta_F}{12} \tag{A.24}$$

$$\int_0^{\theta_F} \tan\frac{\theta}{2}\sin\theta\cos^3\theta\,d\theta = \int_0^{\theta_F} (1-\cos\theta)\cos^3\theta\,d\theta =$$
$$= \int_0^{\theta_F} (\cos^3\theta - \cos^4\theta)\,d\theta =$$
$$= \frac{1}{2}\int_0^{\theta_F} (1+\cos 2\theta)\cos\theta\,d\theta - \frac{1}{4}\int_0^{\theta_F} (1+\cos 2\theta)^2\,d\theta =$$
$$= \frac{1}{2}\int_0^{\theta_F} \cos\theta\,d\theta + \frac{1}{4}\int_0^{\theta_F} (\cos 3\theta + \cos\theta)\,d\theta +$$
$$- \frac{1}{4}\int_0^{\theta_F} (1 + 2\cos 2\theta + \cos^2 2\theta) =$$
$$= \frac{\sin\theta_F}{2} + \frac{1}{4}\left(\frac{\sin 3\theta_F}{3} + \sin\theta_F\right) +$$
$$- \frac{1}{4}\int_0^{\theta_F} (1 + 2\cos 2\theta) - \frac{1}{8}\int_0^{\theta_F} (1+\cos 4\theta) =$$
$$= -\frac{3\theta_F}{8} + \frac{3\sin\theta_F}{4} - \frac{\sin 2\theta_F}{4} + \frac{\sin 3\theta_F}{12} - \frac{\sin 4\theta_F}{32} \tag{A.25}$$

# APPENDIX B
# THEODORSEN COEFFICIENTS

In this Appendix the functions and the geometric constants defined for convenience's sake by Theodorsen in his works ([22] and [23]) and used in Chapter 1 are reported, neglecting the terms multiplied by $l$ and $m$, since they are null, because in this work aerodinamically balanced flaps are not considered, as they are not able to represent the deformation of a morphing blade.

Functions for the computation of the lift

$$A_{ch} = -1 - \frac{2G}{k} + j\frac{2F}{k} \tag{B.1}$$

$$\begin{aligned} A_{c\alpha} =& a - \left(\frac{1}{2} - a\right)\frac{2G}{k} + \frac{2F}{k^2} + \\ &+ j\frac{1}{k}\left(1 + \frac{2G}{k} + \left(\frac{1}{2} - a\right)2F\right) \end{aligned} \tag{B.2}$$

$$\begin{aligned} A_{c\beta} =& \frac{T_1}{\pi} - T_{11}\frac{2G}{2\pi k} + T_{10}\frac{2F}{\pi k^2} + \\ &+ j\frac{1}{k}\left(-\frac{T_4}{\pi} + T_{10}\frac{2G}{\pi k} + T_{11}\frac{2F}{2\pi}\right) \end{aligned} \tag{B.3}$$

$$\begin{aligned} A_{c\gamma} =& \frac{T_1^d}{\pi} - T_{11}^d\frac{2G}{2\pi k} + T_{10}^d\frac{2F}{\pi k^2} + \\ &+ j\frac{1}{k}\left(-\frac{T_4^d}{\pi} + T_{10}^d\frac{2G}{\pi k} + T_{11}^d\frac{2F}{2\pi}\right) \end{aligned} \tag{B.4}$$

Functions for the computation of the moment referred to the rotation point

$$A_{ah} = a + \left(\frac{1}{2} + a\right)\frac{2G}{k} + j\frac{1}{k}\left(-\left(\frac{1}{2} + a\right)2F\right) \tag{B.5}$$

$$\begin{aligned} A_{a\alpha} = &- \left(\frac{1}{8} + a^2\right) + \left(\frac{1}{4} - a^2\right)\frac{2G}{k} - \left(\frac{1}{2} + a\right)\frac{2F}{k^2} + \\ &+ j\frac{1}{k}\left(\left(\frac{1}{2} - a\right) - \left(\frac{1}{2} + a\right)\frac{2G}{k} - \left(\frac{1}{4} - a^2\right)2F\right) \end{aligned} \tag{B.6}$$

$$\begin{aligned} A_{a\beta} = &- \frac{2T_{13}}{\pi} + \frac{T_{15}}{\pi k^2} + \left(\frac{1}{2} + a\right)\left(T_{11}\frac{2G}{2\pi k} - T_{10}\frac{2F}{\pi k^2}\right) + \\ &+ j\frac{1}{k}\left(\frac{T_{16}}{\pi} - \left(\frac{1}{2} + a\right)\left(T_{10}\frac{2G}{\pi k} + T_{11}\frac{F}{\pi}\right)\right) \end{aligned} \tag{B.7}$$

$$\begin{aligned} A_{a\gamma} = &- \frac{2T^d_{13}}{\pi} + \frac{T^d_{15}}{\pi k^2} + \left(\frac{1}{2} + a\right)\left(T^d_{11}\frac{2G}{2\pi k} - T^d_{10}\frac{2F}{\pi k^2}\right) + \\ &+ j\frac{1}{k}\left(\frac{T^d_{16}}{\pi} - \left(\frac{1}{2} + a\right)\left(T^d_{10}\frac{2G}{\pi k} + T^d_{11}\frac{F}{\pi}\right)\right) \end{aligned} \tag{B.8}$$

Functions for the computation of the first hinge moment

$$A_{bh} = \frac{T_1}{\pi} - T_{12}\frac{2G}{2\pi k} + jT_{12}\frac{2F}{2\pi k} \tag{B.9}$$

$$\begin{aligned} A_{ba} = &- \frac{2T_{13}}{\pi} - \frac{T_{12}}{2\pi}\left(\left(\frac{1}{2} - a\right)\frac{2G}{k} - \frac{2F}{k^2}\right) + \\ &+ j\frac{1}{k}\left(\frac{T_{17}}{pi} + \frac{T_{12}}{2\pi}\left(\frac{2G}{k} + \left(\frac{1}{2} - a\right)2F\right)\right) \end{aligned} \tag{B.10}$$

$$\begin{aligned} A_{bb} = &\frac{T_3}{\pi^2} + \frac{T_{18}}{k^2\pi^2} - \frac{T_{12}}{2\pi}\left(T_{11}\frac{2G}{2\pi k} - T_{10}\frac{2F}{\pi k^2}\right) + \\ &+ j\frac{1}{k}\left(\frac{T_{19}}{pi^2} + \frac{T_{12}}{2\pi}\left(T_{10}\frac{2G}{\pi k} + T_{11}\frac{2F}{2\pi}\right)\right) \end{aligned} \tag{B.11}$$

$$A_{bd} = \frac{Y_6}{\pi^2} + \frac{Y_9}{\pi^2 k^2} - \frac{T_{12}}{2\pi}\left(T_{11}^d \frac{2G}{2\pi k} - T_{10}^d \frac{2F}{\pi k^2}\right) + \\ + j\frac{1}{k}\left(\frac{Y_{10}}{\pi^2} + \frac{T_{12}}{2\pi}\left(T_{10}^d \frac{2G}{\pi k} + T_{11}^d \frac{2F}{2\pi}\right)\right) \tag{B.12}$$

Functions for the computation of the second hinge moment

$$A_{dh} = \frac{T_1^d}{\pi} - T_{12}^d \frac{2G}{2\pi k} + jT_{12}^d \frac{2F}{2\pi k} \tag{B.13}$$

$$A_{da} = -\frac{2T_{13}^d}{\pi} - \frac{T_{12}^d}{2\pi}\left(\left(\frac{1}{2} - a\right)\frac{2G}{k} - \frac{2F}{k^2}\right) + \\ + j\frac{1}{k}\left(\frac{T_{17}^d}{pi} + \frac{T_{12}^d}{2\pi}\left(\frac{2G}{k} + \left(\frac{1}{2} - a\right)2F\right)\right) \tag{B.14}$$

$$A_{db} = \frac{Y_6}{\pi^2} + \frac{Y_1 7}{\pi^2 k^2} - \frac{T_{12}^d}{2\pi}\left(T_{11}\frac{2G}{2\pi k} - T_{10}\frac{2F}{\pi k^2}\right) + \\ + j\frac{1}{k}\left(\frac{Y_{18}}{\pi^2} + \frac{T_{12}^d}{2\pi}\left(T_{10}\frac{2G}{\pi k} + T_{11}\frac{2F}{2\pi}\right)\right) \tag{B.15}$$

$$A_{dd} = \frac{T_3^d}{\pi^2} + \frac{T_{18}^d}{k^2\pi^2} - \frac{T_{12}^d}{2\pi}\left(T_{11}^d \frac{2G}{2\pi k} - T_{10}^d \frac{2F}{\pi k^2}\right) + \\ + j\frac{1}{k}\left(\frac{T_{19}^d}{pi^2} + \frac{T_{12}^d}{2\pi}\left(T_{10}^d \frac{2G}{\pi k} + T_{11}^d \frac{2F}{2\pi}\right)\right) \tag{B.16}$$

The $T$ terms are functions of $c$ and $d$ only. When no explicit mention is made, they are ment to be function of $c$, otherwise they are labeled with a $d$ (i.e. $T_{\dots}^{\mathrm{d}}$), and it is only necessary to replace the $c$ with a $d$ in the following constants.

$$T_0 = c\sqrt{1-c^2}\theta_F - (1-c^2)$$
$$T_1 = -\frac{1}{3}(2+c^2)\sqrt{1-c^2} + c\theta_F$$
$$T_2 = c(1-c^2) - (1+c^2)\sqrt{1-c^2}\theta_F + c\theta_F^2$$
$$T_3 = -\frac{1}{8}(1-c^2)(5c^2+4) + \frac{1}{4}c(7+2c^2)\sqrt{1-c^2}\theta_F - \left(\frac{1}{8} + c^2\right)\theta_F^2$$
$$T_4 = c\sqrt{1-c^2} - \theta_F$$

$$T_5 = -(1-c^2) + 2c\sqrt{1-c^2}\theta_F - \theta_F^2$$
$$T_6 = T_2$$
$$T_7 = \frac{1}{8}c(7+2c^2)\sqrt{1-c^2} - \left(\frac{1}{8}+c^2\right)\theta_F$$
$$T_8 = -\frac{1}{3}(1-c^2)^{3/2} - cT_4$$
$$T_9 = \frac{1}{2}\left[\frac{1}{3}(1-c^2)^{3/2} + aT_4\right]$$

$$T_{10} = \sqrt{1-c^2} + \theta_F$$
$$T_{11} = (2-c)\sqrt{1-c^2} + (1-2c)\theta_F$$
$$T_{12} = (2+c)\sqrt{1-c^2} - (1+2c)\theta_F$$

$$T_{13} = -\frac{1}{2}(T_7 + (c-a)T_1)$$
$$T_{15} = T_4 + T_{10}$$
$$T_{16} = T_1 - T_8 - (c-a)T_4 + \frac{1}{2}T_{11}$$
$$T_{17} = -2T_9 - T_1 + \left(a - \frac{1}{2}\right)T_4$$
$$T_{18} = T_5 - T_4T_{10}$$
$$T_{19} = -\frac{1}{2}T_4T_{11}$$
$$T_{21} = \sqrt{\frac{1+c}{1-c}}$$

The $Y$ terms are functions of both $c$ and $d$.

$$Y_1 = -\sqrt{1-c^2}\sqrt{1-d^2} - \theta_{F_0}\,\theta_{F_1} + d\sqrt{1-d^2}\,\theta_{F_0} + \\ + c\sqrt{1-c^2}\,\theta_{F_1} - (d-c)^2\log N$$
$$Y_2 = 2\sqrt{1-d^2}\,\theta_{F_0} - 2(d-c)\log N$$

$$Y_3 = \frac{1}{3}(c+2d)\sqrt{1-c^2}\sqrt{1-d^2} + d\,\theta_{F_0}\,\theta_{F_1} + \\ - \frac{1}{3}(2+d^2)\sqrt{1-d^2}\,\theta_{F_0} + \\ - \frac{1}{3}(1+3cd-c^2)\sqrt{1-c^2}\,\theta_{F_1} + \frac{1}{3}(d-c)^3\log N$$

$$
\begin{aligned}
Y_4 &= \frac{1}{3}(d+2c)\sqrt{1-c^2}\sqrt{1-d^2} + c\,\theta_{F_0}\,\theta_{F_1} + \\
&- \frac{1}{3}(2+c^2)\sqrt{1-c^2}\,\theta_{F_1} + \\
&- \frac{1}{3}(1+3cd-d^2)\sqrt{1-d^2}\,\theta_{F_0} - \frac{1}{3}(d-c)^3\log N
\end{aligned}
$$

$$
\begin{aligned}
Y_6 &= -\frac{1}{2}\sqrt{1-c^2}\sqrt{1-d^2}\left(1+\frac{c^2}{6}+\frac{d^2}{6}+\frac{11cd}{12}\right) - \left(\frac{1}{8}+cd\right)\theta_{F_0}\,\theta_{F_1} \\
&+ \frac{1}{3}\left[\frac{d}{4}\left(\frac{5}{2}-d^2\right)+c(2+d^2)\right]\sqrt{1-d^2}\,\theta_{F_0} + \\
&+ \frac{1}{3}\left[\frac{c}{4}\left(\frac{5}{2}-c^2\right)+d(2+c^2)\right]\sqrt{1-c^2}\,\theta_{F_1} + \\
&+ \frac{1}{12}(d-c)^4\log N
\end{aligned}
$$

$$
\begin{aligned}
Y_9 &= Y_1 - T_4 T_1^{\mathrm{d}} 0 \\
Y_{10} &= Y_3 - Y_4 - \frac{1}{2}T_4 T_{11}^{\mathrm{d}} \\
Y_{13} &= Y_2 + T_4 T_{21}^{\mathrm{d}} \\
Y_{17} &= Y_1 - T_4^{\mathrm{d}} T_{10} \\
Y_{18} &= Y_4 - Y_3 - \frac{1}{2}T_4^{\mathrm{d}} T_{11}
\end{aligned}
$$

with

$$
N(c,d) = \left|\frac{1-cd-\sqrt{1-c^2}\sqrt{1-d^2}}{d-c}\right|
$$

APPENDICE C

# ESTRATTO IN LINGUA ITALIANA

L' introduzione di nuove tecnologie per materiali di applicazione strutturale, come per esempio l'uso di materiali adattivi, apre le porte alla possibilità di realizzare un cambiamento di forma regolare di superfici aerodinamiche, grazie all' applicazione di forze di attuazione distribuite. Queste capacità *morphing* possono essere sfruttate al fine di assolvere a molteplici funzioni, sia nell'ambito di velivoli ad ala fissa, sia per velivoli ad ala rotante. Pale o ali morphing possono portare a miglioramenti di prestazioni, manovrabilità, caratteristiche aerodinamiche ed aeroelastiche, pertanto la ricerca in questo settore è attualmente molto attiva.

Il miglioramento delle prestazioni del rotore principale di un elicottero è oggetto di svariate ricerche, in quanto esso esercita un' influenza molto alta sul comportamento globale del mezzo in volo a punto fisso, in volo avanzato, nell'ambito delle vibrazioni, della manovrabilità, dell'emissione di rumore, eccetera. Uno degli aspetti cruciali nella progettazione delle pale di un rotore è che sono soggette ad un ampia gamma di condizioni aerodinamiche differenti, che dipendono dalla posizione azimutale e dalle condizioni di volo, quindi può risultare difficile scegliere delle specifiche che tengano conto di questa variabilità e che siano un giusto compromesso tra le varie esigenze. La variazione di configurazione del rotore principale durante il volo può essere sfruttata in questo ambito per adattarsi alle diverse condizioni, al fine di migliorare le prestazioni e ridurre effetti indesiderati come le vibrazioni e il rumore.

Il fine di questo lavoro è quello di sviluppare un semplice modello di aerodinamica instazionaria armonica per profili deformabili adatto ad un' ottimizzazione preliminare delle deformazioni del profilo stesso per migliorarne

alcune prestazioni aerodinamiche. Un secondo obiettivo è l' investigazione del suddetto problema di ottimizzazione, per fornire le basi ad ulteriori sviluppi, i quali potrebbero concentrarsi su un progetto e una ottimizzazione più accurati e completi di una pala morphing. Dato che non si desidera fornire uno strumento di ottimizzazione operativo per un profilo adattivo, spesso la semplicità verrà preferita all' accuratezza.

Alcuni risultati sono calcolati anche per profili dotati di flap incernierati in serie, i quali rappresentano un modo classico, seppur non molto usato in ambito elicotteristico, di variare la curvatura di un profilo aerodinamico.

### Modello aerodinamico

Per implementare il problema di ottimizzazione agilmente, si è scelto di scegliere un modello semplice e leggero per descrivere l' aerodinamica associata al moto armonico del profilo. Questo può essere visto come un profilo sottile soggetto a moto armonico con ampiezza costante e sufficientemente piccola in una corrente a potenziale, bidimensionale e incomprimibile. Ciò permette di utilizzare una teoria linearizzata, in cui il profilo viene ridotto alla sua linea media. Grazie alla linearità, è possibile sfruttare il principio di sovrapposizione degli effetti, sommando soluzioni semplici per ricostruire la soluzione globale.

Per calcolare le azioni aerodinamiche, viene utilizzato l'approccio di Küssner e Schwarz, il quale si basa sulla rappresentazione in serie di Fourier della perturbazione di velocità rispetto alla variabile spaziale. La distribuzione di differenza di pressione $\Delta C_p$ sul profilo è calcolata a partire dai coefficienti della serie, chiamati coefficienti di *upwash*, dai quali si riescono ad ottenere anche la portanza, il momento e la potenza aerodinamica integrando opportunamente la distribuzione di pressione.

Il moto della linea media viene dapprima rappresentato con dei flap incernierati in serie, il cui movimento armonico si sovrappone a delle oscillazioni di *plunge* e *pitch*. In questo caso si riescono ad ottenere i risultati originali di Küssner e Schwarz i quali, per verificarne la convergenza, vengono comparati a quelli della teoria classica di Theodorsen.

Successivamente si descrive il movimento della linea media con una spline cubica, ovvero con una cubica base a cui si sovrappongono delle ulteriori deformazioni cubiche a partire da una certa ascissa, ovvero una sorta di flap

cubico (si veda la Figura C.1).

$$z(x,t) = \begin{cases} \mathcal{P}_0(x)e^{j\omega t} & \text{if } x < x_{F_0} \\ (\mathcal{P}_0(x) + \mathcal{P}_1(x))e^{j\omega t} & \text{if } x_{F_0} \leq x < x_{F_1} \\ (\mathcal{P}_0(x) + \mathcal{P}_1(x) + \mathcal{P}_2(x))e^{j\omega t} & \text{if } x_{F_1} \leq x < x_{F_2} \\ \dots \end{cases} \tag{C.1}$$

Viene sviluppato il calcolo dei coefficienti di upwash e delle azioni aerodinamiche anche per questo caso, ne viene fatta una verifica di convergenza e vengono confrontate con quelle prodotte dal profilo dotato di flap in configurazioni analoghe.

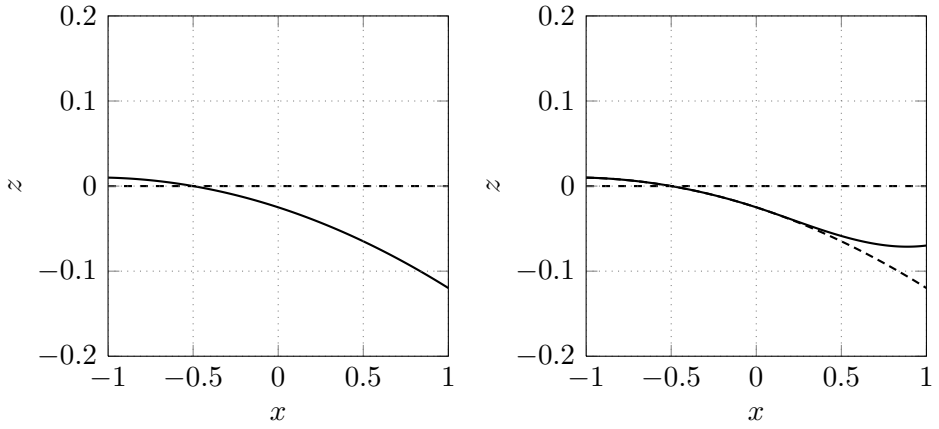


(A) Primo passo: deformazione cubica globale

(B) Secondo passo: sovrapposizione lineare del flap cubico

FIGURA C.1. Esempio di deformazione polinomiale cubica della linea media e sovrapposizione di un flap cubico

### Modello elastico e strutturale

Una volta scelto come modello strutturale per la rappresentazione del profilo un modello di trave di Eulero-Bernoulli, è possibile scriverne l'equazione di moto in forma debole per mezzo del Principio dei Lavori Virtuali, trascurando il contributo inerziale legato alla rotazione delle sezioni.

Gli spostamenti della trave vengono poi approssimati utilizzando un approccio alla Ritz-Galerkin.

Come funzioni di forma si sceglie di utilizzare degli elementi finiti hermitiani, i quali garantiscono una regolarità della soluzione di tipo $C^1$. Una delle caratteristiche fondamentali degli elementi finiti sta nella suddivisione

del dominio (ossia la trave) in un insieme di sottodomini, detti elementi. Vengono definite delle funzioni di forma, le quali interpolano la soluzione su ciascun elemento a partire dal valore che essa assume sui nodi dell'elemento stesso, ovvero dai gradi di libertà, mentre queste funzioni sono nulle sugli altri elementi. Ciò significa che le funzioni di forma sono a supporto compatto, da cui ne risulta, come vantaggio, la sparsità delle matrici di massa e rigidezza.

Per il calcolo di queste matrici è necessario anche stabilire una rappresentazione per la distribuzione di massa e di rigidezza flessionale. Un metodo semplice ma efficace per lo scopo della tesi è di considerarle rispettivamente proporzionali allo spessore del profilo e al suo cubo, calcolando una densità media $\rho_s$ e un modulo elastico approssimato $E_s$ a partire dalle caratteristiche di un esempio di profilo NACA0012 di applicazione elicotteristica.

$$m(x) = \rho_s \, t(x) \tag{C.2}$$
$$EJ(x) = E_s \, t^3(x) \tag{C.3}$$

Gli integrali per il calcolo delle suddette matrici sono svolti numericamente con il metodo di integrazione di Gauss.

Viene infine realizzata una trasformazione di variabili per generare un'interfaccia tra variabili strutturali (i gradi di libertà degli elementi finiti) e variabili aerodinamiche (i coefficienti della spline).

### Ottimizzazione

Come prima cosa, quando si vuole affrontare un problema di ottimizzazione è necessario decidere cosa si vuole ottimizzare e, di conseguenza, definire delle funzioni obiettivo (o funzioni di merito) che descrivano matematicamente l'obiettivo ricercato.

Può essere interessante scegliere di minimizzare il contributo oscillatorio di momento aerodinamico che si genera quando si vuole ottenere una certa oscillazione armonica di portanza per mezzo della variazione di incidenza e curvatura del profilo. Ciò può essere utile, nell'ottica di una vera pala di rotore, per ridurre il carico vibratorio sulla pala stessa e trasmesso al mozzo, al fine di migliorare il comportamento a fatica e il livello di vibrazioni. Il problema di ottimizzazione può essere quindi scritto come:

$$\text{minimizzare} \qquad J(\mathbf{x}) = |C_M(\mathbf{x})|^2 \tag{C.4}$$
$$\text{soggetto a} \qquad f(\mathbf{x}) = |C_L(\mathbf{x})|^2 - \bar{C}_L^2 = 0, \tag{C.5}$$
$$x_i \in [\mathrm{LB}, \mathrm{UB}] \text{ per } i = 1, \ldots, n_{\mathrm{var}} \tag{C.6}$$

É inoltre possibile pensare di aggiungere un secondo obiettivo, ovvero la minimizzazione della potenza (aerodinamica o totale di attuazione) richiesta per la deformazione del profilo. Il problema diventa quindi un'ottimizzazione multiobiettivo, per cui non si cerca più una sola soluzione ottima ma l'insieme di soluzioni non dominate appartenenti al fronte di Pareto. Il problema può essere scritto nel seguente modo:

$$\begin{aligned} \text{minimizzare} \quad & |C_M(\mathbf{x})|^2 \text{ e } |C_W(\mathbf{x})|^2 && \text{(C.7)} \\ \text{soggetto a} \quad & f(\mathbf{x}) = |C_L(\mathbf{x})|^2 - \bar{C}_L^2 = 0, && \text{(C.8)} \\ & x_i \in [\text{LB}, \text{UB}] \text{ per } i = 1, \ldots, n_{\text{var}} && \text{(C.9)} \end{aligned}$$

Le ottimizzazioni vengono svolte sia con un metodo *gradient-based*, ossia con un algoritmo *sequential quadratic programming* (SQP), sia con un metodo evolutivo, in particolare con un algoritmo genetico (GA).

Viene inoltre proposto un metodo analitico di ottimizzazione non vincolata del solo momento aerodinamico, utile per una verifica iniziale di convergenza dei metodi numerici.

### Risultati

Utilizzando quanto sopra descritto, è possibile ottenere i valori ottimali di incidenza e deflessione per la minimizzazione del solo momento aerodinamico nel caso di flap singolo e di flap e tab. Per quest'ultima configurazione viene condotta anche l'ottimizzazione multiobiettivo che minimizza momento e potenza aerodinamica. Questi casi più semplici vengono utilizzati anche per la messa a punto e la verifica di convergenza dei metodi numerici di ottimizzazione. Tutte le minimizzazioni sono ripetute a diverse frequenze ridotte.

É poi possibile ripetere queste ottimizzazioni per il modello polinomiale cubico a tratti di linea media. Per quanto riguarda il caso più interessante, ovvero quello multiobiettivo, viene realizzato anche una verifica di convergenza: si aumenta il numero di tratti di spline (e quindi di variabili) preso in considerazione verificando che le forme ottime ottenute non cambino molto, accertando che il numero di variabili usato è sufficiente a descrivere la soluzione.

Infine, mantenendo il numero di tratti di spline risultato dall'analisi di convergenza, si svolge l'ottimizzazione multiobiettivo bel momento aerodinamico e della potenza di attuazione globale, variando, oltre alla frequenza ridotta, i valori di densità e di modulo elastico equivalente. In generale le forme ottenute nelle ottimizzazioni multiobiettivo si assestano su curve con due cambi di segno nella derivata seconda, l'ampiezza e la forma specifica

della deformazione dipende però dal valore assunto dai parametri adimensionali che caratterizzano il caso ($k$, $\frac{\rho_s}{\rho}$ e $\frac{E_s}{\rho U^2}$) e dal punto del fronte di Pareto in cui si trova la soluzione.

# BIBLIOGRAPHY


[1] R. L. Bisplinghoff, H. Ashley, and R. L. Halfman. *Aeroelasticity*. Dover Publications, 1996.

[2] S. Boyd and L. Vandenberghe. *Convex Optimization*. Cambridge University Press, 2004.

[3] T. F. Coleman and Y. Zhang. *Optimization Toolbox$^{TM}$user's guide*. The MathWorks, Inc., 2013.

[4] V. Comincioli. *Analisi numerica: metodi, modelli, applicazioni*. McGraw - Hill, 1990.

[5] K. Deb. An introduction to genetic algorithms. *Sadhana*, **24**:293–315, 2009.

[6] K. Deb. Multi-objective optimization using evolutionary algorithms: An introduction. *KanGAL Report*, **N. 2011003**, 2011.

[7] K. Deb, A. Pratap, S. Agarwal, and T. Meyarivan. A fast and elitist multiobjective genetic algorithm: Nsga-ii. *IEEE Transactions on Evolutionary Computation*, **Vol. 6**, 2002.

[8] R. Drazumeric, B. Gjerek, F. Kosel, and P. Marzocca. On bimodal flutter behavior of a flexible airfoil. *Journal of Fluids and Structures*, **45**:164–179, 2014.

[9] Y. C. Fung. *An introduction to the theory of aeroelasticity*. Dover Publications, 2008.

[10] P. Gamboa, A. Suleman, J. Vale, and F. J. P. Lau. Optimization of a morphing wing based on coupled aerodynamic and structural constraints. *AIAA Journal*, **47**:2087–2104, 2009.

[11] H. Glauert. A theory of thin aerofoils. *British A.R.C.*, **R. & M. No. 910**, 1924.

[12] H. Glauert. Theoretical relationships for an aerofoil with hinged flap. *British A.R.C.*, **R. & M. No. 1095**:129–138, 1927.

[13] C. O. Johnston, W. H. Mason, and C. Han. Unsteady thin airfoil theory revisited for a general deforming airfoil. *Journal of Mechanical Science and Technology*, **24**:2451–2460, 2010.

[14] H. Julian Allen. Calculation of the chordwise load distribution over airfoil sections with plain, split or serially hinged trailing-edge flaps. *NACA*, **Report No. 634**:435–450, 1938.

[15] H. G. Küssner and I. Schwarz. The oscillating wing with aerodynamically balanced elevator. *NACA*, **T.M. No. 991**, 1941.

[16] J. Murua, R. Palacios, and J. Peirò. Camber effects in the dynamic aeroelasticity of compliant airfoils. *Journal of Fluids and Structures*, **26**, 2012.

[17] H. Namgoong, W. A. Crossley, and A. S. Lyrintzis. Aerodynamic optimization of a morphing airfoil using energy as an objective. *AIAA Journal*, **45**, 2007.

[18] O. Nelles. *Nonlinear system identification*. Springer, 2001.

[19] J. Nocedal and S. J. Wright. *Numerical Optimization*. Springer, 1999.

[20] M. J. Santer and S. Pellegrino. Topology optimization of adaptive compliant aircraft wing leading edge. In *48th AIAA/ASME/ASCE/AHS/ASC Structures, Structural Dynamics, and Materials Conference*, 2007.

[21] M. J. Santer and S. Pellegrino. Topological optimization of compliant adaptive wing structure. *AIAA Journal*, **47**, 2009.

[22] T. Theodorsen. General theory of aerodynamic instability and the mechanism of flutter. *NACA*, **Report No. 496**:413–419, 1934.

[23] T. Theodorsen and I. E. Garrick. Nonstationary flow about a wing-aileron-tab combination including aerodynamic balance. *NACA*, **Report No. 736**:129–138, 1941.

[24] K.-V Truong, H. Yeo, and R. A. Ormiston. Structural dynamics modeling of rectangular rotor blades. *Aerospace Science and Technology*, **30**, 2013.

[25] W. P. Walker. *Optimization of Harmonically Deforming Thin Airfoils and Membrane Wings for Optimum Thrust and Efficiency*. PhD thesis, 2012.